DEVELOPING AND CHARACTERIZING BULK METALLIC GLASSES FOR EXTREME APPLICATIONS

THESIS BY

SCOTT NOLAN ROBERTS

IN PARTIAL FULFILLMENT OF THE REQUIREMENTS FOR THE DEGREE OF

DOCTOR OF PHILOSOPHY

CALIFORNIA INSTITUTE OF TECHNOLOGY

PASADENA, CALIFORNIA

2014

DEFENDED DECEMBER 16, 2013

NOTHING IS TOO SMALL…

PUT DOWN IN RECORD EVEN YOUR DOUBTS AND SURMISES…

WE LEARN FROM FAILURE,

NOT FROM SUCCESS!

ABRAHAM VAN HELSING, M.D., D.PH., D.LITT., ETC.

ABSTRACT

Metallic glasses have typically been treated as a “one size fits all” type of material. Every alloy is considered to have high strength, high hardness, large elastic limits, corrosion resistance, etc. However, similar to traditional crystalline materials, properties are strongly dependent upon the constituent elements, how it was processed, and the conditions under which it will be used. An important distinction which can be made is between metallic glasses and their composites. Charpy impact toughness measurements are performed to determine the effect processing and microstructure have on bulk metallic glass matrix composites (BMGMCs). Samples are suction cast, machined from commercial plates, and semi-solidly forged (SSF). The SSF specimens have been found to have the highest impact toughness due to the coarsening of the dendrites, which occurs during the semi-solid processing stages. Ductile to brittle transition (DTBT) temperatures are measured for a BMGMC. While at room temperature the BMGMC is highly toughened compared to a fully glassy alloy, it undergoes a DTBT by 250 K. At this point, its impact toughness mirrors that of the constituent glassy matrix. In the following chapter, BMGMCs are shown to have the capability of being capacitively welded to form single, monolithic structures. Shear measurements are performed across welded samples, and, at sufficient weld energies, are found to retain the strength of the parent alloy. Cross-sections are inspected via SEM and no visible crystallization of the matrix occurs.

Next, metallic glasses and BMGMCs are formed into sheets and eggbox structures are tested in hypervelocity impacts. Metallic glasses are ideal candidates for protection against micrometeorite orbital debris due to their high hardness and relatively low density. A flat single layer, flat BMG is compared to a BMGMC eggbox and the latter creates a more diffuse projectile cloud after penetration. A three tiered eggbox structure is also tested by firing a 3.17 mm aluminum sphere at 2.7 km/s at it. The projectile penetrates the first two layers, but is successfully contained by the third.

A large series of metallic glass alloys are created and their wear loss is measured in a pin on disk test. Wear is found to vary dramatically among different metallic glasses, with some considerably outperforming the current state-of-the-art crystalline material (most notably $Cu_{43}Zr_{43}Al_7Be_7$). Others, on the other hand, suffered extensive wear loss. Commercially available Vitreloy 1 lost nearly three times as much mass in wear as alloy prepared in a laboratory setting. No conclusive correlations can be found between any set of mechanical properties (hardness, density, elastic, bulk, or shear modulus, Poisson's ratio, frictional force, and run in time) and wear loss. Heat treatments are performed on Vitreloy 1 and $Cu_{43}Zr_{43}Al_7Be_7$. Anneals near the glass transition temperature are found to increase hardness slightly, but decrease wear loss significantly. Crystallization of both alloys leads to dramatic increases in wear resistance. Finally, wear tests under vacuum are performed on the two alloys above. Vitreloy 1 experiences a dramatic decrease in wear loss, while $Cu_{43}Zr_{43}Al_7Be_7$ has a moderate increase. Meanwhile, gears are fabricated through three techniques: electrical discharge machining of 1 cm by 3 mm cylinders, semisolid forging, and copper mold suction casting. Initial testing finds the pin on disk test to be an accurate predictor of wear performance in gears.

The final chapter explores an exciting technique in the field of additive manufacturing. Laser engineered net shaping (LENS) is a method whereby small amounts of metallic powders are melted by a laser such that shapes and designs can be built layer by layer into a final part. The technique is extended to mixing different powders during melting, so that compositional gradients can be created across a manufactured part. Two compositional gradients are fabricated and characterized. Ti-6Al-4V to pure vanadium was chosen for its combination of high strength and light weight on one end, and high melting point on the other. It was inspected by cross-sectional x-ray diffraction, and only the anticipated phases were present. 304L stainless steel to Invar 36 was created in both pillar and as a radial gradient. It combines strength and weldability along with a zero coefficient of thermal expansion material. Only the austenite phase is found to be present via x-ray diffraction. Coefficient of thermal expansion is measured for four compositions, and it is found to be tunable depending on composition.

ACKNOWLEDGEMENTS

First, I would like to thank my advisor, Bill Johnson. Back when I was doing graduate school interviews, I remember Bill was the first professor I interviewed with. An hour later, I felt torn. If every professor was as excited about their work as Bill, how would I ever choose where to attend school? After visiting a few more schools the choice was obvious. I would be attending Caltech. When I started in the lab in the fall of 2007, Aaron Wiest taught me the ropes and helped guide me through my candidacy project.

After Aaron graduated, I found myself working with Doug Hofmann on semisolid forging of metallic glass composites. Doug continued as a mentor to me throughout my graduate career, and I look forward to working with him in the future in our lab at the Jet Propulsion Laboratory.

I'd also like to thank all of my fellow labmates. Henry Kozachkov for always being a sympathetic ear and being able to make me laugh harder than anyone else. Joanna Kolodziejska for all her help with my later projects, and being willing to actually get stuff done when the rest of us were at the point of giving up. Andrew Hoff for being continually eager to learn about everything we've been doing in the lab, and help rekindle my passion for what I had been doing throughout my graduate career. Xiao Lu for saving my bacon a number of times when I was TAing APh 105. Dale Conner for our many discussions on research possibilities. It's a shame our melt spinner had to meet the fate it did. Marios Demetriou for always keeping group meeting interesting.

My classmates at Caltech were also a continual source of inspiration. The first two years here were some of the hardest of my life, and I wouldn't have been able to get through without my study group: Aaron Varga, Nick Stadie, Chatr Panithipongwut, Jorge Munoz, and Pratyush Tiwary. During my time here at Caltech, I've also spent a lot of time TAing classes. Thank you to everyone that attended recitations, asked questions, and helped me make the best of nine terms of teaching assistant duties. The ISP lunches hosted by Daniel Yoder and Laura Flower Kim offered a weekly chance to kick back, enjoy some good food, and learn about my colleagues from all over the world. Their sponsoring of the summer softball team, the Asteroid Pirates, I co-captained with Lisa Mauger also gave a lot of us a fun way of getting some sun.

Finally, I'd like to thank all those closest to me. My parents have always done their best to stand by my decisions and support me throughout my struggles. It didn't matter if it was standing up for my argument with a teacher on displaying my artwork in elementary school or moving 3000 miles from home to attend grad school. Last, but certainly not least, is my partner through this long journey, Sanda Cea. Her faith in my ability to finish my degree at Caltech even prior to my acceptance here has helped me stay positive time and time again. There's no way I would have been able to finish my thesis without the many nights you kept me company in the office while I battled my way through this document. If you ever decide to write a thesis yourself, I'll have to find a bigger couch.

TABLE OF CONTENTS

LIST OF FIGURES

LIST OF TABLES

Chapter 1 - Introduction

Materials Science is a field which seeks to understand the interrelationship between processing, properties, structure, and performance. This thesis will approach each of these cornerstones of the field through the study of metallic glasses. Due to their sensitivity to slow cooling rates, they offer distinct challenges in processing, while at the same time, they offer unique processing capabilities through technologies such as rapid discharge forming[1] and electromagnetic forming.[2] The properties of metallic glass are also their own unique set. Bulk metallic glasses (BMGs) have largely been treated as a one size-fits-all material. They can have high strength, large elastic limits, high hardness, high toughness, corrosion resistance, and a host of other commonly desirable traits, but all of these properties are not true for every alloy. The critical constraints of each application need to be considered individually. Saying metallic glasses are resistant to corrosion is like saying because titanium alloys are popular materials for aerospace applications, cadmium should be a good choice as well, because they both have a hexagonal closed packed crystal structure.

The first non-crystalline metallic alloys were discovered by Klement, Willens, and Duwez in 1960 during a series of experiments designed to probe the effects of extremely high cooling rates on the eutectic microstructure.[3] It was already known that as the cooling rate was increased, the interlaminar spacing would decrease.[4] Previous efforts in rapid cooling had been performed by propelling small droplets of molten alloy into another liquid. However, the cooling rate was limited by the vapor barrier which would be created by the molten droplet evaporating a liquid, as well as the need for the molten droplet to spread out rapidly into a thin layer to minimize the distance for heat to diffuse. Duwez was able to overcome both of these obstacles by dripping molten droplets onto a spinning copper wheel. The force from the wheel on the droplet rapidly elongates it, and copper provides an optimal heat sink to rapidly draw heat away from the droplet.[5] Through this method, an Au-Si binary glass was formed.[3] Previously, the optimal technique for quenching molten metals was to allow droplets to fall into a viscous liquid to quench the molten droplet.

For almost a decade glasses were only able to be formed as either splats or thin ribbons. Even though this the melt spinning technique would eventually yield MetGlas, a commercially viable material, the field itself was limited by the thin casting limits.[6] Chen and Turnbull broke through this barrier by producing various alloys of the Pd-Si-Au/Ag/Cu family which were able to be cast to thicknesses greater than 1 mm.[7] Not until the developments of the Pd-Ni-Cu-P and Zr-Al-Ni-Cu alloys developed by the Inoue group at Tohoku University and the Zr-Ti-Be family of alloys developed by the Johnson group at Caltech were glassy alloys available in excess of a centimeter.[8–10]

With these new materials came a new wave of interest in metallic glass research. Now, more complicated geometries than simple ribbons could be created. These bulk glass formers lead to the initial commercial development of bulk metallic glasses. Products such as golf clubs and cell phone cases rapidly came to market. However, it was found that the lack of control during processing lead to impurities present in the final product which had devastating effects on the properties. Instead of being tough and strong, they were brittle.[11–13]

A fully amorphous MG's microstructure lacks grains, dislocations, or any of the other hallmarks of a traditional crystalline solid. Their microstructure is fairly simple. They can deform elastically up to their elastic limit, after which point they typically fail catastrophically due to a single shear band. So, taking cues from effective methods of toughing other metals, the thought was to extrinsically introduce second phases into the bulk metallic glass. Efforts were made with the infiltration of powders,[14,15] fiber reinforcements,[16,17] sintering multiple glasses together,[18] extruding metallic glass powders with crystalline fibers,[19] and more.[20] An alternative approach is to partially crystallize the BMG upon cooling, which results in a multi-phase structure.[21] This led to the development of a new class of bulk metallic glass matrix composites, where a soft crystalline dendrite is grown to inhibit crack growth and increase toughness.

However, it wasn't until a study by Conner et. al.[22] that the cause for the increased toughness of metallic glass composites could be fully explained. It was discovered that if a metallic glass' thickness is, at most, twice the alloy's plastic zone size, then, in bending, ductility could be achieved. As a shear band grows from the outside of a bending surface, it will eventually reach the neutral axis of stress. At this point the tensile force will be zero, preventing the shear band from propagating any further. On the compressive side of the whisker, shear bands would not be able to propagate, since they are constrained by compressive stresses. By taking this result and expanding on it, an idea for a desired maximum length scale for a continuous amorphous matrix is apparent.

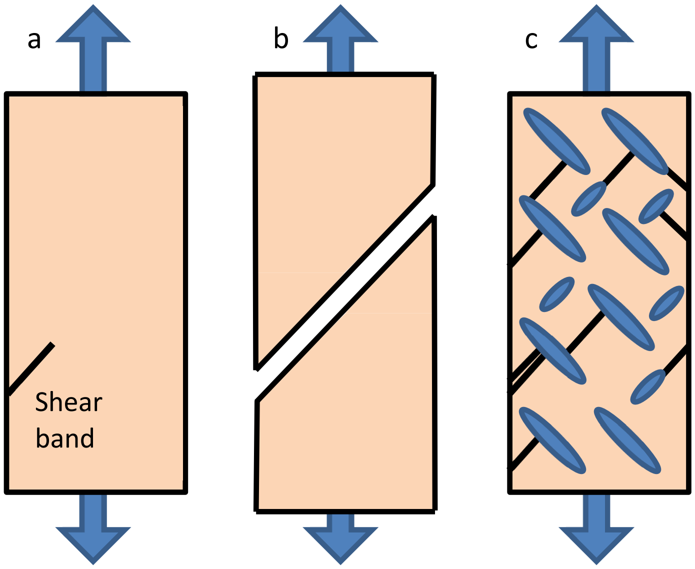

Figure 1-1: (a) A shear band beginning to grow in a BMG. (b) Failure by a single shear band in a bulk glass. (c) Multiple shear bands growth being arrested by a secondary phase.

If a second phase can be embedded in a BMG with this sort of spacing, ductility and increased toughness can be expected. Initially a shear band will nucleate and begin to grow. As long as it interacts with a second phase particle prior to becoming large enough to cavitate the shear band's growth will be arrested. At this point, the tip of the shear band will be blunted (the radius of curvature will go from extremely sharp to the size of the second phase particle). It is now energetically favorable to nucleate new shear bands instead of trying to propagate the initial one. For this reason, a well reinforced composite glass will exhibit superior plasticity (Figure 1-1).

The next step was to combine the idea of a BMG with a crystalline dendrite inside of it, along with controlling the spacing of the dendrite's arms to be approximately the critical shear band length. Hofmann et al.[23] were able to achieve this goal by holding molten ZrTiNbCuBe alloys below the liquidus temperature, but above the solidus. This technique allowed body centered cubic (bcc) dendrites to nucleate and grow. Previously, the composites had been rapidly quenched, and as such, the dendrite microstructure was heavily dependent upon the location within the sample and the apparent cooling rate. Dendrites nearest the surface experienced the fastest cooling, and wound up with very small dendrite morphologies. Those at the center had time for grain refinement, and wound up with more favorable mechanical properties, as their spacing was closer to the critical shear band length. Holding the entire ingot in the semisolid region allows dendrites to nucleate everywhere and grow at the same rate throughout. The whole sample can then be quenched, resulting in relatively uniform properties. Ductility was able to be achieved even in pure tension through this technique.[24]

The ability to hold a bulk metallic glass matrix composite (BMGMC) within the semi-solid region without causing rapid crystallization of an entire ingot upon rapid cooling offers different processing techniques compared to a traditional BMG. One of the limitations of BMGs is their continual reliance on “beating the clock.” In other words, when processing a BMG one must always avoid crystallization. If a part requires multiple heating and cooling steps (such as forming feedstock ingots, then later heating and forging them into a final shape), crystallization must be avoided at all times. Even if the final part is to be sub-mm in thickness, if the feedstock ingot is thicker, then the critical casting thickness must be large enough for the feedstock to quench sufficiently. It must also not crystallize during heating prior to forging as well as after the forming process. On the other hand, if a BMGMC is being semisolidly processed,[25] the original ingot can be allowed to crystallize during cooling into feedstock. This is because during semisolid forging the ingot is reheated back above the solidus temperature. At this point, any crystals which have formed in the matrix will melt, leaving a mixture of liquid and equilibrium dendrite. The liquid can then readily be revitrified with a sufficient cooling rate.

Another class of BMGs containing crystals is those which partially crystallize in an uncontrolled manner upon quenching; these have been demonstrated in numerous studies.[26–29] A problem with this method is the inconsistency in properties of the final alloy, as well as the microstructure’s strong dependence upon the geometry of the final part. While an alloy may give an optimal microstructure for a 1 mm rod, when processed into a half millimeter thick sheet the dendrites may not have enough time to fully grow. Likewise, for a 2 mm thick rod the center may cool too slowly, and an excess of crystals could form. It may be a possibility to design an alloy around a particular application. First, determine the final geometry which will be used, then develop particular alloys for each situation. This method seems fairly difficult, however, as generally things are not of uniform thickness, and, even if they are, cooling rates may vary across a mold, giving different microstructures at different parts.

Since this thesis focuses predominantly on BMGs and BMCMCs, and each of these are heavily dependent upon both the thermodynamics of a system as well as the kinetics inside the system, it is informative basic theories of crystallization from a liquid. When a new crystalline phase, α, begins to form from a liquid, it will take up some volume of the liquid. It will also create a liquid/crystal interface. Both of these terms have an energetic cost, and if growth is assumed to be spherical, the resultant energy change in the system is

$$\Delta G = \left(4\pi r^2\right)\sigma_{sl} - \frac{4}{3}\pi r^3 \Delta G_V \tag{1}$$

where ΔG_V is the change in Gibbs free energy from the liquid to the crystal, σ_{sl} is the interfacial energy between the solid and liquid phases, and r is the radius of the nuclei. A system is at equilibrium when G is minimized. This minimum will be reached when the volume term becomes equivalent to the surface energy term. This can be found by taking $\left.\frac{\delta(\Delta G)}{\delta r}\right|_{r_c} = 0$,where r_c is the critical radius.

$$\begin{aligned} 8\pi r\sigma_{sl} - 4\pi r^2 \Delta G_V &= 0 \\ 4\pi r^2 \Delta G_V &= 8\pi r\sigma_{sl} \\ r &= \frac{2\sigma_{sl}}{\Delta G_V} \end{aligned} \tag{2}$$

This relationship can then be reinserted into our initial equation to find the critical free energy difference, ΔG_c

$$\Delta G_c = \frac{16\pi}{3}\left(\frac{\sigma_{sl}^3}{\Delta G_V^2}\right) \tag{3}$$

Another thought experiment which can be performed is estimating the amount of total fraction of volume taken up by spherical α nuclei as they grow in a liquid. Provided nucleation occurs randomly and evenly throughout the liquid, and growth rate is constant and isotropic. For the first nuclei to form

$$V = \frac{4}{3}\pi r^3 = \frac{4}{3}\pi (vt)^3 \tag{4}$$

For any nuclei forming later, it would begin its growth at time τ,

$$V' = \frac{4}{3}\pi v^3 (t-\tau)^3 \tag{5}$$

For a given amount of time, dτ, there will be *N*dτ nuclei forming. So, in the beginning of transformation (before particle impingement occurs) the total extended volume is

$$f_\alpha^e = \frac{4\pi}{3} N v^3 \int_0^t (t-\tau)^3 \, d\tau$$
$$f_\alpha^e = \frac{\pi}{3} N v^3 t^4 \tag{6}$$

As stated above, this will only be valid for very short times, or when *f* is small. In order to extend the theory to longer times, the overlap of nuclei forming inside existing nuclei which have already grown must be taken into account. For this reason, above, f_α^e is given as the fraction of volume which has been transformed, including multiple counting of areas due to overlapping nuclei. The actual volume transformed is related by

$$df_\alpha = df_\alpha^e f_L$$
$$df_\alpha = df_\alpha^e (1 - f_\alpha) \tag{7}$$

Rearranging , integrating, and solving for fraction transformed

$$\int \frac{1}{(1-f_\alpha)} df_\alpha = \int df_\alpha^e$$

$$\begin{aligned} \ln(1-f_\alpha) &= -f_\alpha^e \\ 1-f_\alpha &= \exp\left(-f_\alpha^e\right) \\ f_\alpha &= 1-\exp\left(-f_\alpha^e\right) \end{aligned} \tag{8}$$

Substituting back in the value for f_α^e from above

$$f_\alpha = 1-\exp\left(-\frac{\pi}{3}Nv^3t^4\right) \tag{9}$$

By grouping all of the constants on the right hand side together, a familiar result, the Johnson-Mehl-Avrami-Kolmogorov, is reached.

$$f_\alpha = 1-\exp\left(-Kt^n\right) \tag{10}$$

Where *K* is a collection of the nucleation rate, growth velocity, and geometric factors. By generalizing t^4 to t^n, different types of growth can be modeled. If desired, this equation can be further rewritten.

$$\begin{aligned} \ln(1-f_\alpha) &= -Kt^n \\ \ln\left[-\ln(1-f_\alpha)\right] &= \ln\left(Kt^n\right) \\ \ln\left[-\ln(1-f_\alpha)\right] &= \ln(K)+n\ln(t) \end{aligned} \tag{11}$$

By performing this simplification, plotting $\ln\left[-\ln(1-f_\alpha)\right]$ versus $\ln(t)$, the slope will give the resultant *n*. In the initial case, *n* = 4, and that could be seen as a particle growing in three dimensions, plus additional particles linearly being added to the system. In the cases of *n* = 1, 2, or 3 for transformations involving site saturation, it would indicate nucleation on surfaces, edges, and points, respectively.[30] In the third situation, growth could initially be seen as *n* = 4, but as soon as the point sites saturate, it changes to a value of 3. Likewise, if, instead of the α nuclei growing as spheres, they grew as circular platelets without saturated sites, it could be seen that *n* would also be equal to 3 for this case (with saturated point sites it would be 2).

To this point the temperature sensitivity of the nucleation and growth rates have not been discussed. While they will not be derived explicitly here, the nucleation rate can be found to be equal to[31]:

$$N = \frac{A}{\eta}\exp\left(-\frac{\Delta G_c}{k_b T}\right)$$

$$N = \frac{A}{\eta}\exp\left(-\frac{16\pi}{3}\frac{\sigma_{sl}^3}{k_b T(\Delta G_V)}\right) \tag{12}$$

Where k_b is Boltzmann's constant, A is comprised of constants, and η is the viscosity, whose temperature dependence can be given as

$$\eta(T) = \eta_0 \exp\left(\frac{DT}{T - T_0}\right) \tag{13}$$

The growth velocity can be expressed as

$$v = \frac{k_b}{3\pi L^2 \eta}\left[1 - \exp\left(-\frac{\phi(\Delta G_c)}{k_b T}\right)\right]$$

$$v = \frac{k_b}{3\pi\eta L^2}\left[1 - \exp\left(-\frac{16\pi}{3}\frac{\phi\sigma_{sl}^3}{k_b T(\Delta G_V)}\right)\right] \tag{14}$$

where ϕ is the average atomic volume and L is the average atomic diameter. By returning to Equation (9) above and inserting all of the expressions given, a full model can be given for the evolution of the microstructure of a material.

$$f_\alpha = 1 - \exp\left(-\frac{\pi}{3}\frac{A}{\eta}\exp\left(-\frac{16\pi}{3}\frac{\sigma_{sl}^3}{k_b T(\Delta G_V)}\right)\left(\frac{k_b}{3\pi\eta L^2}\left[1 - \exp\left(-\frac{16\pi}{3}\frac{\phi\sigma_{sl}^3}{k_b T(\Delta G_V)}\right)\right]\right)^{n-1} t^n\right)$$

(15)

$$f_\alpha = 1 - \exp\left[-\frac{A k_b}{9\eta_0^2 e^{\frac{2DT}{T-T_0}} L^2} e^{-\frac{16\pi}{3}\frac{\sigma_{sl}^3}{k_b T(\Delta G_V)}}\left(1 - e^{-\frac{16\pi}{3}\frac{\phi\sigma_{sl}^3}{k_b T(\Delta G_V)}}\right)^{n-1} t^n\right] \tag{16}$$

It is fairly evident that even this relatively simple model winds up with complicated behavior. The viscosity, growth velocity, and nucleation rate are all exponentially dependent upon temperature. As the temperature decreases the nucleation rate will grow quickly, and the growth velocity will also decrease rapidly. From this, we can see there will be a specific temperature at which the product of the nucleation and growth rates will reach a maximum, and this would be the temperature at which the growth of α would be fastest. In terms of forming a BMG, this is the critical temperature which must be rapidly cooled to in order to stand a chance at vitrification. Taking this as a way to think about the accidental composites, one can readily see how sensitive they can be to processing conditions. Indeed, casting a 2 mm rod from a copper mold will have different cooling conditions versus a copper mold. In this case, one may have the desired microstructure, while the other would not.

The following chapters will deal with a number of different methods, properties, processes, and new applications for metallic glasses and their composites. In this introduction, an outline has been made of the past history of metallic glasses, starting from their origins as a thin, difficult to process material to the development of bulk metallic glasses which are able to be cast in excess of one inch in thickness. The importance of designing metallic glasses such that their feature size is on the order of their plastic zone size is necessary in preventing catastrophic failure. Finally, the way to design composites to take advantage of this knowledge was discussed.

The second chapter is a study of how Charpy impact toughness can be affected by processing conditions. Various alloys are fabricated through suction casting, semi-solid forging, and commercially cast plates. Their performance is compared with that of traditional engineering alloys. A series of cryogenic Charpy tests of two BMGs, one BMGMC, and a well-studied crystalline alloy are performed as well. In the end, a semi-solidly forged BMGMC has the highest impact toughness at room temperature and maintains parity with the well-performing BMGs even at cryogenic temperatures.

In the next chapter, the feasibility of joining bulk metallic glass matrix composites through rapid capacitive discharge is demonstrated. A series of measurements are performed to determine the maximum strength which can be achieved after welding, and it is found to be approximately that of the parent material. A cross section of the weld interface is inspected via SEM, and no traces of crystallization are found. The dendrite microstructure has not been heated sufficiently to be remelted nor heated long enough to coarsen. The matrix was able to be fully revitrified.

The fourth chapter explores the use of both bulk metallic glasses and bulk metallic glass matrix composites as energy absorbing materials in hypervelocity impacts. Flat sheets of Vitreloy 1 and an eggbox geometry of DH1 are impacted with a 3.17 mm aluminum sphere travelling at 2.7 km/sec. The eggbox's facets spread the ejected material out over a greater area, and are found to generate more light during the impact, implying a greater amount of energy was absorbed. The composite eggboxes are also welded into a multilayered Whipple shield, and they are able to fully stop the aluminum projectile with a velocity of 2.3 km/sec. The first two layers are penetrated, but the third stops any debris from passing through. The multilayered composites were found to outperform aluminum honeycomb sandwich panels for a given thickness. Metallic glasses and their composites are found to have a very promising future for hypervelocity impact protection, due to their high hardness and low melting point.

Next, preliminary measurements are performed to qualify metallic glasses as a potential material to become the replacement material for the gears on the Mars Space Laboratory. The currently used Vascomax gears cannot suffer from high wear rates when operated at cryogenic temperatures. For this reason, Curiosity’s gearboxes were outfitted with lubricants and heaters to prevent the gears from wearing excessively. Unfortunately, this requires substantial amounts of power and adds mass. Metallic glasses are reputed for their resistance to wear and are have been shown to lack a ductile to brittle phase transition,[32,33] so they should retain many of their attributes even at low temperatures.

A large series of metallic glass alloys are created and their wear loss is measured in a pin-on-disk test. Wear is found to vary dramatically among different metallic glasses, with some considerably outperforming Vascomax (most notably $Cu_{43}Zr_{43}Al_7Be_7$). Others, on the other hand, suffered extensive wear loss. Commercially available Vitreloy 1 was found to be much worse in wear compared to lab quality, likely due to impurities present during processing. This could explain some of the variability observed in the literature about this alloy. No conclusive correlations can be found between any set of mechanical properties (hardness, density, elastic, bulk, or shear modulus, Poisson’s ratio, frictional force, and run in time) and wear loss. Heat treatments are performed on Vitreloy 1 and $Cu_{43}Zr_{43}Al_7Be_7$. Anneals near the glass transition temperature are found to possibly increase hardness slightly, but decrease wear loss significantly. Crystallization of both alloys leads to dramatic increases in wear resistance. Finally, wear tests are performed on the two alloys above. Vitreloy 1 experiences a dramatic decrease in wear loss, while $Cu_{43}Zr_{43}Al_7Be_7$ has a moderate increase. Meanwhile, gears are fabricated through three techniques: electrical discharge machining of 1 cm by 3 mm cylinders, semisolid forging, and copper mold suction casting. Initial testing finds the pin-on-disk test to be an accurate predictor of wear performance in gears.

The final chapter explores an exciting technique in the field of additive manufacturing. Laser engineered net shaping (LENS) is a method whereby small amounts of metallic powders are melted by a laser such that shapes and designs can be built layer by layer into a final part. The technique is extended to mixing different powders during melting, so that compositional gradients can be created across a manufactured part. Two compositional gradients are fabricated and characterized. Ti-6Al-4V to pure vanadium was chosen for its combination of high strength and light weight on one end, and high melting point on the other. It was inspected by cross-sectional x-ray diffraction, and only the anticipated phases were present. A 304L stainless steel to Invar 36 transitionary alloy was fabricated in both linear and radial gradients. It combines strength and weldability along with a zero coefficient of thermal expansion material. Only the austenite phase is found to be present via x-ray diffraction. Coefficient of thermal expansion is measured for four compositions, and is found to be tunable depending on composition.

References

(1) Johnson, W. L.; Kaltenboeck, G.; Demetriou, M. D.; Schramm, J. P.; Liu, X.; Samwer, K.; Kim, C. P.; Hofmann, D. C. Beating crystallization in glass-forming metals by millisecond heating and processing. *Science* **2011**, *332*, 828–33.

(2) Johnson, W. L.; Kltenboeck, G.; Demetriou, M. D.; Roberts, S.; Samwer, K.; Kaltenboeck, G.; Demetrious, M. Electromagnetic forming of metallic glasses using a capacitive discharge and magnetic field **2013**, *2*, 1–27.

(3) Klement, W.; Willens, R. H.; Duwez, P. Non-crystalline structure in Solidified Gold-Silicon Alloys. *Nature* **1960**, *187*, 869–870.

(4) Hultgren, R.; Olsen, W. T. Effect of rate of freezing on degree of segregation in alloys. *AIME Trans* **1950**, 1323.

(5) Duwez, P.; Willens, R. H.; Klement, W. Continuous Series of Metastable Solid Solutions in Silver-Copper Alloys. *J. Appl. Phys.* **1960**, *31*, 1136.

(6) Liebermann, H.; Graham, C. Production of amorphous alloy ribbons and effects of apparatus parameters on ribbon dimensions. *IEEE Trans. Magn.* **1976**, *12*, 921–923.

(7) Chen, H. .; Turnbull, D. Formation, stability and structure of palladium-silicon based alloy glasses. *Acta Metall.* **1969**, *17*, 1021–1031.

(8) Inoue, A.; Zhang, T.; Nishiyama, N.; Ohba, K.; Masumoto, T. Preparation of 16 mm diameter rod of amorphous Zr65Al7.5Ni10Cu17.5 alloy. *Mater. Transations, JIM* **1993**, *34*, 1234–1237.

(9) Peker, A.; Johnson, W. L. A highly processable metallic glass: Zr41.2Ti13.8Cu12.5Ni10.0Be22.5. **1993**, *63*, 2342–2344.

(10) Inoue, A.; Nishiyama, N.; Matsuda, T. Preparation of Bulk Glassy Pd40Ni10Cu30P20 Alloy of 40 mm in Diameter by Water Quenching. *Mater. Trans. - JIM* **1996**, *37*, 181–184.

(11) Gebert, A.; Eckert, J.; Schultz, L. Effect of oxygen on phase formation and thermal stability of slowly cooled Zr65Al7.5Cu17.5Ni10 metallic glass. *Acta Mater.* **1998**, *46*, 5475–5482.

(12) Liu, C. T.; Chisholm, M. F.; Miller, M. K. Oxygen impurity and microalloying effect in a Zr-based bulk metallic glass alloy. *Intermetallics* **2002**, *10*, 1105–1112.

(13) Conner, R. D.; Maire, R. E.; Johnson, W. L. Effect of oxygen concentration upon the ductility of amorphous Zr57Nb5Al10Cu15.4Ni12.6. *Mater. Sci. Eng. A* **2006**, *419*, 148–152.

(14) Zhu, Z.; Zhang, H.; Hu, Z.; Zhang, W.; Inoue, a. Ta-particulate reinforced Zr-based bulk metallic glass matrix composite with tensile plasticity. *Scr. Mater.* **2010**, *62*, 278–281.

(15) Conner, R. D.; Choi-Yim, H.; Johnson, W. L. Mechanical properties of Zr57Nb5Al10Cu15.4Ni12.6 metallic glass matrix particulate composites. *J. Mater. Res.* **2011**, *14*, 3292–3297.

(16) Conner, R. D.; Dandliker, R. B.; Johnson, W. L. Mechanical properties of tungsten and steel fiber reinforced Zr41.25Ti13.75Cu12.5Ni10Be22.5 metallic glass matrix composites. *Acta Mater.* **1998**, *46*, 6089–6102.

(17) Clausen, B.; Lee, S. Y.; Ustundag, E.; Aydiner, C. C.; Conner, R. D.; Bourke, M. Compressive yielding of tungsten fiber reinforced bulk metallic glass composites. *Scr. Mater.* **2003**, *49*, 123–128.

(18) Cho, S.-M.; Han, J.-H.; Lee, J.-K.; Kim, Y.-C. Fe-Based Nano-Structured Powder Reinforced Zr-Based Bulk Metallic Glass Composites by Powder Consolidation. *Korean J. Mater. Res.* **2009**, *19*, 504–509.

(19) Bae, D. H.; Lee, M. H.; Kim, D. H.; Sordelet, D. J. Plasticity in Ni59Zr20Ti16Si2Sn3 metallic glass matrix composites containing brass fibers synthesized by warm extrusion of powders. *Appl. Phys. Lett.* **2003**, *83*, 2312.

(20) Lee, K. S.; Kang, S.-H.; Lee, Y.-S. Synthesis of Zr-based bulk metallic glass–crystalline aluminum alloy composite by co-extrusion. *Mater. Lett.* **2010**, *64*, 129–132.

(21) Szuecs, F.; Kim, C. P.; Johnson, W. L. Mechanical Properties of Zr56.2Ti13.8Nb5.0Cu6.9Ni5.6Be12.5 Ductile Phase Reinforced Bulk Metallic Glass Composite. *Acta Mater.* **2001**, *49*, 1507–1513.

(22) Conner, R. D.; Li, Y.; Nix, W. D.; Johnson, W. L. Shear band spacing under bending of Zr-based metallic glass plates. *Acta Mater.* **2004**, *52*, 2429–2434.

(23) Hofmann, D. C.; Suh, J.-Y.; Wiest, A.; Duan, G.; Lind, M.-L.; Demetriou, M. D.; Johnson, W. L. Designing metallic glass matrix composites with high toughness and tensile ductility. *Nature* **2008**, *451*, 1085–9.

(24) Hofmann, D. C.; Suh, J.-Y.; Wiest, A.; Lind, M.-L.; Demetriou, M. D.; Johnson, W. L. Development of tough, low-density titanium-based bulk metallic glass matrix composites with tensile ductility. *Proc. Natl. Acad. Sci. U. S. A.* **2008**, *105*, 20136–40.

(25) Hofmann, D. C.; Kozachkov, H.; Khalifa, H. E.; Schramm, J. P.; Demetriou, M. D.; Vecchio, K. S.; Johnson, W. L. Semi-solid induction forging of metallic glass matrix composites. *JOM* **2009**, *61*, 11–17.

(26) Qin, C. L.; Zhang, W.; Asami, K.; Kimura, H.; Wang, X. M.; Inoue, A. A novel Cu-based BMG composite with high corrosion resistance and excellent mechanical properties. *Acta Mater.* **2006**, *54*, 3713–3719.

(27) Chang, H. J.; Yook, W.; Park, E. S.; Kyeong, J. S.; Kim, D. H. Synthesis of metallic glass composites using phase separation phenomena. *Acta Mater.* **2010**, *58*, 2483–2491.

(28) Lim, K. R.; Na, J. H.; Park, J. M.; Kim, W. T.; Kim, D. H. Enhancement of plasticity in Ti-based metallic glass matrix composites by controlling characteristic and volume fraction of primary phase. *J. Mater. Res.* **2010**, *25*, 2183–2191.

(29) Park, J. M.; Jayaraj, J.; Kim, D. H.; Mattern, N.; Wang, G.; Eckert, J. Tailoring of in situ Ti-based bulk glassy matrix composites with high mechanical performance. *Intermetallics* **2010**, *18*, 1908–1911.

(30) Cahn, J. W. Transformation kinetics during continuous cooling. *Acta Metall.* **1956**, *4*, 572–575.

(31) Schroers, J.; Wu, Y.; Busch, R.; Johnson, W. L. Transition from Nucleation Controlled to Growth Controlled Crystallization in Pd43Ni10Cu27P20 Melts. *Acta Mater.* **2001**, *49*, 2773–2781.

(32) Li, H.; Tao, K.; Fan, C.; Liaw, P. K.; Choo, H. Effect of temperature on mechanical behavior of Zr-based bulk metallic glasses. *Appl. Phys. Lett.* **2006**, *89*, 041921.

(33) Roberts, S.; Zachrisson, C.; Kozachkov, H.; Ullah, A.; Shapiro, A. a.; Johnson, W. L.; Hofmann, D. C. Cryogenic Charpy impact testing of metallic glass matrix composites. *Scr. Mater.* **2012**, *66*, 284–287.

Chapter 2 – Effects of Processing and Temperature on Charpy Impact Toughness in Metallic Glasses and Metallic Glass Matrix Composites

Introduction to Charpy Testing

Charpy impact testing (CIT) is an ASTM standard fracture mechanics technique used to measure a material's notch toughness at moderately high strain rates. It is defined by the ASTM standard E23[1], requiring a 55x10x10 mm beam with a 45°, 2 mm deep notch cut into the midpoint of the 55 mm side (Figure 2-1). The testing apparatus consists of a weighted hammer mounted at the end of a pendulum. The hammer can be raised to a known height and the sample to be tested placed in the path of the hammer's swing, with the notch facing away from the impact surface (Figure 2-2). By measuring the height of the hammer's swing after impacting the sample, a measurement of the energy absorbed by a sample can be taken.

$$\Delta E = mg(h_f - h_i) \tag{1}$$

The lost potential energy is converted into work, which fractures the sample by driving a crack initiating at the notch. The sample geometry, with the notch facing away from the hammer's impact, is used to cause a stress concentration at the tip of the notch to ensure the sample fails instead of bending along the rest of the bar.

While the results obtained from a CIT are not necessarily quantitative by nature, it is a useful tool to make qualitative comparisons between different materials or conditions on a material's toughness. It will not provide a measurement of a quantitative property, such as plane-strain fracture toughness, K_{Ic}.

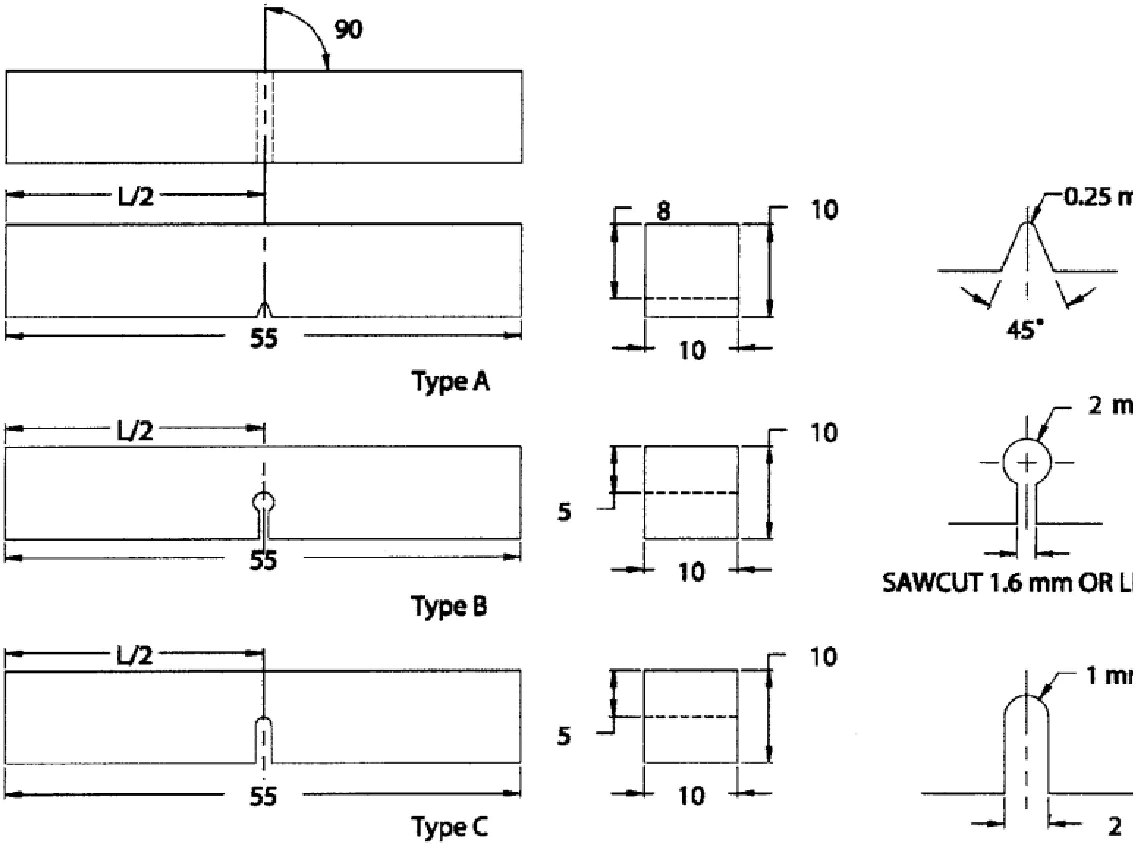

Notch length to edge	90 ±2°
Adjacent sides shall be at	90° ± 10 min
Cross-section dimensions	± 0.075 mm
Length of specimen (L)	+0, −2.5 mm
Centering of notch (L/2)	± 1 mm
Angel of notch	±1°
Radius of notch	±0.025 mm
Ligament Length:	±0.025 mm
Type A specimen	±0.025 mm
Type B and C specimen	±0.075 mm
Finish requirements	2 µm on notched surface and opposite face; 4 µm on other two surface

Figure 2-1: Geometry required for an ASTM standard Charpy impact test.[1] Type A is the geometry modified for our testing due to limitation in casting thickness in BMG alloys.

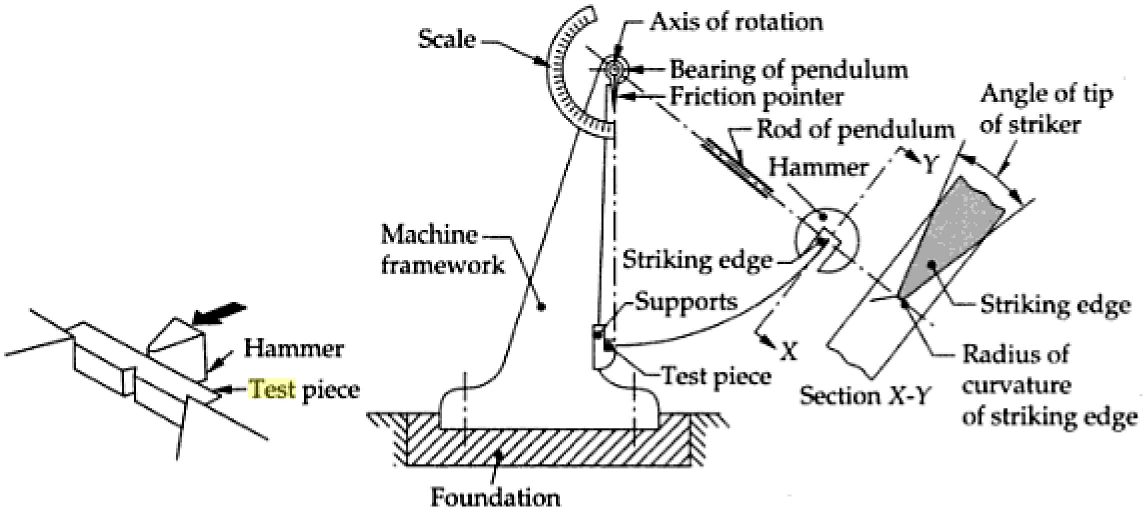

Figure 2-2: A schematic of a Charpy impact test.[2]

Some materials, upon cooling below a critical temperature, will exhibit a rapid decrease in their measured impact toughness. This change is called a ductile to brittle transition (DTBT). The CIT provides a rapid and reliable method to measure the relative change in impact toughness of a material as it becomes more brittle. This is primarily because the CIT test can be performed in a matter of seconds after removing a test specimen from a cryogenic bath or oven, allowing the entire test to be performed isothermally. In contrast, a plane-strain fracture toughness test would have to be performed in an environmental chamber for non-ambient temperature testing. It is known that fcc materials do not undergo a DTBT, while bcc and hcp metals do. Some cryogenic work has been done on BMGs to assess their ambient impact toughness, as well as their elevated and cryogenic toughness. Two Charpy studies were performed by Raghavan et al.[3,4] where in one study the BMG Vitreloy 1 was tested from 100 K to 450 K, and in the other the samples were annealed and then tested from 100 K to 600 K. Toughness was shown to dramatically decrease with increasing temperature in both studies. H Li et al.[5] performed compression tests of a Zr-based BMG at 77 K and observed an increase in the compressive yield strength compared to room temperature, while Huang et al.[6] saw both an increase in compressive strength and plasticity at 123 K. Yu et al.[7] studied the temperature dependence of the various elastic moduli at cryogenic temperatures. Qiao et al. [8] summarized the ultimate tensile strength of BMGs from 75 to 300 K. Not surprisingly, the properties of BMGs remain relatively unchanged even at cryogenic temperatures. The toughness does decrease with temperature, but in a linear fashion similar to fcc metals, instead of the sharp order-of-magnitude drop associated with bcc metals and those with a DTBT.

Although the toughness of BMGs doesn't decrease significantly at cryogenic temperatures, their initial toughness is fairly low compared with most high-performance engineering materials (e.g. titanium, steel, and aluminum alloys). To address this shortcoming, bulk metallic glass matrix composites (BMGMCs) have been developed to offer significantly higher toughness at room temperature due to the ability of a soft, bcc crystalline phase to stop shear band propagation. Qiao et al[8] performed compression tests on two BMGMCs to observe if the embedded bcc crystalline dendrites exhibited an expected DTBT temperature. In both alloys there was significant compressive plasticity at room temperature, but at 77 K the sample was brittle. Unfortunately, only two temperatures were measured (room temperature and 77 K), so there was not enough information to confirm or reject the existence of a DTBT in BMGMCs. In this chapter, measurements were performed at ten different temperatures ranging from 100 K to 300 K to allow for a more complete view of how impact toughness varies with temperature. Using impact testing instead of compressive testing is also preferred, as plasticity can be influenced by frictional forces during compression tests. Compression tests are also slow, making it difficult to maintain isothermal conditions throughout the test.

Charpy tests were also performed on a variety of BMGs and BMGMCs that were prepared using different processing conditions. This was done to provide a baseline for further Charpy testing of both BMGs and BMGMCs that cannot be formed into the shapes required for larger mechanical tests. This chapter also represents the first Charpy study of BMGMCs, done to compliment work done in the literature with quasistatic and dynamic mechanical testing.[9–14]

Experimental

This chapter focuses on comparing the impact behavior of three BMGMCs to Vitreloy 1 (a monolithic BMG) as well as some traditional crystalline alloys. The first BMGMC tested is a titanium-based alloy DV1 ($Ti_{48}Zr_{20}V_{12}Cu_5Be_{15}$), with 40% crystal volume fraction. The second is a zirconium-titanium-based alloy DH3 ($Zr_{39.9}Ti_{33.9}Nb_{7.6}Cu_{6.4}Be_{12.5}$), with 67% crystal volume fraction. LM2 ($Zr_{71.9}Ti_{9.3}Nb_6Cu_{6.15}Ni_{4.6}Be_{1.6}$), a commercially available zirconium-based composite material, is 40% crystalline. Vitreloy 1 ($Zr_{41.2}Ti_{13.8}Cu_{12.5}Ni_{10}Be_{22.5}$) is the BMG used for comparison, and is the most widely commercially used BMG (under the trade name LM1). Several crystalline alloys were also used for comparison with the BMG alloys. These include Ti-6Al-4V, Al-7075, Al-2024, and SS 304. To measure ductile to brittle transitions, both 99.9% pure tin and DH3-Matrix ($Zr_{35}Ti_{30}Cu_{8.25}Be_{26.75}$), a BMG with composition equivalent to that of the glass matrix in DH3, are used. A summary of their properties can be seen in Table 2-1.

BMG alloys were produced by arc melting high purity elements in a Ti-gettered argon atmosphere. Suction cast (SC) samples were then remelted in a mini-arc melter and cast into 3x3x30 mm beams. A notch 0.5 mm deep, 1 mm wide, 90° cut was made using an endmill. Semi-Solid Forged (SSF) samples were held isothermally above their solidus temperatures prior to forging to allow for dendrite coarsening before being formed into 3 mm thick plates. The plates were then sectioned on a laboratory saw and notched with an endmill similar to the SC samples.

Commercial alloys were procured as 3 mm thick plates, sectioned, and notched in a similar manner.

Charpy tests were performed on a modified Riehle Impact Testing Machine, which was instrumented to detect small changes in hammer velocity (Figure 2-3). Standard Charpy machines operate from two drop heights, 61 and 122 cm (24 and 48 in), with two hammer masses so that four maximum impact energies can be obtained: 41, 81, 163, and 325 J. Unfortunately, full-sized Charpy testing on Zr-Be-based BMGs from literature indicate only 1-5 J of energy is absorbed, whereas Zr-Be-based BMGMCs absorb 25-45J.[3,4,15–17] Full sized Charpy specimens can be very difficult to fabricate out of various BMGs. A very large critical casting thickness is required, and ingots of at least 30 g would be required (very difficult with laboratory-scale equipment). Changing the sample geometry to 30x3x3 mm allows for rapid fabrication through suction casting in a mini arc melter. In the future, poor glass formers can also be directly compared, since this is an easier geometry for fabrication. Since the impact toughness of the BMG alloys is relatively low, plane-stress effects are absent even in the smaller beams, which means comparisons to tests done in larger specimens are proportional. The cross-sectional area of the compact samples in the current work is approximately 10 times smaller than full-sized samples, so the amount of energy absorbed would be nearly undectable using standard drop heights and hammer masses. Therefore, the Charpy tester was modified by reducing the drop height and the hammer mass, and the impact energy was measured both by dial and by instrumentation. Equating the potential energy of the hammer at the drop height ($PE=mgh$) with the kinetic energy of the hammer at impact ($KE = mv^2/2$), the initial velocity (v_0) of the hammer before the impact is found to be a function only of the initial drop height.

$$v_0 = \sqrt{2gh} \tag{2}$$

To instrument the machine, a 1 cm diameter cylindrical magnet was attached to a plastic arm on the side of the hammer pendulum. Two 1 cm diameter copper coils were mounted on a plate 70 mm apart, with their midpoint located at the impact location Figure 2-3a. The coils were wired to a digital oscilloscope connected to a computer. When the magnet attached to the hammer passes the first coil, a voltage that registers as a sinusoidal peak on the oscilloscope is created. During the impact with the specimen, the hammer slows down before it passes the second coil, creating a difference in the width of the sinusoidal peak. The energy absorbed by the sample can then be determined through

$$E = \frac{1}{2} m \left(v_0^2 - v_f^2 \right) \tag{3}$$

The velocity of the hammer can be determined by $v = \Delta x / \Delta t$, where Δt is the width of the sinusoidal pulse (the transit time of the magnet across the coil) and Δx is the width of the coil. Using the known standard drop height of the hammer, the initial velocity was calculated to be 3.46 m/s; using this known velocity, Δx was calculated to be ~1.0 cm for each coil by measuring the peak width. Using the known original impact energy and hammer height, the original effective mass of the hammer was calculated as 6.8 kg. An example of this procedure is demonstrated in Figure 2-3d. To accommodate the small-scale specimens, the energy of the hammer was reduced by decreasing the hammer mass to 2.7 kg and the initial velocity to 2.0 m/s. The new drop height was calculated to be 21 cm (from the measured velocity) and, thus, the total energy of the hammer was reduced from 41 to 5.6 J. For samples requiring more than 5 J to fracture, a second drop height was calibrated at 83 cm, imparting 22.2 J of energy at impact. A modified fixture to support the shorter samples was built as an insert into the existing

Charpy fixture, as shown in Figure 2-3b. The span length was thereby reduced from 50 to 20 mm for the small-scale tests.

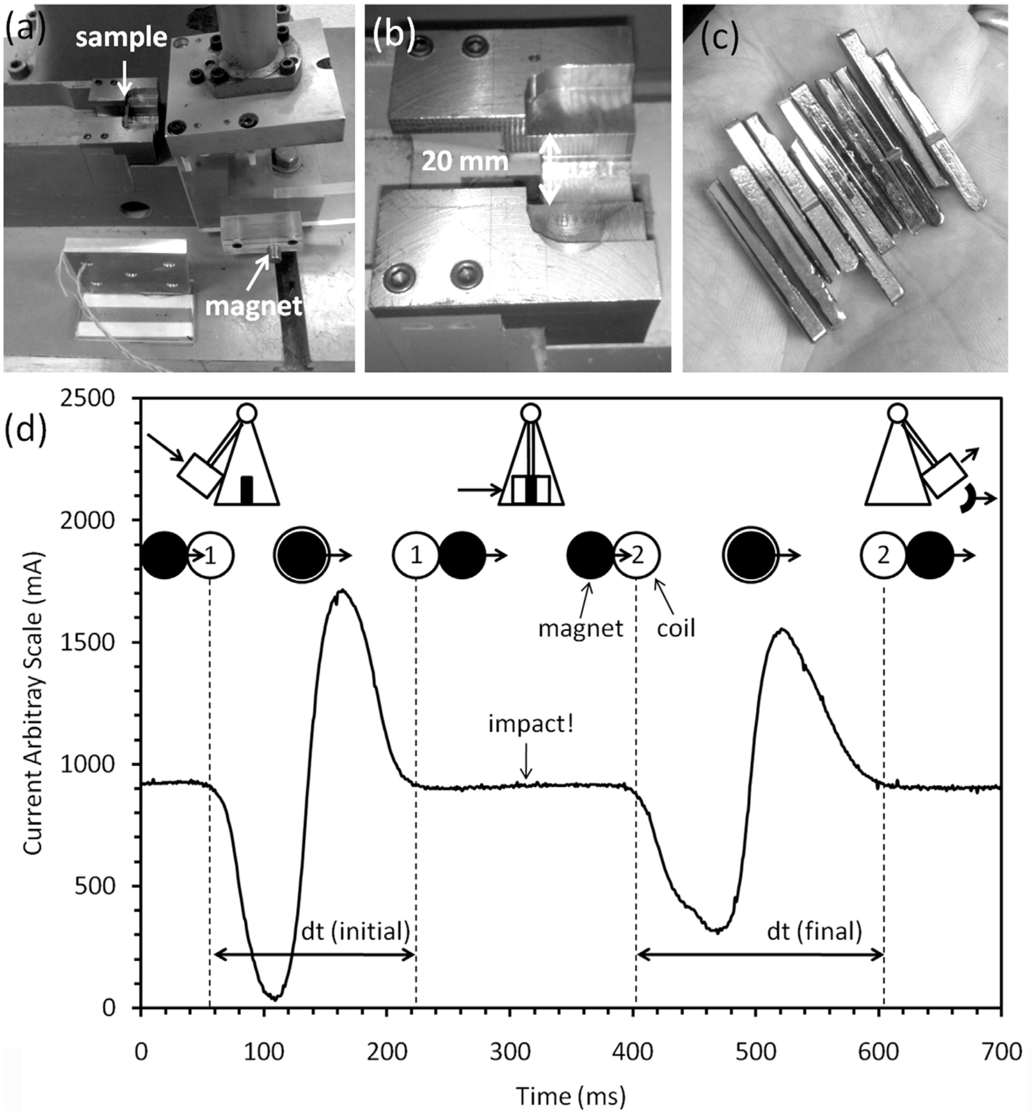

Figure 2-3: Instrumented small-scale Charpy testing. (a) The pendulum hammer has been stripped of excess mass to reduce the impact energy. A plastic extension has been built to hold the magnet. As the pendulum swings, the magnet passes a coil before and after impact, which registers a current. (b) The modified sample holder has a shorter span length of 20 mm for compact Charpy samples. (c) Suction cast (SC) samples of the alloy DV1. (d) Induced current obtained from an impact test on DH3 using a digital oscilloscope. The hammer’s speed is reduced during impact, which broadens the second peak. The width of the coils and magnets are known to be *dx* = 1 cm, so the velocity of the hammer can be determined through *v* = *dx/dt*. The energy during the impact is $E = 1/2\, mv^2$.

To calibrate the impact temperatures for the DTBT measurements, a series of heating curves was measured for each alloy. This was done by attaching a thermocouple to a specimen, holding the sample in liquid nitrogen until it reached equilibrium, quickly loading the sample into the testing setup, and then recording the temperature as a function of time as the sample heated due to contact with air and the sample fixture. This was repeated several times for each sample, so a plot of temperature vs. time could be obtained for each sample. The heating curve for DH3 is shown in Figure 2-4. The validity of the testing setup for measuring DTBT was verified by measuring an accurate DTBT temperature for 99.9% Sn.

Microstructures of the samples were analyzed through x-ray diffraction, backscattered scanning electron microscopy (QBSD-SEM), Rockwell hardness testing, acoustical measurements, and optical microscopy.

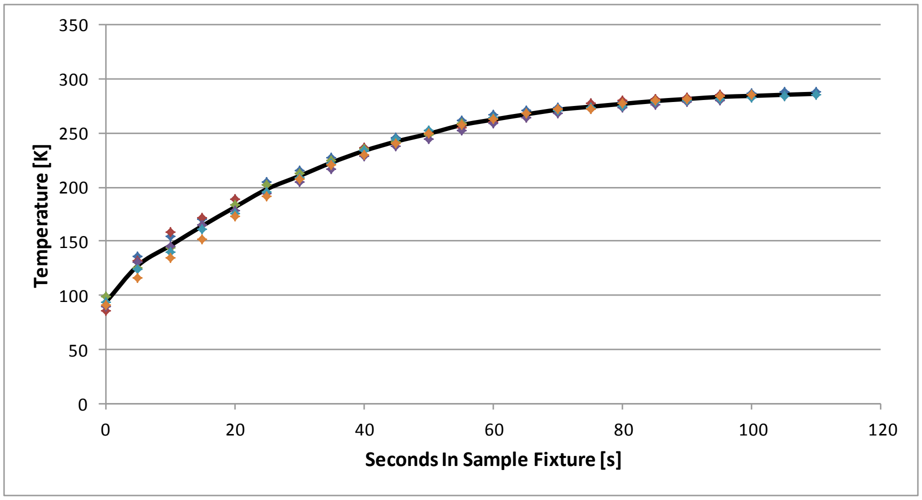

Figure 2-4: The temperature calibration curve for DH3 ($Zr_{39.9}Ti_{33.9}Nb_{7.6}Cu_{6.4}Be_{12.5}$).

Table 2-1: Physical & mechanical properties of samples measured via Charpy impact testing.

Name	Vol % of Crystal	Processing Method	CIT 300 K [J]	CIT 100 K [J]	CIT 300 K [J/cm²]	CIT 100 K [J/cm²]	σ_y [MPa]	σ_{max} [MPa]	Hardness [HRc]	ρ [g/cm³]	E [GPa]	σ_{max}/ρ
Vitreloy 1	0	SC	0.68	0.31	7.6	3.4	1700	1700	60	6.1	97.2	279
LM2	40	CCP	0.13	-	1.4	-	1000	1300	56.2	6.2	78.8	210
DV1	40	SC	1.31	0.33	14.6	3.7	1360	1430	58.3	5.2	92.4	275
DV1	40	SSF	4.82	-	53.6	-	1360	1430	50.8	5.2	92.4	275
DH3	67	SC	2.66	0.32	29.6	3.6	1100	1200	47.8	5.8	75.3	207
DH3	67	SSF	5.27	-	58.6	-	1100	1200	43.3	5.8	75.3	207
DH3-Xtal	100	X-tal	0.19	0.26	2.1	2.9	-	-	-	5.8	-	-
Ti-6-4	100	GD 5 STA	2.97	-	33	-	1100	1200	41	4.5	114	267
Al7075	100	T6	0.38	-	4.2	-	500	570	6	2.8	71.7	203
Al2024	100	T6	0.66	-	7.3	-	350	430	<1	2.8	72.4	155
SS 304	100	STA	9.49	-	105.4	-	220	500	<1	8	190	63
Sn 99.9%	100	X-tal	0.92	0.04	10.2	0.4	12.5	220	<1	5.8	41.4	38

σ_y, σ_{max}, and E for all crystalline alloys (other than DH3-matrix) were obtained from matweb.com. Processing routes for metallic glasses are defined as: SC (suction cast), CCP (commercially cast plate), and SSF (semisolid forged). CIT is Charpy impact toughness.

Results and Discussion

Influence of Processing Conditions of Charpy Impact Energy

Compact Charpy impact testing was performed on a total of 12 alloys: six containing an amorphous phase and six fully crystalline alloys. Table 2-1 gives compositions and processing conditions for the alloys tested. Figure 2-5 is a visual plot of the data in Table 2-1, which shows the impact energy (in Joules) for each sample along with impact energy per cross-sectional area (in J/cm²). On average, seven samples of each type were impacted to observe the effect of processing variation on impact energy, and the mean value for each alloy is shown in Figure 2-5 with a red circle. As a baseline, the monolithic BMG Vitreloy 1 (abbreviated Vit 1) was also evaluated via Charpy testing, as was done by several other groups.[3,4,16,17] Vit 1, which is the most widely studied and commercialized BMG to date (often under the trade name LM1), is approximately the amorphous matrix for the commercial composite LM2. Commercial quality alloy was obtained and were then broken up and suction cast into beams. The impact energy for the Vit 1 samples was determined to be 0.68 J, which is similar to the results from other studies when scaled to full size, despite differences in sample geometry and origin. The crack propagation through Vit 1 test samples also appears similar to the crack propagation through a fracture toughness tests done in other studies.[15]

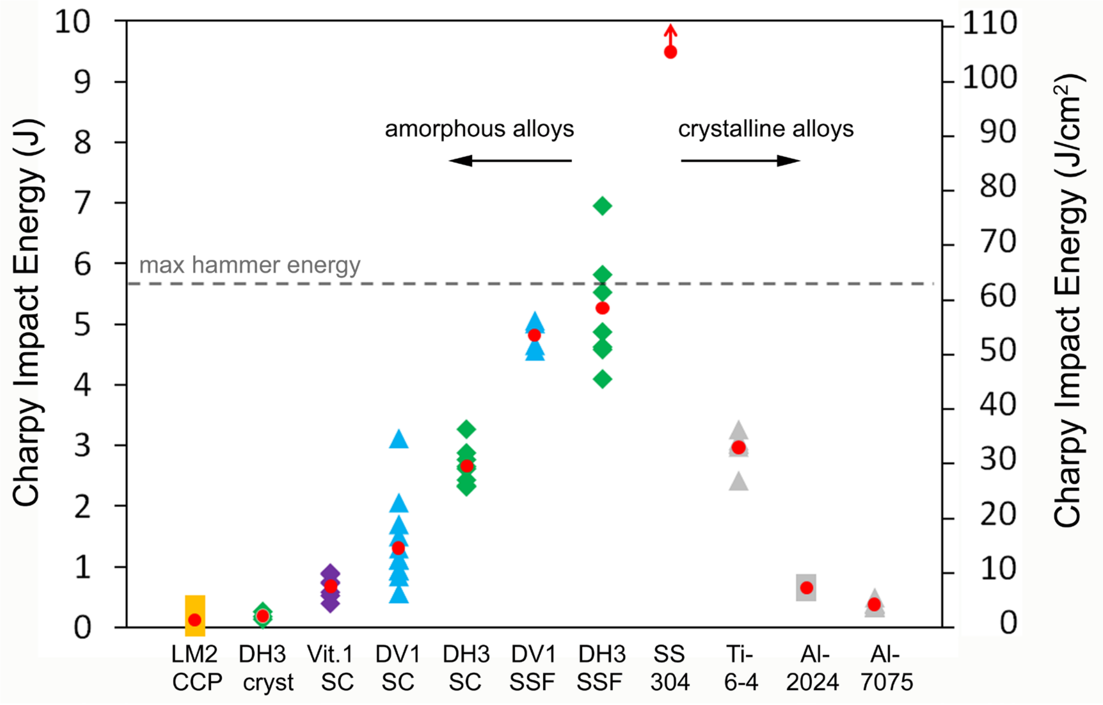

Figure 2-5: Compact Charpy impact toughness values from 11 alloys tested; one bulk metallic glass (BMG), six bulk metallic glass matrix composites (DH3, DV1, LM2) in various processing conditions, and four crystalline alloys. The processing conditions are commercially cast plate (CCP), crystalline (xtal), suction cast (SC), and semisolidly forged (SSF). The maximum hammer energy for the low drop height is displayed on the plot along with a scaled estimation of the full-sized Charpy toughness. On average, seven samples of each alloy were tested, and the average is plotted as a red circle.

Surprisingly, the commercially cast composite, LM2, had the lowest impact energy, with only 0.13 J absorbed. This is in spite of the alloy having approximately 40% volume fraction of a soft, crystalline dendrite phase. The brittle fracture surface typical of an the impact test is shown in Figure 2-6 and the microstructure is shown in Figure 2-7. Images of the fracture surface allow for an estimation of toughness. Qualitative estimates on the toughness of an alloy can be made by inspecting the fracture surface. High surface roughness, large numbers of shear bands, and the shear bands forming a long distance from the fracture surface are all indicative of a tough material. LM2's lack of roughness on the facture surface is indicative of a brittle material, which the impact energy measurements verify. It is well-known from other studies that commercially available LM2 contains a high ppm concentration of oxygen, which reduces the toughness of the matrix BMG considerably. This is the likely cause of the low observed toughness, despite the presence of the dendrites. Cracks forming in the matrix propagated without plastic shielding from the dendrites.

Figure 2-7a is a composite SEM micrograph of LM2 obtained via a quadrant backscatter detector (QBSD). This causes the dendrites to appear white in color versus the gray of the matrix due to the different composition, stemming from the Z-scattering differences. These samples were commercially produced by die-casting a liquid from a shot sleeve into a steel mold. This method has a relatively slow cooling rate, which allowed the microstructure to coarsen to levels similar to the SSF DV1 and DH3samples (shown in Figure 2-8a and Figure 2-9a). The dendrite arms are ~10 μm thick, and the spacing of the arms is between 1-5 μm. The main branches of the dendrites are ~100 μm in diameter, and are spaced several hundred microns apart. Unlike the other SSF samples, though, LM2 is not extensively toughened by the coarsening, as the crack cleaved through the sample without any significant branching or blunting. A limited number of shear bands can be seen on the surface normal to the fracture, but they only extend between

5 µm to 50 µm away from the crack. As expected, the low commercial purity of the alloys makes the matrix brittle and limits the glass forming ability of the alloy. This causes some brittle intermetallic phases to nucleate during solidification, as seen in Figure 2-7c. In combination, the high-oxygen matrix and the presence of the brittle intermetallic phases result in a very low toughness.

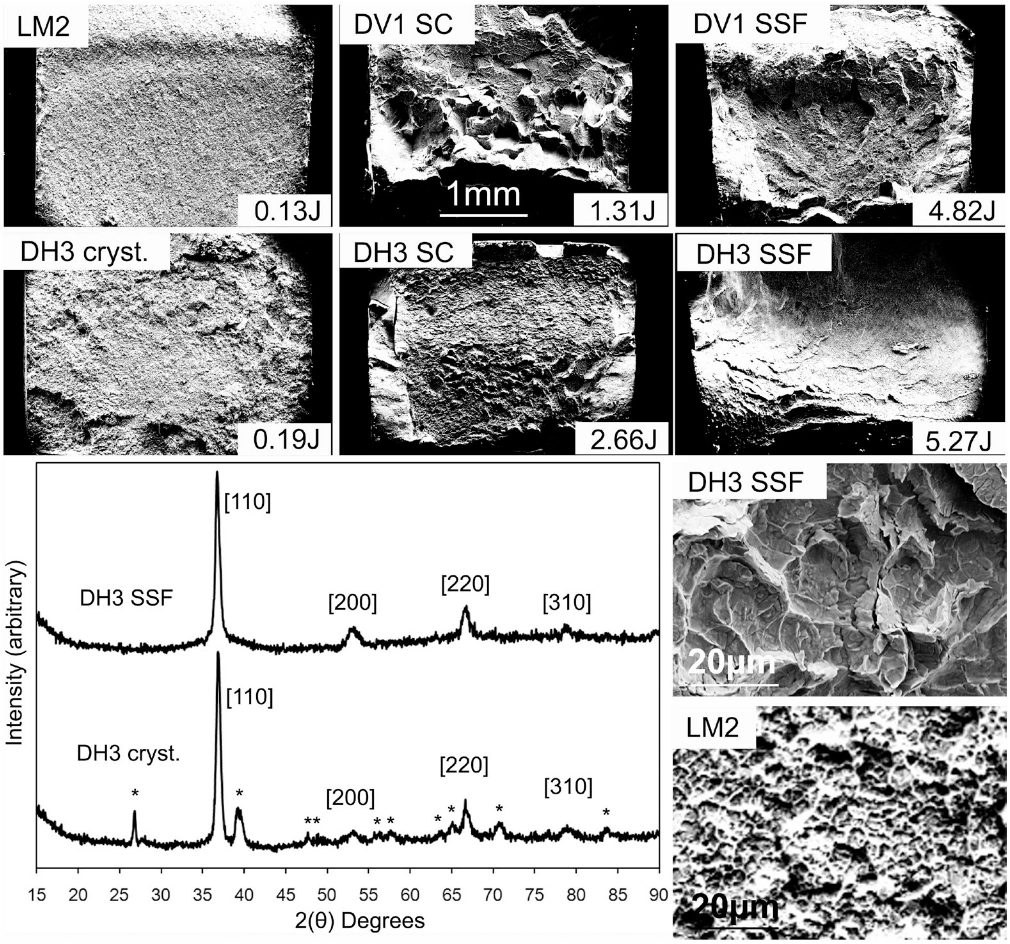

Figure 2-6: Fracture surfaces from six BMGMC samples tested in this study, along with their impact energy. X-ray scans from SSF DH3 and the completely crystalline state are also shown. Although the body-centered cubic dendrites remain in the crystalline sample, the matrix is no longer amorphous, as evident from the numerous starred peaks. Also shown are magnified fracture surfaces from SSF, DH3, and LM2, showing the difference in the fracture pattern. All images are of the fracture surface taken with backscattered electrons in a SEM.

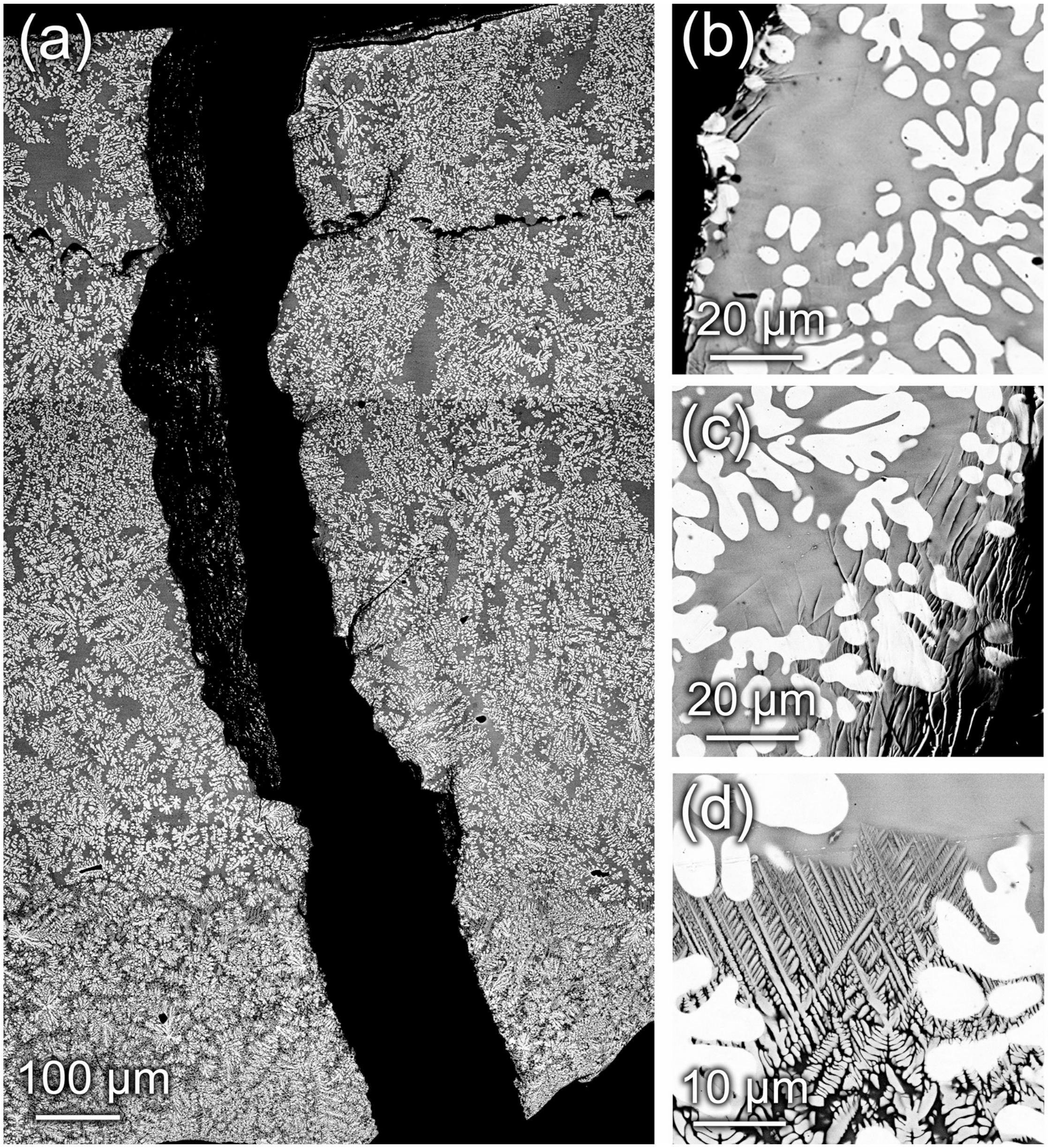

Figure 2-7: (a) A backscattered SEM micrograph showing a fractured specimen of commercially cast LM2. Despite the large, coarse dendrites, other factors (like oxygen content and partial crystallization) make this the most brittle alloy tested. (b) The edge of the crack from a region in (a) demonstrating very little toughness. (c) Another region near the edge of the crack showing that several shear bands have formed. (d) A region where the matrix has crystallized into an unknown brittle phase.

The Ti-based BMGMC DV1 was the first non-commercial composite tested. It is notable for its large amount of tensile strain to failure (~15%) and low density (5.17 g/cm^3).[15] Ten samples were suction cast, and their impact energy is plotted as the blue triangles in Figure 2-5. SC DV1 has a large amount of variability, with impact energies between samples spanning nearly an order of magnitude (a low of 0.56 J, high of 3.1 J, and an average of 1.3 J). This is likely caused by the suction casting method, during which molten material is sucked into a mold and there is the possibility of small voids due to the turbulent flow. There are also inconsistencies in the solidification behavior of various DV1 samples as fabrication conditions do not permit identical castings. Temperature control is not perfect, so some would be cast from higher temperatures causing a slower cooling rate and larger dendrites. This would not have been as much of a problem for SC Vit 1, since it lacks the dendritic microstructure seen in the composites and has less variability when cast. To study the effects of dendrite refinement on DV1, an ingot was heated into the semi-solid regime (~950 °C), and held isothermally for ~1 minute to coarsen the microstructure, then forged between two copper plates into a 3mm thick plate (as demonstrated in Ref 18). Semisolidly forging DV1 had a significant effect on impact toughness, with the average energy absorbed increasing by nearly four times to 4.8 J. Scatter was also reduced as a function of both the coarsened microstructure and that the samples were cut from the same plate. Figure 2-8 demonstrates the difference between fractures in the two methods of processing DV1. Both samples exhibit a rough fracture surface, but the SSF sample exhibits significant shear lips on the edges perpendicular to the notch. Figures 2-8a and 2-7d show composite images of the crack path through the DV1 SSF and SC samples, respectively. The microstructure for the SSF sample is actually visible to the unaided eye, as a result of the coarsening imparted by semi-solid processing. Damage can be seen 1-2 mm away from the crack edge, and mostly consists of closely spaced shear bands (<10 µm separation) with significant

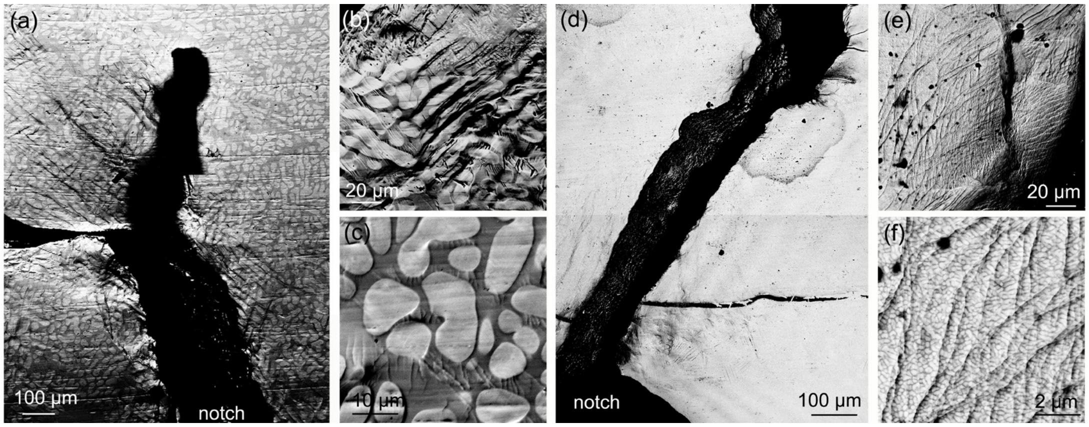

Figure 2-8: Backscattered SEM micrographs from the BMGMC DV1 (40% dendrite). (a) Crack originating at the notch and then propagating through a SSF sample during a compact Charpy test. (b),(c) Higher magnification of shear bands interacting with the Ti-based dendrites (e) Crack propagating through a SC sample during compact Charpy test. (e),(h) Higher magnification micrographs of shear bands in the SC sample along with the nominal microstructure.

damage visible in the dendrites (Figure 2-8b and Figure 2-8c). Dendrite arm spacing is 5-10 μm, with thicknesses ~10-15 μm. The length of a dendrite is ~100 μm, and the arm spacing is only a few microns. In contrast, the SC sample shows much less branching and blunting, with shear bands only observed ~100-200 μm from the edge of the crack. Although many shear bands are observed (Figure 2-8f) compared to an alloy such as Vit 1, there are significantly less than in the SSF sample. The microstructure from the SC sample (Figure 2-8f) is an order of magnitude smaller than the SSF sample, as a result of casting from above the liquidus and rapid quenching. The overall dendrite size is only a few microns, with the arms themselves being approximately 0.5-1 μm. Figure 2-8f is a highly magnified image of the dendrites with shear bands that occurred during fracture. It should be noted that although the SC sample of DV1 had energy absorption 25% less than that in the SSF sample, it is still not a brittle fracture when compared to LM2 and Vit 1. SC samples of DV1 still exhibit ten times higher impact toughness than commercial LM2. Thus, even though the small dendrites aren’t as effective at blunting and redirecting the crack tip as the coarser dendrites, they still require a significant amount of energy to fracture.

DH3, the Zr-Ti based BMGMC, was the next impact tested composite. This alloy is notable for its high fracture toughness (>173 MPa $m^{1/2}$) and fatigue endurance limit (25% of yield strength), mostly caused by the increased volume fraction of soft dendrites (66%).[15] DH3 specimens were SC and SSF, similar to DV1, but in addition one set of samples intentionally had the matrix crystallized (DH3-xtal) by slowly cooling from the semi-solid region (XRD scan shown in Figure 2-6). The XRD scan from DH3 is a typical scan for all of the composites which exhibit both a large, broad amorphous hump as well as bcc diffraction peaks. The DH3-xtal XRD scan shows how upon the matrix's crystallization, additional diffraction peaks can be seen from the formation of intermetallic phases. XRD scans of other alloys are not shown.

The SC samples of DH3 show the reverse trend during impact testing compared to the SC samples of DV1. Instead of a large scatter, the impact energies are clustered closely to the average of 2.7 J. It is likely due to the higher dendrite fraction (and thereby higher liquidus temperature) that the mini arc melter was unable to fully melt the alloy prior to suction casting, and as a result some dendrite refinement was allowed to take place. This created a more uniform microstructure during casting, which should result in less scatter in impact energies. The SSF DH3 samples also exhibited significantly higher average impact energies than the SC samples (5.4 J), although the improvement was not as dramatic as with DV1. The amount of energy absorbed by SSF DH3 was actually high enough that a larger drop height was required to break the samples. Similarly to DV1, the microstructure difference in DH3 SC and SSF varied by approximately an order of magnitude. The nominal microstructure from the SSF samples is shown in Figure 2-9b and Figure 2-9g, with dendrite arms 10-15 µm wide and spaced ~5 µm apart. The overall dendrite size is 100-200 µm. The scale of both DV1 and DH3's SSF samples are similar, with DH3 having a larger fraction of dendrites. In contrast, the dendrites from SC DH3

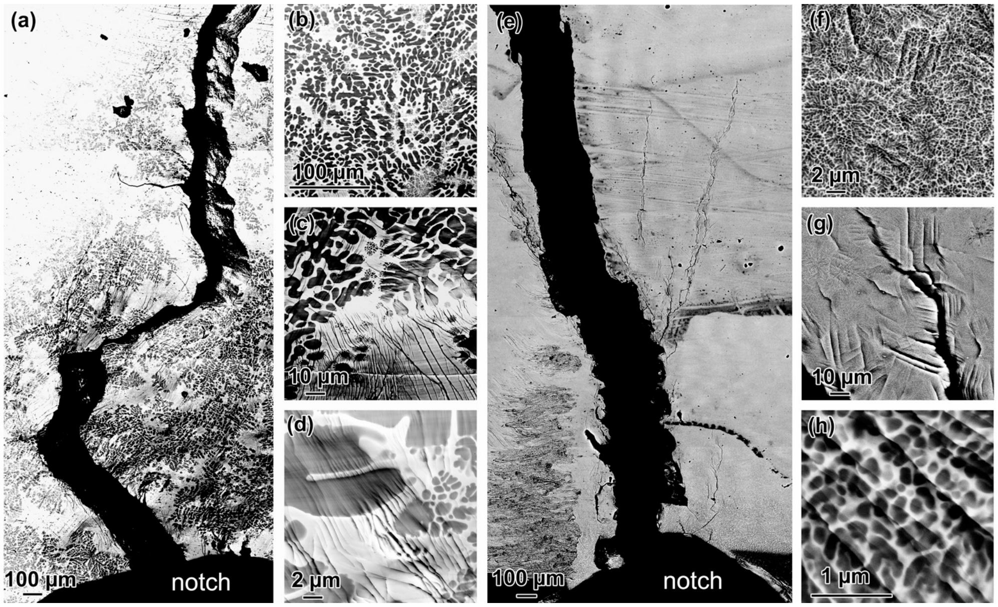

Figure 2-9: (a) Crack arrest and branching after impact in a SSF sample. (b) Near the edge of the crack, many shear bands have formed and been arrested by the soft dendrites. (c) Magnification of a region in (a) demonstrating that even far away from the crack, shear bands still form in the glass matrix. (e) Crack propagating through a SC sample of DH3 and (f),(g) higher magnification images of the shear bands and microstructure.

have an arm size of 0.5-1 µm, and a spacing of only a few hundred nanometers (Figure 2-9f and Figure 2-9h). The overall dendrite size is on the order of 1-5 µm in diameter.

Four common crystalline alloys were also tested in the same geometry for direct comparison with the amorphous alloys, since a smaller than standard Charpy size was used. The aerospace aluminum alloys Al-2024-T6 and Al7075-T6 exhibited impact energies of 0.66 and 0.38 J, with very low observed scatter. Ti-6-4's impact energies were close to that of the SC samples of DH3, but were surpassed by both SSF samples of DV1 and DH3. The fourth crystalline alloy tested was a completely crystallized sample of DH3. It was fabricated via SSF, then annealed in a radio frequency (RF) induction coil until crystallization was visible on the surface. Crystallinity was verified by XRD (Figure 2-6), and no amorphous content was detected via differential scanning calometry (DSC). It is not pictured, but the microstructure of the sample is similar to Figure 2-7d: there are large coarsened dendrites, but the amorphous matrix is replaced by a fine eutectic. Crystallizing the matrix resulted in a measured impact energy of 0.19 J. This is approximately 7% of the SC samples, 3% of the SSF samples, but still higher than the 0.13 J of the LM2 BMGMC. These results underline the importance of ensuring a vitrified and tough matrix. By crystallizing the glass, the impact toughness of the matrix goes down substantially, with a corresponding decrease in the critical size at which cracks form (100 μm in the glass to ~10 nm in the crystalline eutectic.[15]). Since self-propagating cracks form at such small lengths in the crystalline matrix, the dendrites, regardless of size, have no effect on toughening, since cracks simply bypass them and propagate through the matrix unhindered. DH3's 67% volume fraction of crystal still experiences an order of magnitude decrease in toughness when the matrix is crystallized. Figure 2-6 shows fracture surfaces of all DH3 samples (SC, SSF, xtal) along with higher magnification images comparing the dimpled fracture pattern between tough SSF DH3 and brittle LM2 samples. As expected, the brittle sample exhibits approximately an order of magnitude smaller dimple pattern than the toughest composite alloy (~20 μm versus ~2 μm). The fracture surfaces from the composites in order of increasing toughness from the crystalline DH3 sample to the SC sample, to the SSF sample. In each case, the roughness increases with toughness, as does the size of shear lips on the sample's edge (nearly 1mm in SSF DH3).

Finally, rolled samples of 304 stainless steel were tested, resulting in an average impact energy of 9.5 J. These samples exhibited sufficiently high toughness in that the hammer was not able to easily fracture the samples. This caused the hammer to vibrate significantly, and likely added to large error in measurement. Because of this, only the average value is plotted in Figure 2-5.

Ductile to Brittle Transition in BMGMCs

To investigate the presence of a DTBT temperature in BMGMCs, further Charpy impact testing was performed from room temperature down to liquid nitrogen temperatures. Figure 2-10 plots the measured impacted energy versus the temperature of the sample at time of impact. As in the previous tests, where crystalline alloys were impact tested to verify the setup, in this section pure Sn was impacted to verify that the DTBT temperature is similar to what is measured in full-sized specimens. The Sn 99.9% curve recreates that from the literature[19] well, with a roughly linearly decreasing toughness from 150 to 300 K, and the DTBT temperature from 130 to 150 K (illustrated by a shaded area). Once below the transition temperature, the toughness decreases linearly to a value roughly 2% of its room temperature value. The small sized specimens were able to accurately replicate the shape of the low temperature toughness of Sn, but the test underestimates the actual impact energies.

Also displayed in Figure 2-10 are two Vitreloy 1 curves for toughness versus temperature. The first (with solid triangles) was produced in this work, while the other (open triangles) is from the literature[4]. The impact energies from literature were performed on specimens with 6x3x50 mm geometry. In both curves, the toughness decreases roughly linearly with temperature and does not exhibit a DTBT. At 100 K, Vit 1 retains 35% of its room temperature toughness, while the toughness of Sn has decreased by 98% from its room temperature toughness. The rate of Vit 1's decrease in toughness is calculated to be ~0.02 $\mathrm{J\ cm^{-2}K^{-1}}$.

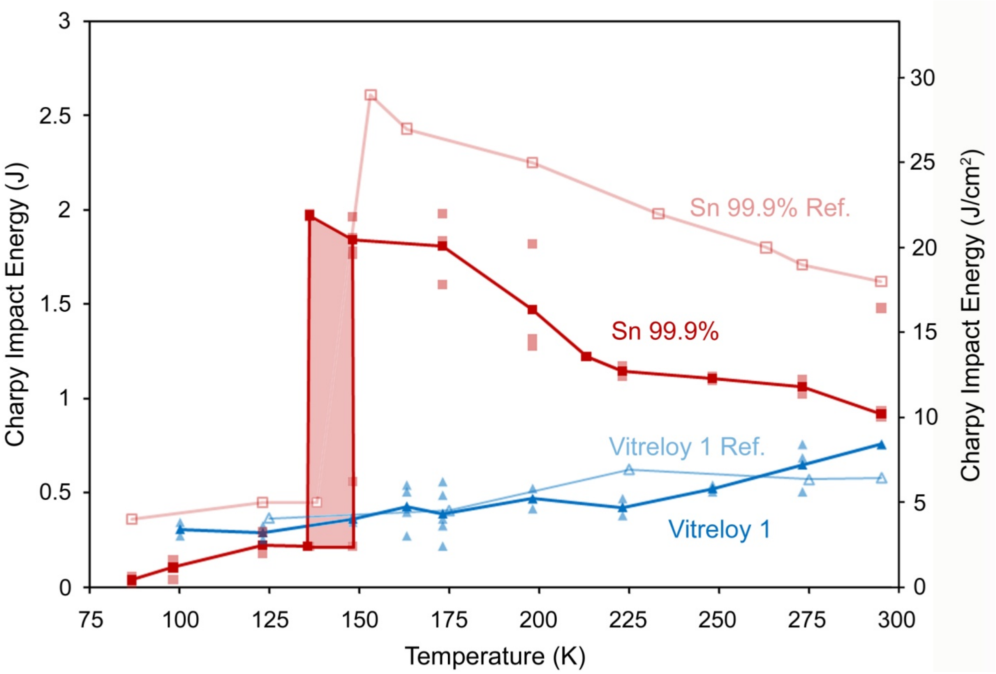

Figure 2-10: Charpy impact toughness vs. temperature for pure Sn and the BMG Vitreloy 1 compared with data obtained from References [19] and[4]. The plot shows that the compact impact setup used in this work recreates the correct DTBT temperature in Sn and reproduces the shape of the curves from literature, despite the smaller specimen size. An estimate of the full-sized Charpy toughness is shown on the right axis. All the data is shown.

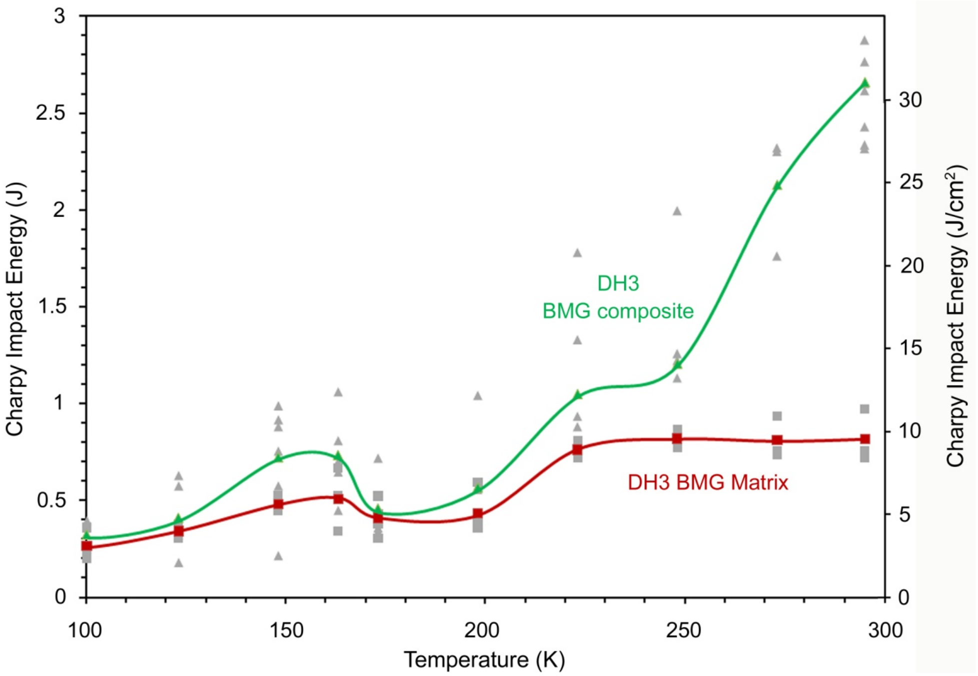

Figure 2-11: Charpy impact toughness vs. temperature for the BMGMC DH3 and its glass matrix, made separately. The curves represent the averages all of the data, which are also shown. Both alloys were produced via suction casting and notched identically.

Figure 2-11 is a plot of temperature vs. toughness for DH3, the BMGMC with 66% soft crystalline dendrite, along with an alloy which approximately mimics its glassy matrix.[20] The BMGMC alloy DH3 exhibits excellent room temperature toughness and ductility, but is comprised of a bcc crystalline phase that is expected to undergo a DTBT. It is known that brittle metallic phases in a glass can make the BMGMC significantly more brittle than the parent glass (as was demonstrated above). Figure 2-11 essentially confirms this hypothesis by showing that the toughness of DH3, while much higher than its matrix BMG at room temperature, quickly loses its toughness and essentially behaves like a monolithic glass. At room temperature, DH3 absorbs more than three times more energy than its glass matrix; however, the impact toughness decreases rapidly for the first 100 K of cooling due to the embrittling of the bcc dendrites. Around 175 to 200 K the DH3 and DH3-Matrix curves virtually converge, demonstrating that the matrix controls the toughness because the dendrites can no longer arrest shear band growth. DH3-Matrix exhibits a similar decrease in toughness compared to Vit 1, maintaining ~30% of its room temperature toughness at 100 K. DH3, the BMGMC, only maintains 15% of its room temperature toughness, which is obviously lower because it starts with a much higher toughness. Despite the performance, DH3's DTBT is still significantly smaller than that of Sn's, which results in only 2% toughness retention at 100 K. Both DH3 and DH3-Matrix have an impact toughness of ~0.25 J (2.7 J cm^{-2}), an order of magnitude higher than Sn's. Earlier in this chapter it was demonstrated that processing techniques can significantly improve the room temperature toughness of a BMGMC, however, that toughening is only worthwhile for temperatures above the DTBT. This is not necessarily a bad result; BMGMCs' superior room temperature toughness remains for the first 100 K below ambient temperature, and the amorphous matrix allows it to retain a moderate amount of toughness even at cryogenic temperatures. Therefore, the BMGMCs are never more brittle than monolithic BMGs with decreasing temperature, and both have respectable toughness at cryogenic temperatures compared to metals that exhibit a DTBT.

Another unexpected result seen in Figure 2-11 is a slight hump in toughness around 163 K. Both DH3 and DH3-Matrix exhibit a slight increase in toughness at that temperature, followed by decreasing toughness at lower temperatures. Since the hump was observed for both alloys, it is likely a real phenomenon occurring in the glass matrix. A similar hump has not to date been observed in Vit 1, where a number of cryogenic studies have been performed.

Figure 2-12 is a collection of SEM micrographs illustrating the differences in the appearance of the fracture surface at 100, 163, and 300 K in the BMGMC DH3. Figure 2-12a-c shows micrographs from the surface of three specimens that were polished to a 0.02 µm finish prior to testing. The notch is at the top of each image, and the crack was driven downwards during impact. Figure 2-12a, a 300 K impact, exhibits a large amount of deformation and crack branching, with shear bands observed a distance of 950 µm from the edge of the crack. The typical shear band spacing, shown at two different magnifications in Figure 2-12d and e, was found to be 2.75 µm. At 163 K (Figure 2-12b) some crack branching is still apparent, although there are fewer shear bands visible on the surface (only up to 600 µm from the crack) and they have a larger spacing of 3 µm (Figure 2-12f). At 100 K (Figure 2-12c), the crack does not branch at all, and cleaves the sample without significant deformation. The few visible shear bands only extended 150 µm away from the crack, and had a spacing of 9.6 µm.

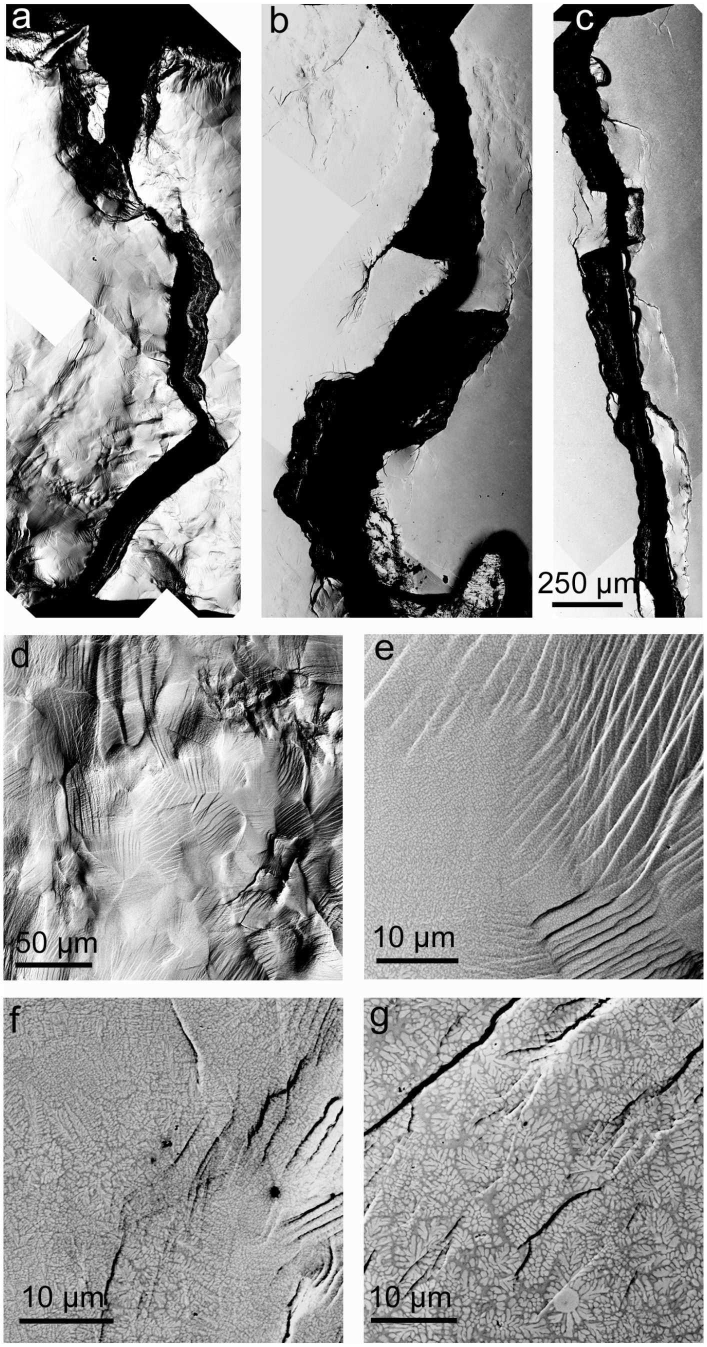

Figure 2-12: (a-c) SEM micrographs from the surface of polished Charpy specimens in the BMGMC DH3 showing how the crack morphology changes with temperature. (a) 300K, (b) 163 K, and (c) 100 K. (d-e) Enlarged micrographs of the shear bands on the surface of the DH3 sample impacted at room temperature. Similar images are shown for cryogenic specimens, (f) 163 K and (g) 100 K.

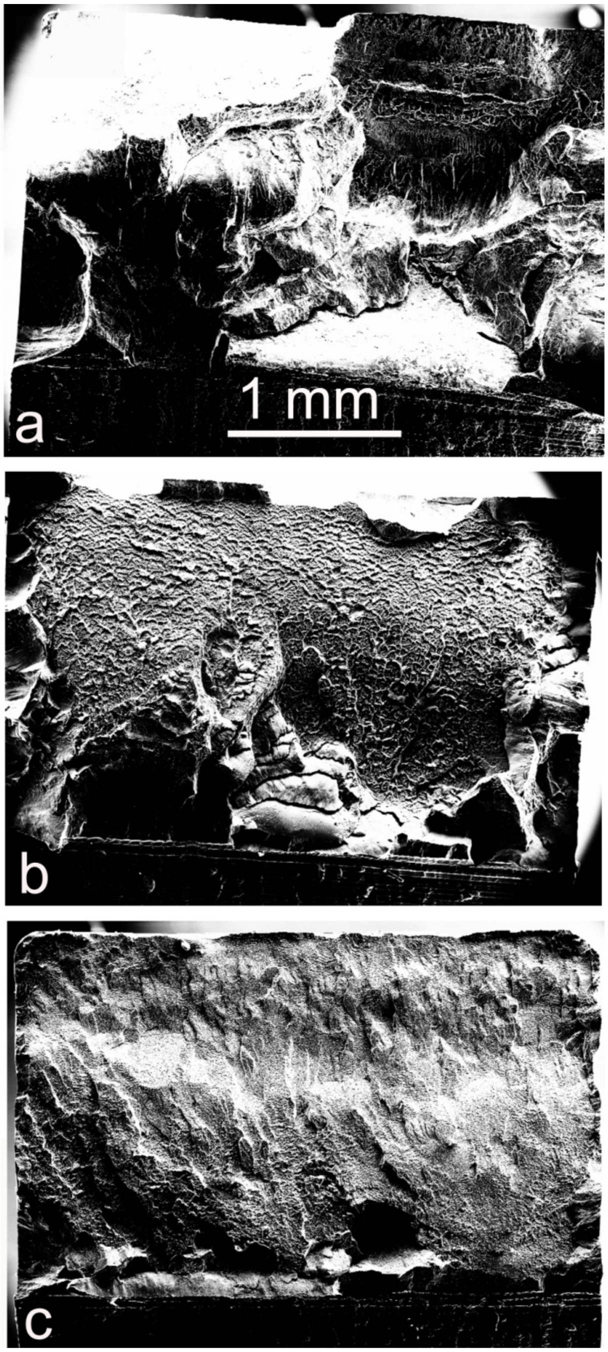

Figure 2-13: (a) SEM micrograph of the fracture surface from the monolithic BMG DH3-Matrix impacted at 300K. (b) DH3-Matrix 100 K. (c) Fracture surface from BMGMC DH3 at 100 K. In all samples the notch is at the bottom of the images.

Plastic flow of a material is a thermally activated process, so, by reducing the temperature, the number of shear bands which can be formed should decrease. Another assessment of toughness is the length of the crack-edge per mm of sample, called *l*, obtained from Figure 2-12a-c. In a perfectly brittle fracture, no crack branching would be observed, and the crack would travel perpendicular to the sample, leading to *l* = 1. In a tough material, the track turns due to blunting and plastic shielding, leading to *l* > 1. In the coldest sample, impacted at 100 K, *l* = 1.10 mm/mm. At 163 K, *l* = 1.38 mm/mm, and at 300 K, *l* = 1.36 mm/mm. The lowest temperature impact has the shortest crack path, with the crack only traveling an extra 10% of distance in the material versus a pure cleavage fracture. The two higher temperature impacts both had similar crack lengths, although they had significantly different average energies of fracture. The higher concentration of shear bands in the 300 K sample can explain its higher toughness. Fracture surfaces of DH3 and DH3-Matrix are shown in Figure 2-13 at (a) 300 K and (b) 100 K. As expected, as the temperature during fracture decreases the fracture surface decreases in roughness, correlating with the decrease in toughness. Figure 2-13c is the fracture surface from DH3 at 100 K. It can be seen to be similar to the DH3-Matrix, as its surface is fairly smooth and lacks a large amount of roughness.

The final alloy tested was the Ti-based BMGMC DV1, which has a lower volume fraction of dendrites than DH3 (40%), but still is reinforced with a bcc phase. Five impacts at 100 K and 300 K were performed. The average impact energy at 100 K was found to be 0.33 J (3.7 J cm^{-2}), compared with 1.31 J (14.5 J cm^{-2}) for the 300 K sample.

Table 2-2: Summary of DH3 DTBT impacts

Temperature [K]	Shear Band Spacing [µm]	Max Shear Band Distance from Crack [µm]	ℓ [mm/mm]	CIT [J]	CIT [J/cm²]
100	9.6	150	1.10	0.32	3.6
163	3.0	600	1.38	0.72	8.5
300	2.75	950	1.36	2.66	29.6

CIT is Charpy impact toughness, and *l* is the crack-edge per mm of sample.

Conclusions

In this study a series of miniaturized Charpy experiments were performed. The influence of processing on the microstructure of BMGMCs was used to vary the microstructure of the two alloys DV1 and DH3. Their impact toughness was measured to be greatest when semisolidly forged. This technique allowed for much greater dendrite refinement than suction casting, which, in turn, increased impact toughness. The commercially cast LM2, while a BMGMC, performed poorly. This was due to the growth of a brittle crystalline phase within the amorphous matrix, with similar results to the massive decrease in toughness experienced by DH3-xtal. With proper fabrication, DV1 and DH3 can absorb more impact energy than Ti-6Al-4V, Al-2024, and Al-7075.

Impact toughness was also measured across a range of temperatures for Vitreloy 1, DH3, DH3-matrix, and Sn. The measurements for Vitreloy 1 and Sn matched well with the values from the literature. Vitreloy 1 was found to slowly decrease in toughness as the impact temperature was reduced. Sn experienced a DTBT between 130 to 150 K. DH3-matrix's temperature sensitivity was similar to Vitreloy 1's, with a gradual decrease as the temperature was reduced. DH3 was very tough at ambient temperatures. It suffered rapid degradation upon cooling, but always performed at least as well as its amorphous matrix. This study demonstrated how even when a bcc crystal undergoes a DTBT it remains possible to mitigate the effects by constraining its failure within another tough material.

References

(1) ASTM Standard E23, 2007, “Standard Test Methods for Notched Bar Impact Testing of Metallic Materials” **2007**.

(2) Nayar, A. *Testing of Metals*; McGraw-Hill Education, 2005; p. 202.

(3) Raghavan, R.; Murali, P.; Ramamurty, U. Ductile to brittle transition in the Zr41.2Ti13.75Cu12.5Ni10Be22.5 bulk metallic glass. *Intermetallics* **2006**, *14*, 1051–1054.

(4) Raghavan, R.; Murali, P.; Ramamurty, U. On factors influencing the ductile-to-brittle transition in a bulk metallic glass. *Acta Mater.* **2009**, *57*, 3332–3340.

(5) Li, H.; Tao, K.; Fan, C.; Liaw, P. K.; Choo, H. Effect of temperature on mechanical behavior of Zr-based bulk metallic glasses. *Appl. Phys. Lett.* **2006**, *89*, 041921.

(6) Huang, Y.; Shen, J.; Sun, J.; Zhang, Z. Enhanced strength and plasticity of a Ti-based metallic glass at cryogenic temperatures. *Mater. Sci. Eng. A* **2008**, *498*, 203–207.

(7) Yu, P.; Wang, R. J.; Zhao, D. Q.; Bai, H. Y. Anomalous temperature dependent elastic moduli of Ce-based bulk metallic glass at low temperatures. *Appl. Phys. Lett.* **2007**, *91*, 201911.

(8) Qiao, J. W.; Liaw, P. K.; Zhang, Y. Ductile-to-brittle transition of in situ dendrite-reinforced metallic-glass–matrix composites. *Scr. Mater.* **2011**, *64*, 462–465.

(9) Cheng, J. L.; Chen, G.; Xu, F.; Du, Y. L.; Li, Y. S.; Liu, C. T. Correlation of the microstructure and mechanical properties of Zr-based in-situ bulk metallic glass matrix composites. *Intermetallics* **2010**, *18*, 2425–2430.

(10) Lim, K. R.; Na, J. H.; Park, J. M.; Kim, W. T.; Kim, D. H. Enhancement of plasticity in Ti-based metallic glass matrix composites by controlling characteristic and volume fraction of primary phase. *J. Mater. Res.* **2010**, *25*, 2183–2191.

(11) Park, J. M.; Jayaraj, J.; Kim, D. H.; Mattern, N.; Wang, G.; Eckert, J. Tailoring of in situ Ti-based bulk glassy matrix composites with high mechanical performance. *Intermetallics* **2010**, *18*, 1908–1911.

(12) Guo, S. F.; Liu, L.; Li, N.; Li, Y. Fe-based bulk metallic glass matrix composite with large plasticity. *Scr. Mater.* **2010**, *62*, 329–332.

(13) Zhu, Z.; Zhang, H.; Hu, Z.; Zhang, W.; Inoue, a. Ta-particulate reinforced Zr-based bulk metallic glass matrix composite with tensile plasticity. *Scr. Mater.* **2010**, *62*, 278–281.

(14) Qiao, J. W.; Feng, P.; Zhang, Y.; Zhang, Q. M.; Liaw, P. K.; Chen, G. L. Quasi-static and dynamic deformation behaviors of in situ Zr-based bulk-metallic-glass-matrix composites. *J. Mater. Res.* **2010**, *25*, 2264–2270.

(15) Hofmann, D. C.; Suh, J.-Y.; Wiest, A.; Duan, G.; Lind, M.-L.; Demetriou, M. D.; Johnson, W. L. Designing metallic glass matrix composites with high toughness and tensile ductility. *Nature* **2008**, *451*, 1085–9.

(16) Shin, H. S.; Kim, K.-H.; Oh, S.-Y. Fracture behavior of Zr-based bulk metallic glass under impact loading. *Int. J. Mod. Phys. B* **2006**, *20*, 4359–4364.

(17) Shin, H.; Kim, K.; Jung, Y.; Ko, D. Impact fracture behavior of Zr-based bulk metallic glass using subsize Charpy specimen. *Adv. Fract. Strength* **2005**, *297-300*, 1356–1361.

(18) Hofmann, D. C.; Kozachkov, H.; Khalifa, H. E.; Schramm, J. P.; Demetriou, M. D.; Vecchio, K. S.; Johnson, W. L. Semi-solid induction forging of metallic glass matrix composites. *JOM* **2009**, *61*, 11–17.

(19) Ratchev, P.; Vandevelde, B.; Verlinden, B.; Allaert, B.; Werkhoven, D. Brittle to Ductile Fracture Transition in Bulk Pb-Free Solders. *IEEE Trans. Components Packag. Technol.* **2007**, *30*, 416–423.

(20) Duan, G.; Wiest, A.; Lind, M. L.; Li, J.; Rhim, W.-K.; Johnson, W. L. Bulk Metallic Glass with Benchmark Thermoplastic Processability. *Adv. Mater.* **2007**, *19*, 4272–4275.

Chapter 3 - Capacitive Joining and Assembly of Bulk Metallic Glass Matrix Composites

Strong, robust joining of metal components is a key consideration in the fabrication of complex assemblies and consumer products. Developing optimal welding and joining practices for each class of materials is critical for their integration into products. Bulk metallic glasses (BMGs) are a relatively new class of materials with exceptional mechanical properties. However, they lack an obvious joining process, owing to their unique amorphous microstructure. BMGs are known for their combination of ultra-high strength, high hardness, large elastic limit, and low melting temperatures that allow them to be cast or molded like polymers. These properties have been widely exploited in applications such as electronic cases and golf clubs, but have been mostly relegated to small, near-net shape parts that are components of larger structures. This is due to a number of factors, including the difficulty of casting larger parts, material cost, and the low toughness of BMGs. Recently, a new class of BMG composites has emerged with soft crystalline dendrites. These dendrites allow the material to deform plastically (up to 10% elongation prior to failure), resulting in a material with ultra-high toughness that still preserves the strength of the metallic glass.[1] These alloys have been semi-solidly processed into panels and cellular structures and been shown to possess some of the highest energy-absorbing capacities of any metal structure.[2,3] Panels of the current BMG composites are already under investigation in energy-absorbing applications, such as orbital debris shielding for spacecraft and satellites, crushable landing foams for extra-terrestrial rovers, and as panels on military vehicles and vessels.[4] The ability to weld these structures together to form wider panels or thicker cellular structures is alluring for future structural applications. Similarly, the ability to weld monolithic BMGs, especially in small parts, has the potential for greatly enhancing their functionality in commercial applications. In this chapter, it is demonstrated that by flash heating and cooling joints of BMGs or BMG composites using capacitive discharge, unions can be achieved with properties nearly indistinguishable from the parent material, opening up the possibility for continuous BMG structures to be fabricated from multiple pieces.

Currently, the joining of BMGs in commercial hardware is eschewed in favor of casting net-shape parts that can then be snapped or bonded together with epoxy. Conventional welding or joining techniques used for many crystalline metals are difficult to apply to BMGs because high rates of cooling are required to vitrify the part. Therefore, any joining operation must both heat and cool the metal quickly, as any heat affected zone (HAZ) reaching temperatures in excess of the glass transition is in danger of crystallization. Many techniques have been attempted for welding BMGs, including friction welding, friction-stir welding, explosive welding, electron beam welding, and laser joining.[5–8] Friction welding, where samples are generally rotated together to generate enough frictional heating to allow for joining, requires samples with axial symmetry, as well as finish-machining operations to remove flashing. Friction stir welding, which involves insertion and translation of a rotating pin tool to mechanically stir material into a welded region, is typically limited to butt welds (although NASA has used the technique for orbital welding of rocket bodies) and has low cooling ability unless the sample is submerged.[9] Explosive welding is not practical for precise joining of parts. While laser welding is very precise, the required dwell time of the laser is long, and results in cooling rates slow enough to crystallize all but the most robust glass formers.

To practically weld BMGs (and, by extension, BMG composites) with precision, a method is needed to rapidly heat and join two BMG interfaces while retaining the ability to quench the HAZ faster than the critical cooling rate for glass formation. One solution involves the use of electrical current pulses, and associated Joule heating, to rapidly heat and join BMG parts while allowing the part to be quickly cooled through conduction and radiation. This technique has been used previously to cut and shear metallic glass ribbons,[10] rapidly anneal ferromagnetic metallic glass ribbons,[11] and to weld rods (in what can be considered the precursor to the present work)[12,13]. Spot welding of metallic glass sheets has been demonstrated as a feasible way of forming a joint with up to 70% of the yield strength of the parent material without any detectible crystallization.[14] Recently, Johnson et al. have demonstrated that high imposed current densities and ohmic dissipation can be used for uniform volumetric heating of BMG samples to temperature ranges where they can be processed through injection casting.[15] This was accomplished by discharging energy from a capacitor bank into a cylindrical rod of a BMG and then injecting the softened glass into a mold using the upper electrode as a plunger. In contrast, the present work focuses on welding structures by passing a large current density through the junction between two BMG parts, where the upper electrode provides a sufficiently high compression load to join the heated interface. Because the load required for joining is far lower that the load required for injection molding, complex electrode geometries can be developed which allow for "projection" welding of BMG parts (see Figure 3-1(b-c) for an example). In the current work, this technique is demonstrated to not only form a union with strength approaching that of the parent material, but also to form complex cellular structures that do not preferentially fail at the joints.

To demonstrate the strength of the weld created with this technique, the BMG composite DH1 ($Zr_{36.6}Ti_{31.4}Nb_{7}Cu_{5.9}Be_{19.1}$) was selected. This alloy comprises a highly processable glassy matrix[16] and approximately 40% volume fraction of soft, body centered cubic crystals embedded homogeneously throughout. The alloy was suction cast into stepped plates

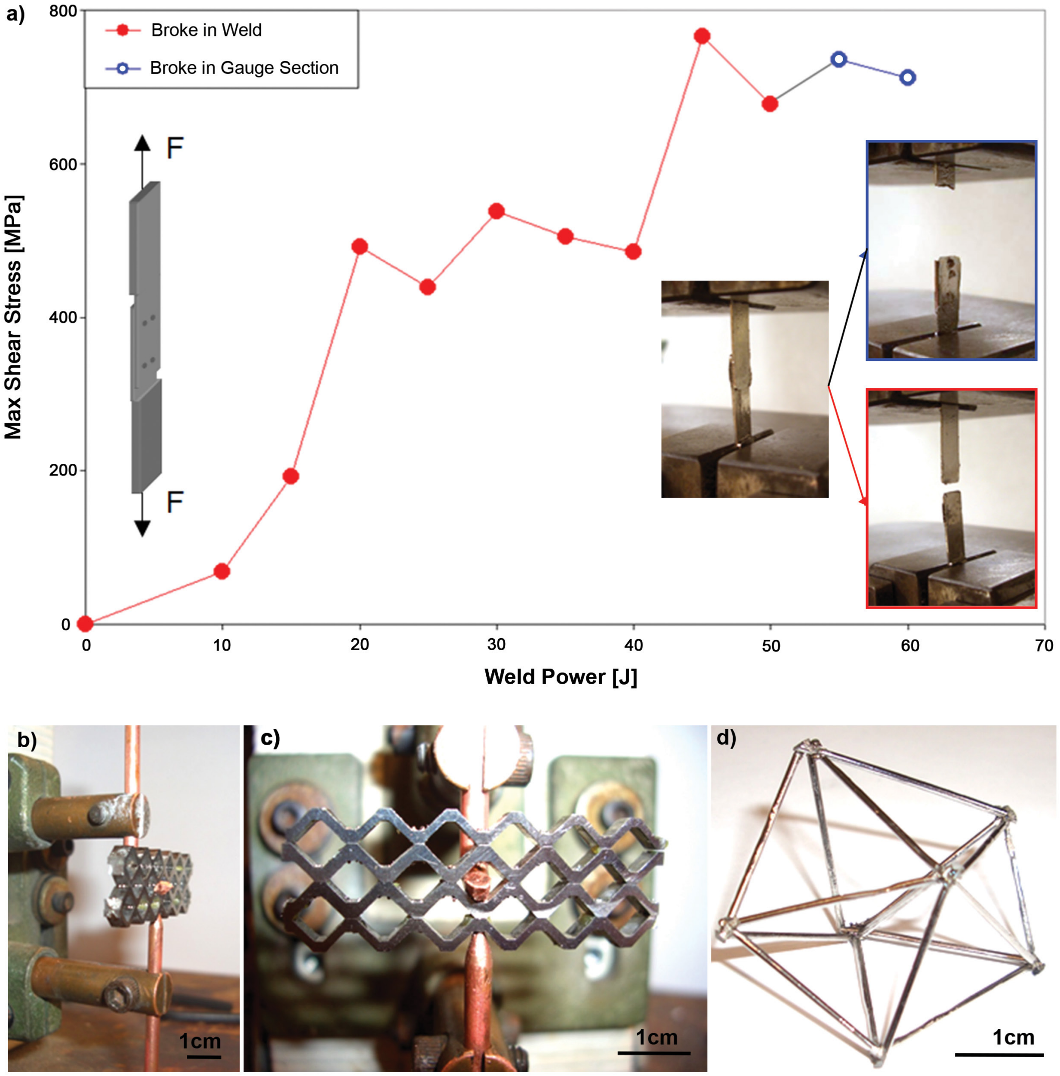

Figure 3-1: (a) Maximum shear stress versus welding power for plates of the BMGMC DH1 that were subjected to four welds for each power. The schematic shows that the geometry of the plates was designed so that the tension test applies pure shear to the welded regions. The red solid circles represent failure in the welds while the filled blue circles represent failure outside the welded region. (b-c) Examples of how copper electrodes can be bent to do "projection welding." In this case, a square honeycomb of the BMGMC DH1 is welded together from corrugated strips. (d) A truss welded fabricated by welding together 1 mm diameter rods of the BMGMC DH1 at the nodes.

(5x30 mm) with a thickness of 1mm on one side, and a thickness of 0.5mm on the other. Two plates were overlapped and welded such that the total thickness of the welded part was 1 mm throughout. This geometry was selected so that a uniaxial tension test could be used to approach a condition of pure shear in the welded region (inset of Figure 3-1a). To join the plates, two copper electrodes were polished to have a 1 mm diameter flat tip. The plates were spot welded using energies ranging from 10 to 70 J per discharge from the capacitor bank. Four welds were used to join each set of plates (leading to a total welded area of ~13 mm^2); the samples were then pulled in tension at a strain rate of 0.1 mm/min until failure. Figure 3-1a shows a plot of capacitor discharge energy versus shear stress at failure. A clear trend of increasing maximum shear stress with increasing weld power was observed until a stress plateau was reached at approximately 500 MPa. At weld energies above 40 J, there appears a jump in the shear stress at failure, leading to a second plateau around 700 MPa, which is approximately the lower bound on the maximum yield strength of the parent material, DH1. The amount of flow and lack of weld line at these discharge energies indicates that a temperature above the solidus was reached (970 K for DH1); however, since the size and morphology of the dendrites appear unaltered at all welding powers, the dwell time or the elevated temperature were insufficient to melt the dendrites (Figure 3-2). With weld energies greater than 50 J, the strength of the welds matches or exceeds the tensile strength of the 0.5x3 mm cross-section of the parent material, and failure occurs in the gauge section instead of along the welds. SEM and XRD inspection of the fracture surface shows no indication of crystallization. At high welding power, the observed shear strength of the welded samples is approximately the same as the yield strength of the plate (τ_y = 700 MPa), demonstrating the ability to form a welded joint with the same mechanical strength as the parent material. It should be noted that these experiments were replicated using a comparable monolithic BMG, and the results showed a similar trend (data not shown).

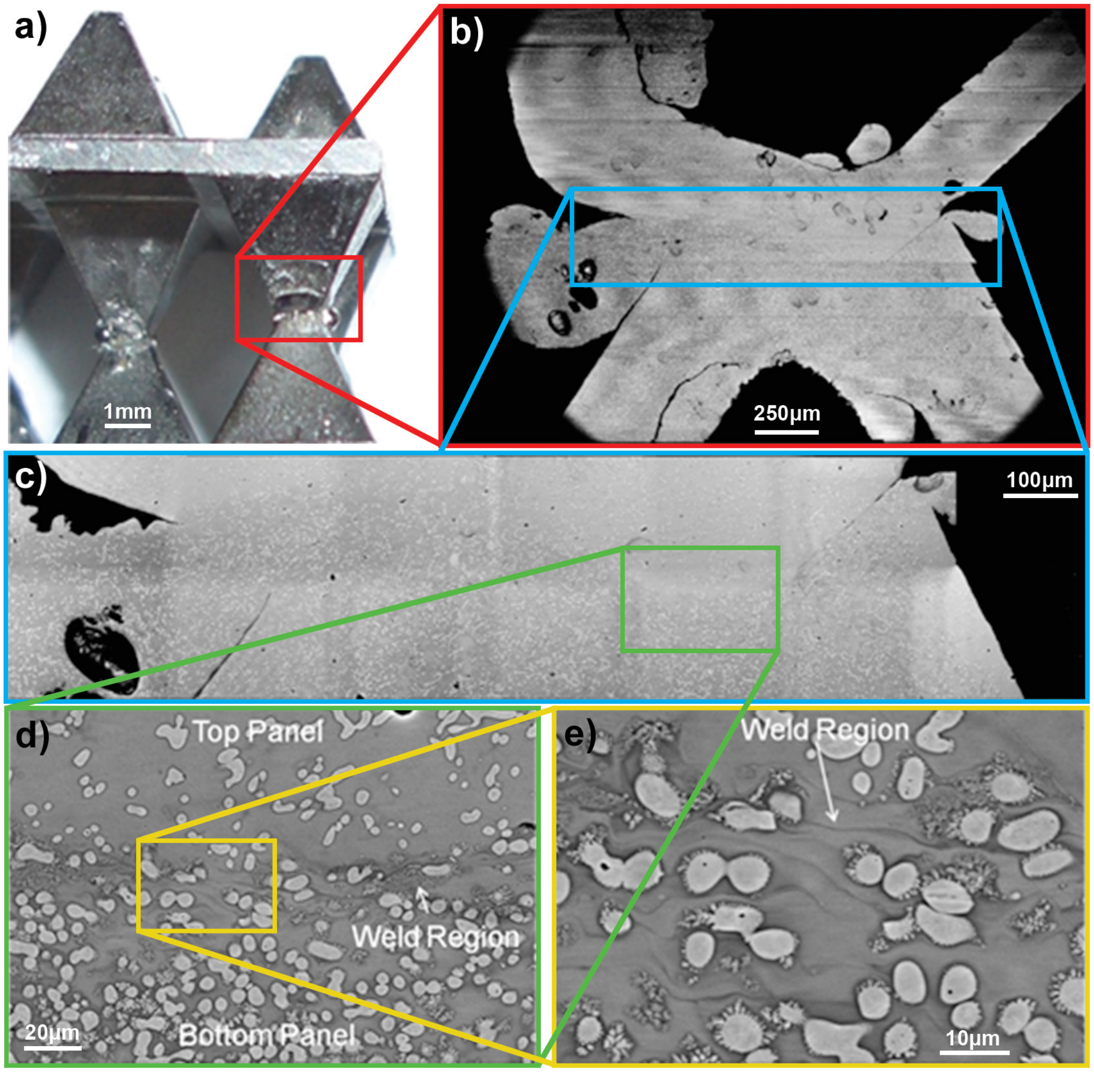

Figure 3-2: (a) An optical image of the nodes between two welded DH1 egg-boxes showing the extent of flow during the welding. (b-e) Progressively enlarged SEM micrographs showing the microstructure of the welded regions. The low magnification micrograph in (b) shows the that material has flowed from under the welding electrodes. At higher magnification (c) there is a clear seam between the two welded pieces that disappears in the location under the electrodes, indicating a solid weld. (d-e) Enlargements of the weld region showing flow lines from the joining but also showing dendrites that were unaffected by the flowing glass matrix. The weld is comprised on the glass matrix from each sample having been heated and joined under the compressive loads without the dendrites being affected. The dendrite microstructures in (d-e) are nominal for the sample outside the welded region.

The key advantage of the capacitive welding technique is the ability to assemble and join BMG composite cellular structures into geometries that cannot be fabricated using other techniques (due to blind machining features, for example). To demonstrate this, panels of semi-solidly forged BMG composite egg-boxes were stacked and welded into cellular structures, and then loaded in compression. The egg-box geometry, which was developed by Schramm et al.[17] for BMG composites, is an elegant way of fabricating a cellular structure that has nearly isotropic deformation in the x-y plane and can be made easily using interlocking molds. Panels with wall thicknesses of 0.5-0.8 mm were produced by semisolid forging,[3] and were demonstrated to have among the highest energy absorbing capacity of any cellular structure.[17] Moreover, the geometry of the egg-box allows for stacking, since the 1 mm square top of each pyramidal cell is designed to align with the bottom of the adjacent cell. Samples were sectioned into 3x3 cells, and the tip of each pyramid was polished. The samples were then stacked, clamped, and the joints were welded together. Two sets of 3x3x2 structures were fabricated at weld energies of 20 J and 40 J. A representative welded sample was cross-sectioned, polished, and imaged using an SEM in QBSD mode to observe the character of the weld (Figure 3-2). As expected, the welding process did not provide sufficient heating or dwell time to allow for the dendrites to go into solution. The dendrite morphology and volume fraction inside the welded region was identical in appearance to the parent material, which was formed through semi-solid forging. Not only was there a continuous path of BMG matrix through the HAZ, but significant flow from both sides of the weld was observed. This indicates that heat generated by the discharge was sufficient to lower the viscosity of the sample, allowing for flow, while the compressive force from the electrode was sufficiently large to induce mechanical mixing between the two sides of the junction. Despite the significant amount of overflow, the dendrites

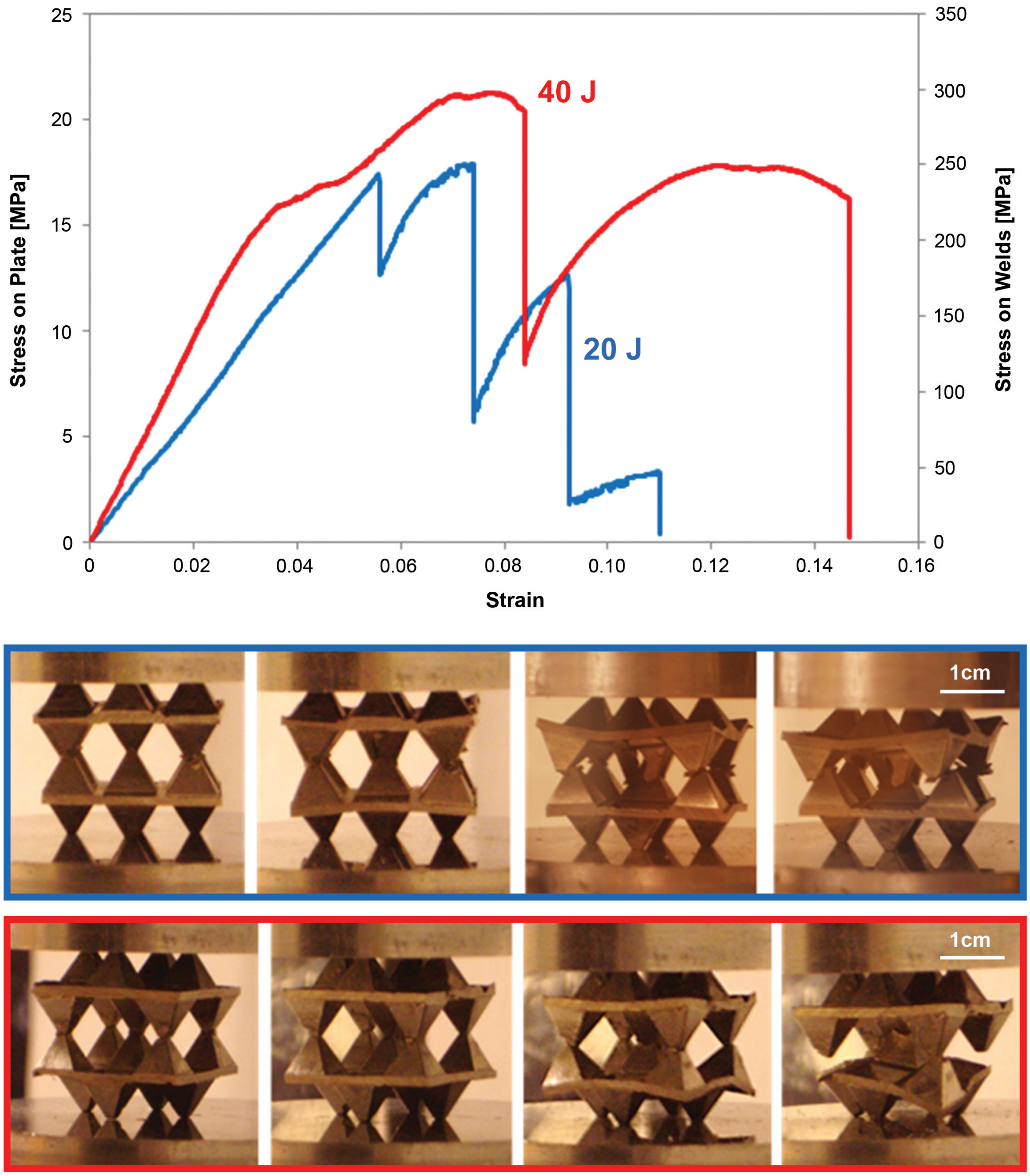

Figure 3-3: Quasistatic compression testing of two DH1 egg-boxes that were welded together at five locations. The blue curve represents a welding power of 20 J (pictured on top) while the red curve represents 40 J (pictured on bottom). Under compression, the samples experience a mixed-mode buckling from edge effects which ultimately breaks the weld. At 40 J, there is a significant amount of buckling before the weld fails, indicating a higher quality weld. This is verified by the compression data, which shows a higher energy absorption in the 40 J welded samples.

were merely displaced by the process and did not have time to change morphology. Moreover, a combination of thermal radiation into the air, conduction into the sample, and conduction into the copper electrodes provided a sufficient cooling rate to prevent the welded junction from crystallizing. This demonstrates that a continuous joint between two pieces of a BMG composite can be created; resulting in a single, uniform structure unobtainable by conventional casting techniques.

By utilizing this projection welding technique, nxn cellular structures can be fabricated from panels of tough, energy absorbing BMG composites. The strength of the welded junction and the energy absorbing capacity of the two-layer, 3x3, welded egg-boxes were assessed using quasi-static compression tests (Figure 3-3). Two samples, welded at 20 J and 40 J, were loaded until failure. The sample welded using 40 J of energy withstood substantially higher loads, and absorbed more energy than the structure welded at lower power. Both samples failed at the welded junctions, primarily due to torque from edge-effects in the samples (Figure 3-3(d-e)).

One potential application of the current technology is the welding of multiple layers of egg-boxes into a thick cellular structure (i.e. an ordered foam). However, with the addition of a third layer, a direct line-of-sight from the welded junction to the electrodes is lost. This can be solved by utilizing a projection welding configuration where the copper electrodes can be bent into complex shapes and inserted into the space between each layer (Figure 3-1(b-c)). Large, truss-like structures were also fabricated out of thin rods using this technique (Figure 3-1d).

The rapid heating and cooling obtained through the use of capacitive welding techniques represent a paradigm shift in the way that BMGs and BMG composites can be integrated into parts. Unlike conventional welding, where the HAZ contains material that is fundamentally different in microstructure and mechanical properties from the parent material, capacitive welding allows for joining BMGs without altering the microstructure. This enables the manufacture of complex parts that could not otherwise be fabricated using any conventional technique. Furthermore, the joints created with this technique exhibit the strength of the parent material, resulting in a structure that behaves as though it was made from a monolithic material. In the next chapter, we show that welding together cellular structures from BMGMCs results in excellent ballistic performance as orbital debris shields for spacecraft.

Citations

[1] D.C. Hofmann, J.-Y. Suh, A. Wiest, M.-L. Lind, M.D. Demetriou, and W.L. Johnson, Proc. Natl. Acad. Sci. U. S. A. **105**, 20136 (2008).

[2] M. Demetriou, C. Veazey, J. Harmon, J. Schramm, and W. Johnson, Phys. Rev. Lett. **101**, 145702 (2008).

[3] D.C. Hofmann, H. Kozachkov, H.E. Khalifa, J.P. Schramm, M.D. Demetriou, K.S. Vecchio, and W.L. Johnson, JOM **61**, 11 (2009).

[4] M. Davidson, S. Roberts, G. Castro, R.P. Dillon, A. Kunz, H. Kozachkov, M.D. Demetriou, W.L. Johnson, S. Nutt, and D.C. Hofmann, Adv. Eng. Mater. n/a (2012).

[5] H.-S. Shin, J.-S. Park, and Y. Yokoyama, J. Alloys Compd. **504**, S275 (2010).

[6] Y. Kawamura, Mater. Sci. Eng. A **375-377**, 112 (2004).

[7] Y. Kawamura, T. Shoji, and Y. Ohno, J. Non. Cryst. Solids **317**, 152 (2003).

[8] H.S. Wang, H.G. Chen, J.S.C. Jang, and M.S. Chiou, Mater. Sci. Eng. A **528**, 338 (2010).

[9] D.C. Hofmann and K.S. Vecchio, Mater. Sci. Eng. A **402**, 234 (2005).

[10] D.E. Ballard, P.G. Frischmann, and A.I. Taub, U.S. Patent No. 5005456 (9 April 1991).

[11] M. Vázquez, J. González, and A. Hernando, J. Magn. Magn. Mater. **53**, 323 (1986).

[12] Y. Kawamura and Y. Ohno, Scr. Mater. **45**, 127 (2001).

[13] a. R. Yavari, M.F. de Oliveira, C.S. Kiminami, a. Inoue, and W.J. Botta F, Mater. Sci. Eng. A **375-377**, 227 (2004).

[14] K. Fujiwara, S. Fukumoto, Y. Yokoyama, M. Nishijima, and A. Yamamoto, Mater. Sci. Eng. A **498**, 302 (2008).

[15] W.L. Johnson, G. Kaltenboeck, M.D. Demetriou, J.P. Schramm, X. Liu, K. Samwer, C.P. Kim, and D.C. Hofmann, Science **332**, 828 (2011).

[16] G. Duan, A. Wiest, M.L. Lind, J. Li, W.-K. Rhim, and W.L. Johnson, Adv. Mater. **19**, 4272 (2007).

[17] J.P. Schramm, D.C. Hofmann, M.D. Demetriou, and W.L. Johnson, Appl. Phys. Lett. **97**, 241910 (2010).

Chapter 4 – Metallic Glasses as Shielding for Hypervelocity Impacts

As human activity has increased in low-earth orbit, so has the accumulation of space debris and the corresponding hazard to space vehicles.[1–3] From 1960 to 1996, the number of objects in orbit increased linearly at a rate of approximately 250 objects per year.[2] Since 1996, however, the number of objects in orbit has been increasing exponentially due to a combination of low-cost space technology and a large number of nations launching spacecraft and satellites. The primary hazard to space vehicles from micrometeoroid and orbital debris (MMOD), comprising fragmentation debris, spacecraft, rocket bodies, and operation debris, is the kinetic energy of these masses traveling at hyper velocities (5-15 km/s).[1–6]

Large debris, generally considered to be objects larger than 100 mm in diameter, can be tracked and characterized by ground-based radar for attitude, size, shape, orbital lifetime, ballistic coefficient, and mass.[2] An impact with large debris is catastrophic for most space vehicles, and collision avoidance maneuvers have been used in the past by the Space Shuttle, satellites, and the International Space Station to prevent such an occurrence.[3] Conversely, small debris projectiles, too small to detect and avoid, have already caused damage to operational space systems.[2] To mitigate the risk of loss of function or mission failure from small debris collisions, particularly from 1 to 5 mm diameter particles, spacecraft designers incorporate implicit protection into vehicle architecture, and explicit MMOD shield impact protection concepts.[5]

A range of shield concepts, including single metal sheets, complex layers of metal, carbon composites, fabrics, and honeycomb sandwich panels (HSPs), have been studied and implemented into space vehicles to mitigate the risk of MMOD impacts.[3–7] The most common type of shield, developed by Fred Whipple in the 1940s, consists of multiple layers separated by a gap, called a standoff (Figure 4-1). The front face sheet of the shield is called the "bumper" and the rear face sheet is called the "rear wall." The bumper breaks up the impacting particle into a spray of melt and vapor that expands while moving though the standoff. Dispersion of the debris cloud over a wider area of the rear wall helps prevent perforation or detached spall. Successful operation of the shield requires that the rear wall survive the impact. The performance of MMOD shields is often estimated using computer simulations and hydrocodes (a computer program used to model the fluid flow of a system) developed from ballistic limit equations (BLEs) obtained via hypervelocity testing.[5–13] For a given shield configuration, test variables include projectile size, velocity, density, and impact angle. The data obtained from a hypervelocity test program are then used to statistically predict the performance of a shield and establish design parameters. For example, the minimum thickness (t_{Ti}, cm) of a titanium wall to prevent a given amount of damage is given by the empirical BLE: [57]

$$t_{Ti} = 5.24d \cdot K \cdot BHN^{-0.25} \left(\frac{\rho_p}{\rho_t} \right)^{\frac{1}{2}} \left(\frac{V \cos\theta}{C_t} \right)^{\frac{2}{3}} \tag{1}$$

where d is the projectile diameter (cm), K the damage parameter for titanium (1.8 for perforation, 2.4 for detached spall, or 3 for incipient attached spall), BHN the Brinell hardness of the target, ρ_p the density of the projectile and ρ_t the density of the target (g/cm^3), C_t the speed of sound in the target (km/s), V the projectile velocity (km/s), and θ is the impact angle from target normal. Thus, a single wall of Ti-15-3-3-3 must be at least 2 mm thick to prevent detached spall from the impact of a 0.8 mm aluminum projectile impacting normal to the plate at a velocity of 6.4 km/s. Equation (1) for titanium shields demonstrates that the material properties which have the most effect on ballistic performance are the hardness and density of the shield (and to a lesser extent, the speed of sound in the target). Subsequently, by increasing the hardness and density of the shield material, the minimum thickness of the shield to prevent a given amount of damage decreases. The density, diameter, and velocity of the projectile also dramatically affect damage, but these parameters cannot be controlled during a real MMOD impact event. Lastly, the impact angle of the projectile affects the ballistic performance of a shield. A normal impact is expected to cause the most damage, while a glancing (oblique) impact does the least damage. Although the trajectory of the projectile cannot be controlled, the design of the shield's surface morphology can affect the impact angle.

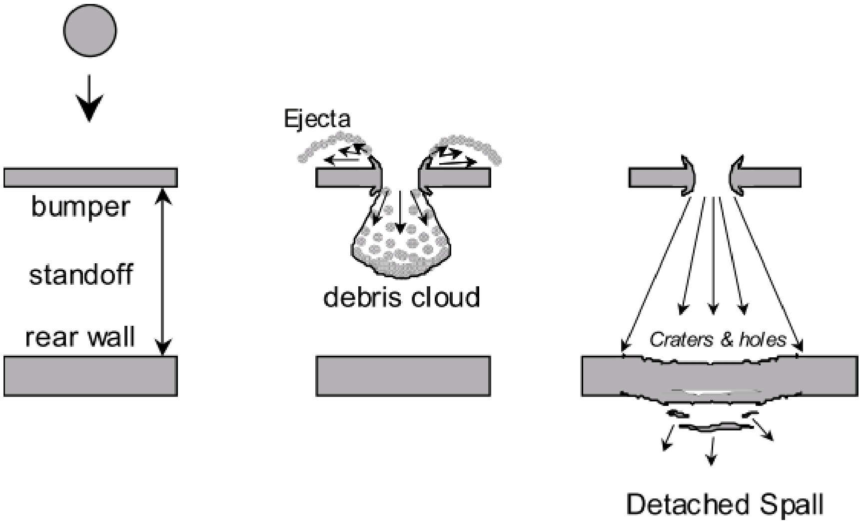

Figure 4-1: A schematic of a Whipple shield with a front bumper, empty space, and a rear wall to catch debris. (b) Impacts will create a cloud of debris both forwards and backwards. (c) If the debris cloud is not sufficiently diffuse it can result in either further penetration or detached spall from the rear wall. Image from Reference [5].

Although BLEs are empirical for each material (Table 4-1), trends in the performance of aluminum, titanium, and steel shields are useful for designing shields from new materials. For example, an optimal bumper shielding material, which combines performance with overall cost, is one that has an extremely high hardness and density, with a multi-faceted face sheet that turns a normal impact into an oblique one, while an optimal foam shield would have a cellular structure that diffuses the impact angle, disperses the debris cloud, and minimizes the shield system of mass. While high hardness would imply that a ceramic shield would be optimal, their high melting temperatures prevent vaporization during MMOD impacts. Solid matter passing through the outer shield, as opposed to liquid and vapor, threatens the spacecraft wall. A truly optimal bumper material combines high hardness and low density with low-melting temperature. This way an MMOD impact vaporizes both the projectile and shield. If the shield is not vaporized it can contribute to the debris cloud impacting the rear wall.

Table 4-1: Ballistic limit equations for various materials

Material	Thickness to prevent damage
Titanium Alloys	$t_{Ti} = 5.24d \cdot K \cdot BHN^{-0.25}\left(\frac{\rho_p}{\rho_t}\right)^{\frac{1}{2}}\left(\frac{V\cos\theta}{C_t}\right)^{\frac{2}{3}}$
Steel	$t_{Steel} \geq 0.781d^{19/18}\left(\frac{\rho_p}{\rho_p}\right)^{1/2}\left(V\cos\theta\right)^{2/3}$
Aluminum Alloys	$t_{Al} = 15.72d^{19/18}BHN^{-0.25}\left(\frac{\rho_p}{\rho_t}\right)^{2/3}\left(\frac{V\cos\theta}{C_t}\right)^{2/3}$

d = projectile diameter (cm); P_x = penetration depth in semi-infinite target of material x (cm); ρ_{p} = projectile density (g/cm^3); ρ_t = target density (g/cm^3); $t_{Material}$ = thickness of steel target (cm); θ = impact angle from target normal; θ = 0° impact normal to target; V = projectile velocity (km/s), BHN is the Brinell Hardness number, C_t = speed of sound in target

Using these shield design criteria, bulk metallic glasses (BMG) and BMG-based matrix-composites (BMGMC) are strong candidates for bumper shielding. BMGMCs are ideal due to their similar density to titanium alloys (5.1-5.8 g/cm^3 vs. 4.5-4.5 g/cm^3, respectively), but they have more than twice the hardness (600 BNH vs. 250 BNH, respectively). They are also designed around deep eutectics to provide a low melting temperature (~900 K) which allows for greater ease of vitrification.[14] The low-solidus temperature and high viscosities of BMGMCs also enable unique panel fabrication methods. As shown in the previous chapter, semi-solid forging techniques have been developed previously to fabricate thin (<0.8 mm wall thickness) panels of BMGMCs in an "eggbox" configuration.[15] These panels exhibit superior specific energy absorption values for cellular structures due to advantageous combinations of high strength, high ductility, and low relative density. These structures also present a multi-faceted surface to an incoming projectile, ensuring that the impact angle is always near 45°. These combinations of features are investigated in the current chapter.

Thin panels of BMGMCs were subjected to hypervelocity impacts at the NASA Ames Vertical Gun Range using a two-stage light gas gun capable of firing a variety of projectiles from a sabot at velocities from 0.8 to 5.5 km/s (Figure 4-2a). BMGMCs plates were fabricated by semi-solid forging.[16] The alloy was heated by induction to a temperature between the solidus and liquidus (~1225 K), held isothermally to allow the microstructure to coarsen, and then forged using water cooled copper molds (Figure 4-2b and 4-2d). DH1 ($Zr_{36.6}Ti_{31.4}Nb_{7}Cu_{5.9}Be_{19.1}$) BMGMC[17] was used in the forging of thin plates (0.5-1.0 mm thick) from 10 g ingots, Figure 4-2c, and thin eggbox panels (0.6 mm nominal wall thickness) from 25 g ingots (Figure 4-2e). The nominal microstructure from each alloy is shown in the inset of Figure 4-2e. The lighter contrast material is the coarsened dendrites and the darker material is the metallic glass matrix. The panels were fastened to a testing jig, Figure 4-2f, and impacted at a normal angle, with velocities ranging from 0.8 to 3.0 km/s, using 3.17 mm aluminum spheres packed in a sabot. The charges were ignited using gunpowder and the sabot was stripped off immediately after the sphere left the gun barrel. The velocity was measured using time-of-flight between sensors and the impact was captured using three laser-triggered cameras. Three cameras recorded each impact: a backlit one using 500,000 frames per second, another using 1,000,000 frames, while a third was

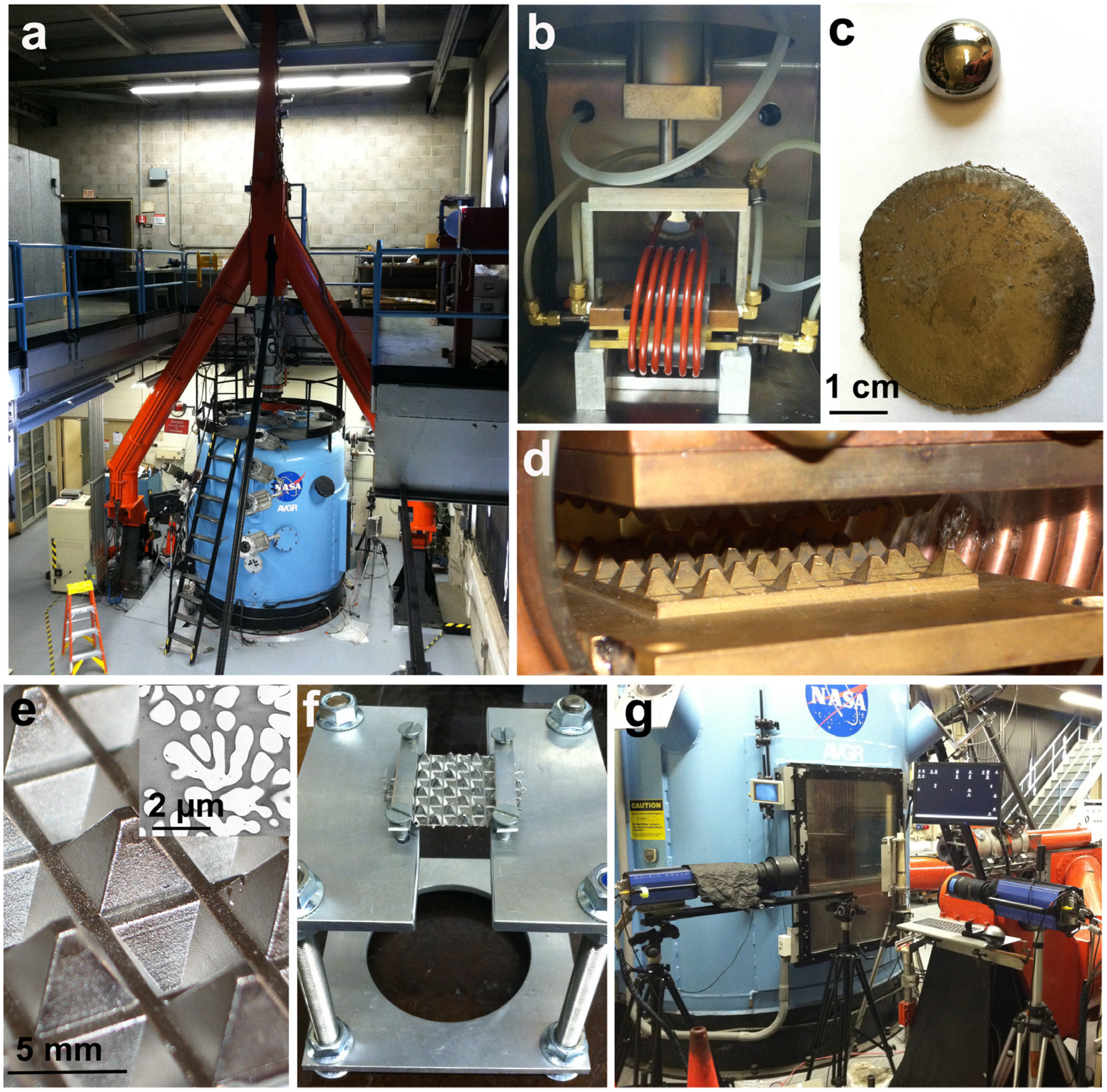

Figure 4-2: Hypervelocity facility and test samples – (a) View of the NASA Ames Vertical Gun Range, which consists of a two-stage light gas gun capable of firing projectiles in two different configurations to allow simulations of impacts from 0.8 to 5.5 km/s. The environmental test chamber is over 2 m high and the angle of impact can be changed using multiple ports on the side. (b) Forging chamber used to fabricate thin plates and eggbox structures. (c) Example of a 10 g ingot of the BMGMC DH1 ($Zr_{36.6}Ti_{31.4}Nb_7Cu_{5.9}Be_{19.1}$) forged into a 0.8 mm thick sheet. (d) Mold used to forge eggbox panels from BMGMCs. (e) BMGMC eggbox with a 0.6 mm thick wall semisolidly forged and the nominal microstructure shown in the inset. (f) Eggbox panel fixed to testing jig. The hole in the bottom plate allows for the collection of debris from the impact. During some impacts, a witness plate was used instead to assess damage. (g) Setup of the high-speed cameras used to capture the impact. Three cameras can be seen in the image (one is at the upper right).

left with an open shutter to collect all the light emitted from the event. The setup is shown in Figure 4-2g.

Figure 4-3 shows two hypervelocity impacts from 3.17 mm spherical aluminum projectiles flying at 2.3 km/s to contrast the performance of a BMGMC shield in different geometries (a thin plate and a multi-faceted eggbox). Six images captured in sequence during impact testing of the eggbox structure are exhibited in Figure 4-3a. The view is edge-on and backlit. The clamping screws are visible at the top and bottom of the sample. The impact occurred on a 45° angled surface of the eggbox, and the event took ~102 µs from the initial impact to the dissipation of the energy releasing flash. Similar impact conditions were used for a thin plate of the same BMG composite with approximately the same thickness, but in a flat configuration instead of the multi-faced one, and results are exhibited in Figure 4-3b. In comparison to the eggbox geometry, the flat plate has a much shorter energy-release flash and the debris cloud is much less diffuse as it travels down range. An estimation of the energy dissipated as light was obtained by counting the white pixels in each frame of video and plotting it versus the frame number (Figure 4-3c). The eggbox geometry produced a light intensity over four times greater than the flat plate as seen when analyzing the non-backlit camera (which is set up to capture only light intensity). Moreover, the eggbox effectively diffused the debris cloud after the impact. Image analysis of at least 95% of the debris cloud was used to estimate the dispersion angle (Figure 4-3d and 4-3e). The dispersion angle of the debris cloud was increased substantially by faceting the surface, from 76° to 101° for flat and faceted surfaces, respectively. Figure 4-3f and 4-3g show a time lapse image of the entire impact taken from a camera above the samples, where all of the light generated in the image is from the impact (the red light is an LED that backlights the samples and pulses at the same frequency as the high speed camera,

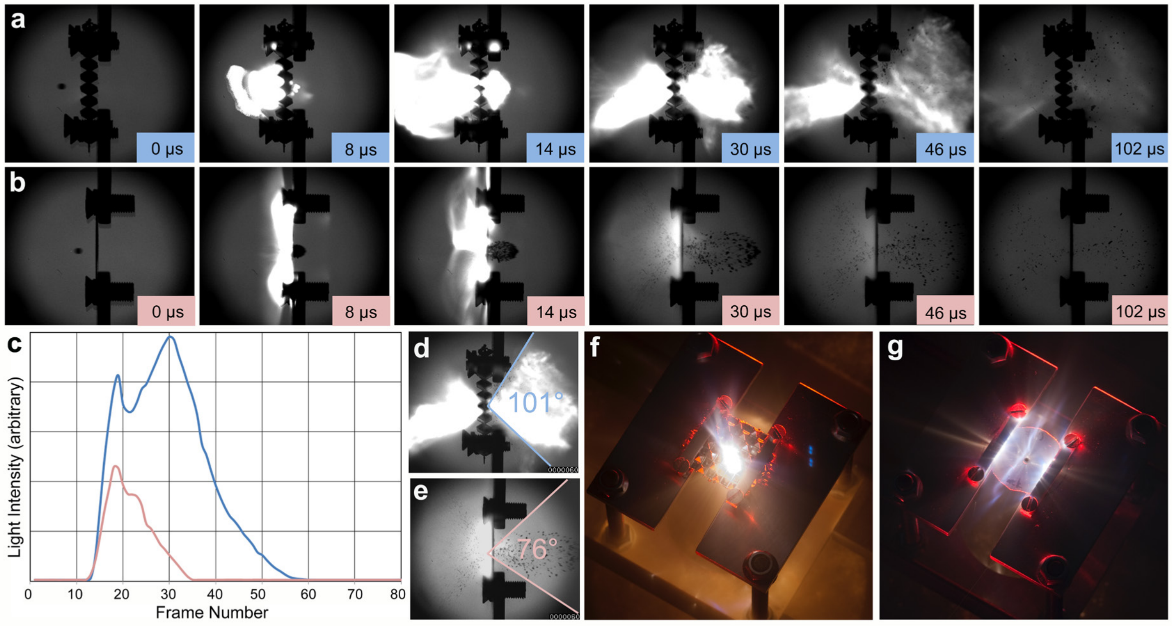

Figure 4-3: Comparison of surface geometry during hypervelocity impacts in BMG composite panels. (a) Backlit side-view images from a 3.17 mm aluminum sphere impacting a 0.6 mm thick DH1 eggbox, shown in (c), at 2.7 km/s for the first 102 µs after impact. The multi-faceted surface effectively diffuses the impact into a broad debris cloud. (b) The same velocity impact as (a) into a 0.7 mm thick BMGMC composite sheet. The impact conditions and alloy are the same between (a) and (b) but the surface geometry is different. In (b) the debris cloud is tightly clustered after impact. (c) Plot of light intensity versus frame number for the hypervelocity tests in (a,b). As an estimation of energy released during impact, image analysis was used to determine the length and intensity of the light. The eggbox is much more effective than the thin sheet at dissipating energy. (d,e) Image analysis was used to designate a range of angle of the debris cloud that captures at least 95% of the debris. The eggbox geometry (d) has a 25° wider spread than the thin sheet (e). (f,g) Long exposure images from the impacts in the eggbox (f) and the thin sheet (g) illustrating the difference in light intensity during the impact. The red light is the laser used to trigger the high-speed camera.

500 KHz). The single wall impact demonstrates the advantages of the thin, multi-faceted eggbox geometry to diffuse debris from the initial impact.

Cellular geometries have previously been employed for MMOD shielding. Specifically, aluminum honeycomb sandwich panels (HSPs) have been used widely as spacecraft shielding due to their low-areal density and ability to diffuse MMOD impacts because of the cellular geometry. HSPs are generally brazed to aluminum facesheets to form the shield, and their performance in hypervelocity tests is well established.[3,6,8,9] These shields exhibit drawbacks, however, including low hardness of the aluminum facesheets, a channeling effect during impacts caused by the honeycomb geometry that prevents dispersion of the debris cloud, low intrinsic strength, and difficulties with brazing. A more effective metal cellular shield can be created by using a harder and higher strength metal and making the geometry stochastic (e.g., using random bubbles instead of tubular honeycombs). The challenge, however, is that these types of cellular structures are difficult to fabricate from conventional high strength metal alloys, such as titanium and steel, due to the higher processing temperatures required to form them. Earlier in this thesis it was shown that bulk metallic glass matrix composites can be welded together via capacitive discharge. Figure 4-4a-d illustrates this method. A welded 6x6x3 cellular structure is shown in Figure 4-4e. It is fixed into the testing jig in Figure 4-4i. For comparison, an aluminum HSP with its upper face sheet removed is provided in Figure 4-4f. In the HSP, impact debris is able to pass through the honeycomb structure easily, an effect called "channeling." In the BMG composite egg-box structure, debris must perforate each multi-faceted layer of the egg-box to penetrate the structure.

Hypervelocity testing was performed on the three-layer BMG composite egg-boxes by firing a 3.17 mm aluminum sphere at 2.3 km s^{-1}, as shown in Figure 4-4g. The projectile impacted an angled surface at 45°, similar to the single layer test, and the debris diffused between the first and second layer. The debris moved laterally in the fifth frame, and then dissipated out the top and bottom, and only a small region of detached spall reached the third layer. The welded

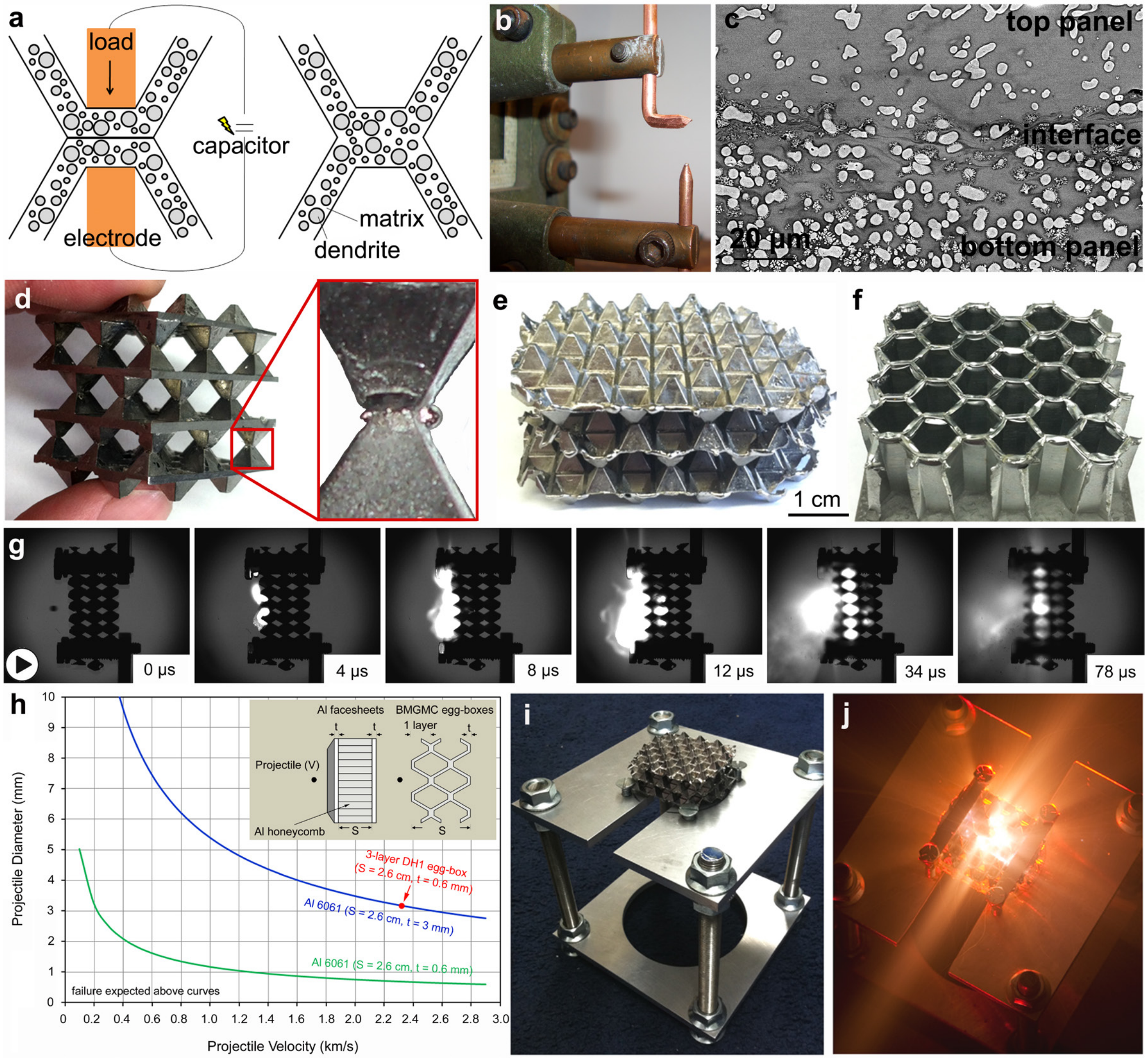

Figure 4-4: Hypervelocity impact of a welded BMG composite cellular structure. (a) Schematic of the capacitive joining process for a BMG composite. (b) Shaped electrons on a spot welder were used to weld egg-boxes together. (c) SEM micrograph from two egg-box panels welded together. (d-e) Egg-box panels which have been welded together. (f) Aluminum HSP structure. (g) Backlit side view of the three layer egg-box structure being impacted by a 3.17 mm aluminum projectile at 2.3 km s^{-1} showing penetration of the first layer and slight penetration of the second layer. (h) Plot showing projectile diameter versus projectile velocity for aluminum sandwich panels with aluminum facesheets calculated from ballistic limit software. S is the height of the honeycombs and t is the thickness of the face sheets. (i) The layered egg-box structure loaded into the sample holder. (j) A long exposure image showing the light generated during the hypervelocity impact.

joints remained intact throughout the impact, and the kinetic energy of the projectile was mitigated. Figure 4-4h shows a plot of BLEs for aluminum HSPs provided by NASA's Johnson Space Center. The lower green curve represents aluminum HSP with the same overall thickness as the three layered BMG structure (26 mm), and with face sheets equal in thickness to the wall of the BMG structure (0.6 mm). The performance of the three layered BMG composite structure falls on the BLE for an aluminum HSP with thickness of 26 mm, but with much thicker face sheets (3 mm vs. 0.5 mm in the composite). Because the third layer of the BMG composite cellular structure was not perforated, the BLE for this structure lies above the upper blue curve in Figure 4-4e. A long exposure image of the entire impact is shown in Figure 4-4j.

This chapter involved a preliminary assessment of BMG composites as potential spacecraft shielding against the threat of MMOD. Utilizing known parameters obtained from hypervelocity testing of conventional materials, BMG composite shield concepts were designed to exploit the critical material and geometric properties (mainly hardness, density, and impact angle) and tested using hypervelocity impacts. We demonstrated that welded panels of BMG composites offer a unique shielding solution for future satellites and spacecraft that are increasingly exposed to the threat of MMOD collisions. This work was also a collaboration with Professor Steve Nutt and Marc Davidson of USC, who assisted in the analysis of the debris cloud.

References

(1) Debris, O.; Committee, T. A.; Debris, S.; Isbn, C.; Pdf, T.; Press, N. A.; Academy, N. *Orbital Debris: A Technical Assessment*; National Academy Press: Washington, DC, 1995; p. 224.

(2) Space, S. and T. S. of the U. N. C. on the P. U. of O. *Technical Report on Space Debris*; United Nations: New York, 1999.

(3) Christiansen, E. L.; Nagy, K.; Lear, D. M.; Prior, T. G. Space station MMOD shielding. *Acta Astronaut.* **2009**, *65*, 921–929.

(4) Schonberg, W. P. Protecting Earth-orbiting spacecraft against micro-meteoroid/orbital debris impact damage using composite structural systems and materials: An overview. *Adv. Sp. Res.* **2010**, *45*, 709–720.

(5) Christiansen, E. L. *Handbook for Designing MMOD Protection*; National Aeronatuics and Space Administration Johnson Space Center: Houston, TX, 2009; p. 152.

(6) Destefanis, R.; Schäfer, F.; Lambert, M.; Faraud, M. Selecting enhanced space debris shields for manned spacecraft. *Int. J. Impact Eng.* **2006**, *33*, 219–230.

(7) Ryan, S.; Christiansen, E. L. *Micrometeoroid and Orbital Debris (MMOD) Shield Ballistic Limit Analysis Program*; TM-2009th–21st ed.; National Aeronautics and Space Administration Johnson Space Center: Houston, TX, 2010.

(8) Sibeaud, J.-M.; Thamié, L.; Puillet, C. Hypervelocity impact on honeycomb target structures: Experiments and modeling. *Int. J. Impact Eng.* **2008**, *35*, 1799–1807.

(9) Schonberg, W.; Schafer, F.; Putzar, R. Hypervelocity impact response of honeycomb sandwich panels. *Acta Astronaut.* **2010**, *66*, 455–466.

(10) Grujicic, M.; Pandurangan, B.; Zhao, C. L.; Biggers, S. B.; Morgan, D. R. Hypervelocity impact resistance of reinforced carbon–carbon/carbon–foam thermal protection systems. *Appl. Surf. Sci.* **2006**, *252*, 5035–5050.

(11) Yang, C.; Liu, R. P.; Zhan, Z. J.; Sun, L. L.; Wang, W. K. High speed impact on Zr41Ti14Cu12.5Ni10Be22.5 bulk metallic glass. *Mater. Sci. Eng. A* **2006**, *426*, 298–304.

(12) Hayhurst, C. J.; Livingstone, I. H. G.; Clegg, R. A.; Destefanis, R.; Faraud, M. Ballistic limit evaluation of advanced shielding using numerical simulations. *Int. J. Impact Eng.* **2001**, *26*, 309–320.

(13) Yang, C.; Wang, W. K.; Liu, R. P.; Liu, L.; Zhang, X. Y.; Li, L. X. Impacted by Hypervelocity Projectiles. *J. Spacecr. Rockets* **2006**, *43*, 12–14.

(14) Johnson, W. L. Bulk glass-forming metallic alloys: science and technology. *MRS Bull.* **1999**, *24*, 42–56.

(15) Schramm, J. P.; Hofmann, D. C.; Demetriou, M. D.; Johnson, W. L. Metallic-glass-matrix composite structures with benchmark mechanical performance. *Appl. Phys. Lett.* **2010**, *97*, 241910.

(16) Hofmann, D. C.; Kozachkov, H.; Khalifa, H. E.; Schramm, J. P.; Demetriou, M. D.; Vecchio, K. S.; Johnson, W. L. Semi-solid induction forging of metallic glass matrix composites. *JOM* **2009**, *61*, 11–17.

(17) Hofmann, D. C.; Suh, J.-Y.; Wiest, A.; Duan, G.; Lind, M.-L.; Demetriou, M. D.; Johnson, W. L. Designing metallic glass matrix composites with high toughness and tensile ductility. *Nature* **2008**, *451*, 1085–9.

Chapter 5 – Wear Behavior of Metallic Glass Gears

Introduction

Metallic glasses have a range of advantageous properties which are well known in the literature. They are considered to be high strength, tough,[1,2] good in corrosion,[3,4] and highly processable[5] to name a few. This chapter will focus on another oft-cited property of metallic glasses: wear resistance. Wear and friction have been the focus of study since the 1970s.[6] In the interim, many systems have been studied many different ways. To help aid with the uniformity of study, the American Society for Testing and Materials (ASTM) has created standards by which wear tests should be performed.[7] These standards, as described below, will be adhered to as closely as possible in this study.

Many previous studies have been performed on metallic glasses in wear, but a main issue is the variety of different ways it can be measured. ASTM offers more than twenty different standards and methods by which wear, and wear-related properties, can be measured in metals. Figure 5-1 outlines some of the most frequent methods used to study wear. The most common test is pin-on-disk, where a pin (either a cylinder or ball) is held stationary while the disc is rotated. This test can be performed in the geometry shown, with the pin being pushed up from the bottom, or with the apparatus rotated to the side. Depending on how the test is oriented, wear debris can collect on the sample differently, causing differing amounts of wear at extended periods of time. Some studies also use the sample under study to be the pin, and others the disc. The second test is shown in (c), a reciprocating pin on plate. This geometry was used for many of the early MetGlas experiments from the literature. A pin (typically a stainless steel alloy) is held stationary while the ribbon is reciprocated underneath it. The geometry has

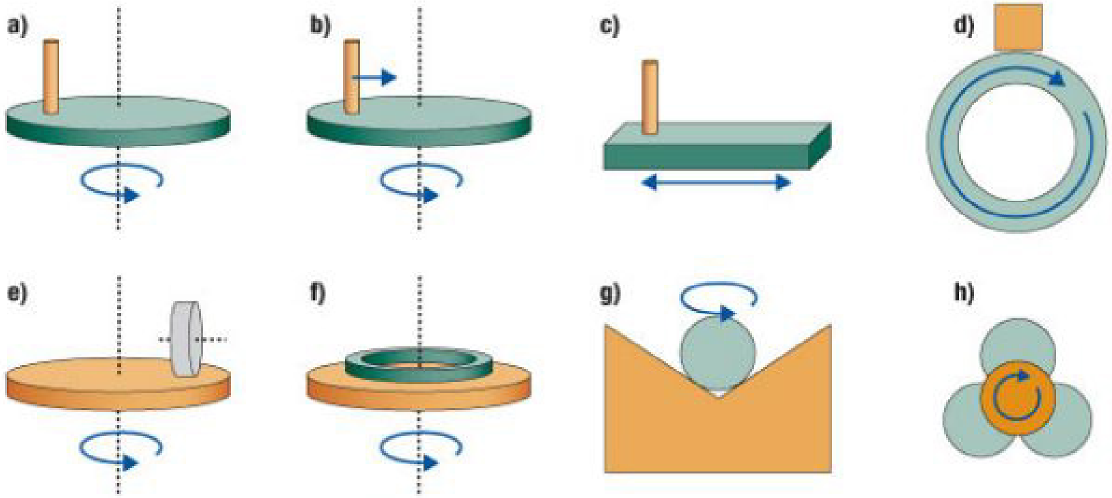

Figure 5-1: Common wear test geometries: (a) pin-on-disc with circular track (b) pin-on-disc with spiral track (c) pin-on-plate (d) block-on-ring (e) disc-on-wheel (f) thrust washer (g) ball-on-prism (h) four ball. Pin-on-disc and pin-on-plate may be identified as ball-on-disc or ball-on-plate, respectively, if the pin has a hemispherical tip.[8]

also been used for rods of metallic glass being rubbed against a steel plate. (d) is another technique used for cylinders of metallic glass where they can be worn against a rotating ring.

The wide variability in testing procedures has made it hard to do direct comparisons from one study to another.

It has been well established that wear rate is related to loading conditions. Numerous studies have found a direct proportionality of wear rate to the applied load. It has been seen in Fe, Ni, and Co-based amorphous ribbons,[9] as cast, crystallized, and annealed Vitreloy 1,[10] as well as in Cu-based bulk metallic glasses.[11] Palar et al[12] have performed extensive studies on the relationship between load and sliding speed on both wear and coefficient of friction (μ). They found an inverse relationship between μ and the normal force. It was also found that as sliding speed was increased, μ stayed roughly constant except for the slowest speeds, where it slightly increased. Finally, they found as the normal load was increased the wear rate decreased. Conflicting reports on velocity by others have also been published. Tao et al[13] state there is a decrease in mass loss per rotation with increased velocity, but an increase coefficient of friction. On the other hand, Li et al[10] state that by increasing the sliding velocity there is an increase in wear rate for as cast, crystallized, and annealed Vitreloy 1. Wear rate has also been shown to directly relate to the sliding distance for Cu-based BMGs.[11]

Most tests tend to be performed on the lower end of the force and sliding velocity spectrum. A reason for this is, as a wear test is performed, heat is generated. If the sliding velocity was high enough, the material wouldn't have enough time to diffuse heat away from the wear track, and temperatures could rise to the glass transition range (or higher). Likewise, for higher pressures, more work is being done at the point of contact, so more heat should be generated. Therefore, at high pressures and sliding speeds, the most heat will be generated, and a breakdown to the linear nature of sliding velocity and load can be expected. At this point, crystallization or displacement of material through flow instead of plasticity can be expected. In order to probe this region, a few experiments have been performed. Huang et al found a decrease in wear resistance along with hardness as temperature increased in a Fe-based BMG.[14] Liu et al performed wear tests near the glass transition temperature in Vitreloy 1. They found near T_g both μ and wear was reduced. As temperatures went higher, friction was reduced more as well. Yet another study found conflicting results, with the μ increasing at higher temperatures.[12]

Yet another possibility for influencing wear in metallic glasses is through various heat treatments. When a metallic glass is quenched, its properties are strongly dependent upon its enthalpy. A rapidly quenched glass will have different properties than one cooled just barely fast enough to form a glass. By annealing at a given temperature, a well-defined position in the potential energy landscape can be reached; so many groups have tested both annealed and crystallized states. Segu et al crystallized a Fe-based BMG and found the crystalline form had much worse wear than the amorphous.[15] Tam and Shek partially crystallized 3 mm pins of $Cu_{60}Zr_{30}Ti_{10}$ and found 30% crystallinity improved wear resistance over as cast samples, and both outperformed a sample which was 50% crystalline.[16] Maddala and Hebert annealed $Cu_{50}Hf_{41.5}Al_{8.5}$ for a variety of times at a temperature high enough to slow grow nanocrystals. They found that as annealing time increased, toughness decreased while hardness increased. Associated with the increase in hardness was a decrease in the wear rate, up until full crystallization, at which point the hardness still increased, but the wear rate increased dramatically.[17] Another study found that for Vitreloy 1, a relaxed glass performed the best, followed by the as cast, and then crystallized.[10] Similarly, another study of a different Zr-based glass found a minimum in wear rate at 40% crystallinity, and claimed to have seen crystallization occurring in the wear track.[18] Chen et al had the creative idea of using a laser to melt a thin surface layer and create a gradient from fully crystalline to fully amorphous, and then performing wear testing on each of the interfaces. It was found that the layer which consisted of an amorphous matrix with crystalline dendrites performed the best (as opposed to the layer with an amorphous matrix and nanocrystallites which performed poorly).[19] Finally, Liu et al tested thermally sprayed $Fe_{62}Ni_3Cr_4Mo_2W_2Si_6B_{17}C_3$. They found that once crystallized its wear performance was the best, followed by the as sprayed condition, and it was the worst when partially crystallized.[20] In the $Ni_{59}Ti_{16}Zr_{20}Si_2Sn_3$ system, however, when kinetically sprayed it outperformed both the partially crystalline and fully crystalline forms when fully amorphous.[21]

Metallic glasses have also been tested under a variety of different environmental conditions. In a comparison between wear in dry conditions, deionized water, and hydrogen peroxide, Vitreloy 1 was found to resist wear best in dry conditions, followed by 60%-90% H_2O_2, then DI H_2O, then 30% H_2O_2.[22] At least three studies have been performed on zirconium based glasses in inert atmospheres. The first found wear was significantly worse under oxygen than argon.[23] The second found the same conclusions as the first, and also performed testing under an argon atmosphere, where it performed similar to under vacuum. It was also found that the surface likely formed a zirconium oxide, which readily flaked off and resulted in high wear rates.[24] A follow-up study included an oxygen environment where wear was accelerated even further than air.[23]

A few other studies have been published which are also pertinent for the current chapter. Microgears (2.4 mm in diameter) have been fabricated out of a Ni-based alloy, and outperformed the currently used steel in a rolling wear test.[25] Another group made composites by including small Fe BMG particles into a crystalline Ni matrix. They noticed that as more BMG was added, μ decreased, but it led to a more brittle wear path.[26]

There are also a number of hypotheses in the literature about various material properties which should be discussed. *The CRC Handbook of Lubrication & Technology* makes the assertion that toughness is the main determinant of wear resistance.[27] This view is tempered in *Introduction to Tribology*; which qualifies the above idea by stating that fracture toughness generally only affects the wear rate in extremely hard and brittle materials. It also states that wear rate can decrease with an increase in the modulus of elasticity for materials with primarily elastic contacts.[28] Opinions are split as to whether the wear performance of metallic glasses is proportional to hardness[14,23,26,29] while others do not[15,18]. An inverse relationship between wear resistance and hardness is predicted by the well-known Archard's wear equation. A final proposed correlation is the ratio of the hardness to elastic modulus. Oberle predicted that materials with a low elastic modulus will be able to accommodate the passage of an abrasive through elastic deformation and avoid permanent damage.[30] This supposition has seen renewed popularity in the applications of nanoindentation.[31]

Experimental

While the studies on wear resistance in metallic glasses are vast, this chapter will focus on a very specific set of requirements, with a particular end use in mind. Recently, prior to the launch of the Mars Science Laboratory (MSL), the steel alloy selected for the gearboxes on the Curiosity rover was found to wear at unacceptable rates in a cold environment. At the time, only ceramic gears had been shown to provide wear behavior at acceptable levels; however, they were expensive and unqualified. So, due to time and budget constraints, a quick engineering fix had to be used. Instead of finding a new material to replace the current Vascomax steel gears, a lubricant was added. Unfortunately, the lubricant's viscosity was too high at low temperatures, and therefore the entire gear box required heating. This necessitated adding heater cartridges and temperature sensing instrumentation to each of the gear boxes on MSL. In addition, wiring routes had to be designed and implemented. Now that MSL has landed, the heat cartridges require power, and actually use approximately 30% of the energy produced by the radioisotope thermoelectric generators. If the gears could instead be used at ambient temperatures, all of that excess power could be used toward scientific instruments.

For this reason, a few basic requirements were set for BMG alloys under consideration. The gears would need to have a minimum critical casting thickness of 3 mm in a 25.4 mm diameter circle via suction casting into copper molds. The desired BMG should have a high enough toughness to survive casting, and some minor post-casting processes, such as machining or wire-cut electrical discharge machining (EDM). The goal was to create an alloy with the wear characteristics of a ceramic, but the toughness of steel. It is also desirable to have fully amorphous (or controllably composite) gears allow for consistent properties from the as-cast state. Metastablely processed composites, those which form dendrites that are not in thermodynamic equilibrium in the semi-solid regime, are not acceptable, as their properties are highly dependent upon both sample geometry and cooling rates. Likewise, nanocrystalline alloys will not be considered in this chapter, as their grain size (and thus properties) can be heavily reliant upon their processing history, in addition to their typically low toughness.

This initial screening stage narrows the available BMG families down to zirconium, titanium, and copper based alloys. Iron, magnesium, lanthanum, nickel, and all other families are either too brittle or will not form glasses in the geometry being tested.

Cylinder-on-Disk Testing

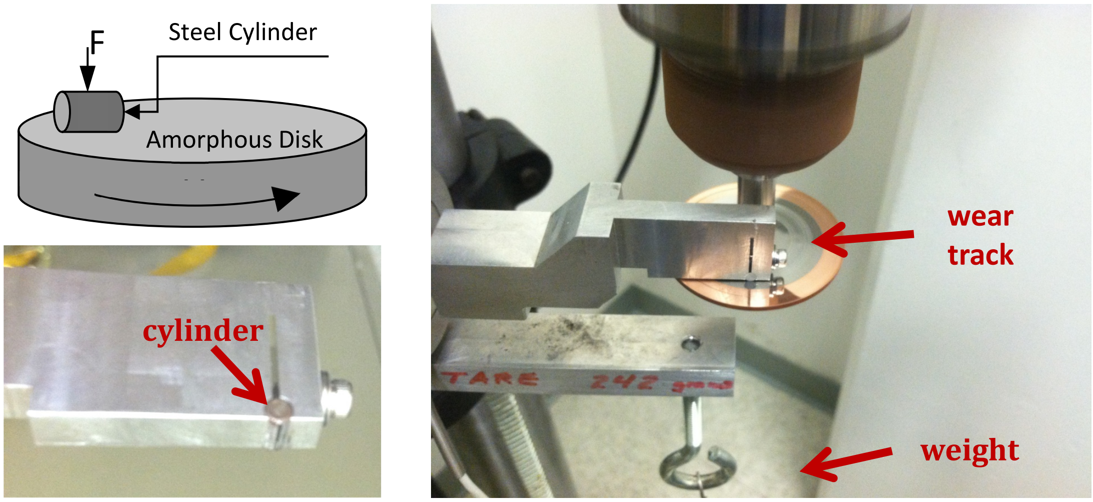

Figure 5-2: a) A schematic for a cylinder-on-disk test. b) Highlighting the mounting system for the cylinder and demonstrating the line contact. c) A cylinder-on-disk test in progress.

Initial testing was done with a cylinder-on-disk test. A schematic of the test is shown in Figure 5-2. In this test, a steel cylinder is pushed onto a disk of the material to be tested. The disk is then rotated with frequency ω for a given distance. The constant force is applied by weight hanging through a pulley system. This test was initially used as a quick screening method for a variety of metallic glass alloys. Table 5-1 summarizes the cylinder-on-disk findings. Mass loss is defined as the change in mass of the test sample as measured before and after the wear test. Nitronic 60 is a fully austenitic steel designed with the intention of being used in high wear conditions. SS 15-5 PH is a precipitation hardened stainless steel commonly used in gears. Ti-6Al-4V STA is a low density titanium alloy which has been solution-treated and aged. It is a common aerospace material. Vascomax C300 is a maraging steel with high hardness and strength. Two amorphous alloys supplied by a commercial source were tested, and compared against ingots created in the laboratory. Then, a number of glass forming alloys were also fabricated via arc melting and suction casting into a copper mold.

Table 5-1: Summary of Pin-on-Disk Results

Alloy Name	*State*	Wear Loss in cylinder-on-disk (mg)
Nitronic 60	Crystalline	6.9
SS 15-5 PH	Crystalline	5.7
Ti-6Al-4V STA	Crystalline	5.2
Vascomax C300	Crystalline	0.5
$Zr_{36.6}Ti_{31.4}Nb_7Cu_{5.9}Be_{19.1}$ (Commercial)	Amorphous	19.1
$Zr_{41.2}Ti_{13.8}Cu_{12.5}Ni_{10}Be_{22.5}$ (Commercial)	Amorphous	16.3
$Zr_{35}Ti_{30}Cu_{8.25}Be_{26.75}$	Amorphous	10
$Zr_{36.6}Ti_{31.4}Nb_7Cu_{5.9}Be_{19.1}$	Composite	7.3
$Zr_{41.2}Ti_{13.8}Cu_{12.5}Ni_{10}Be_{22.5}$	Amorphous	6.4
$Ti_{48}Zr_{20}V_{10}Cu_5Be_{15}$	Composite	5.5
$Zr_{57}Nb_5Cu_{15.4}Ni_{12.6}Al_{10}$	Amorphous	4.1
$Cu_{47.5}Zr_{48}Al_4Co_{0.5}$	Composite	3.5
$Cu_{47}Zr_{46}Al_5Y_2$	Amorphous	2.8
$Cu_{43}Zr_{43}Al_7Be_7$	Amorphous	2.3
$Cu_{43}Zr_{43}Al_7Ag_7$	Amorphous	2
$Cu_{41}Zr_{40}Al_7Be_7Co_5$	Amorphous	0.9
$Ni_{40}Zr_{28.5}Ti_{16.5}Al_{10}Cu_5$	Amorphous	0.2

A large range of mass loss can be seen in both crystalline and amorphous systems. Vascomax, the current material used in gears on the MSL, outperforms its closest conventional competitor by an order of magnitude (0.5 mg material lost compared to 5.2 for Ti-6Al-4V). $Zr_{41.2}Ti_{13.8}Cu_{12.5}Ni_{10}Be_{22.5}$ (Vitreloy 1) performed extremely poorly when taken from commercially cast plates, with a wear loss of 16.3 mg to the 6.4 mg of a laboratory prepared sample. $Zr_{36.6}Ti_{31.4}Nb_7Cu_{5.9}Be_{19.1}$, a BMGMC, also performed considerably worse using commercial stock material, with 19.1 mg to 7.3 mg from a laboratory prepared ingot. This is likely due to the known problem with commercial materials having a higher amount of impurities (excess oxygen, carbon, etc) due to poor processing conditions. Alloys with these impurities are known to have inferior mechanical properties to those produced via more clean methods. The rest of the MG alloys can be seen to span a range of wear behaviors, from $Zr_{35}Ti_{30}Cu_{8.25}Be_{26.75}$ being marginally worse than the crystalline alloys, to $Ni_{40}Zr_{28.5}Ti_{16.5}Al_{10}Cu_5$ only losing 0.2 mg, a 60% improvement on Vascomax.

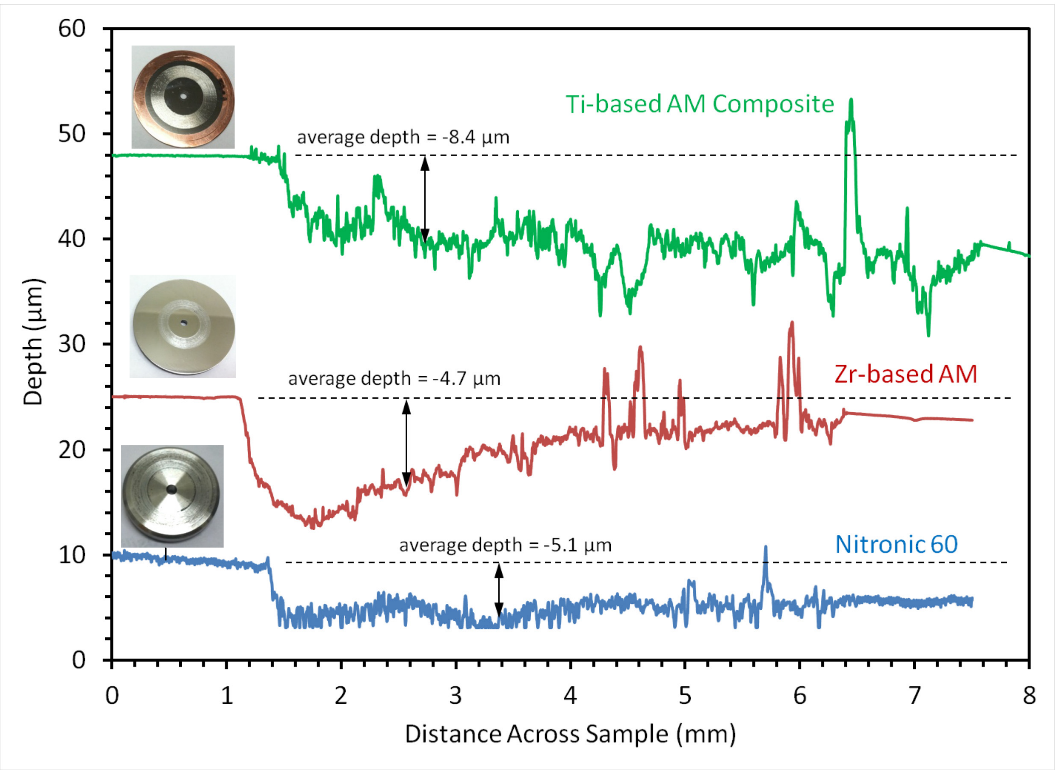

Figure 5-3: Profilometry data for three samples. The Ti-based composite and Zr-based AM were both polished to a 0.02 um finish, while the Nitronic 60 sample was finished on a lathe. Inset are images of each sample post-wear.

As another measure of wear resistance, profilometry measurements were performed on some of the specimens. Figure 5-3 contains a plot of wear depth versus position from a titanium-based composite, Vitreloy 1, and Nitronic 60, an austenitic steel alloy (shown inset). For each sample, an average wear depth (R_m) was calculated. The Ti-based composite fared the worst, with an average wear depth of 8.4 μm. Both Vitreloy 1 and Nitronic 60 had similar wear depths, with 4.7 μm and 5.1 μm, respectively. While Vitreloy 1 had a smaller average depth, the profile was less consistent, with much heavier wear on one side of the track than the other. This likely arose due to an issue with the metal cylinder not being perfectly flat on the sample during the wear test.

Pin-on-Disk Testing

Issues such as the one above with a misaligned cylinder prompted further refinement of our experimental technique. In order to decreases sensitivity to instrumental error and come into compliance with ASTM standards, a pin-on-disk (POD) tester was built and used instead of a cylinder-on-disk tester. Figure 5-4a is a schematic of how a POD tester operates. Similar to a cylinder-on-disk test, the sample is rotated at a frequency ω with a pin placed at some radius, R, away and a normal force, F, applied to it. In this case, however, a point force is applied by a stainless ball bearing instead of a cylinder, which creates a line force. Figure 5-4b and 5-4c show a specimen being tested. The testing conditions were kept consistent for all samples. R was 9.75 mm, the ball bearing was 4.76 mm in diameter, the rotational frequency was Y Hz, and a normal force of 1 N was applied. The samples were run for a total distance of 1.2 km. The frictional force was also measured via a Wheatstone bridge. Samples were individually weighed and alloyed in an arc melter. They were then suction cast into a copper mold 25 mm in diameter and 2.75 mm thick (shown inset in Figure 5-4d). Each then had the gate sections removed. Faces were polished to a 16 μm finish prior to testing.

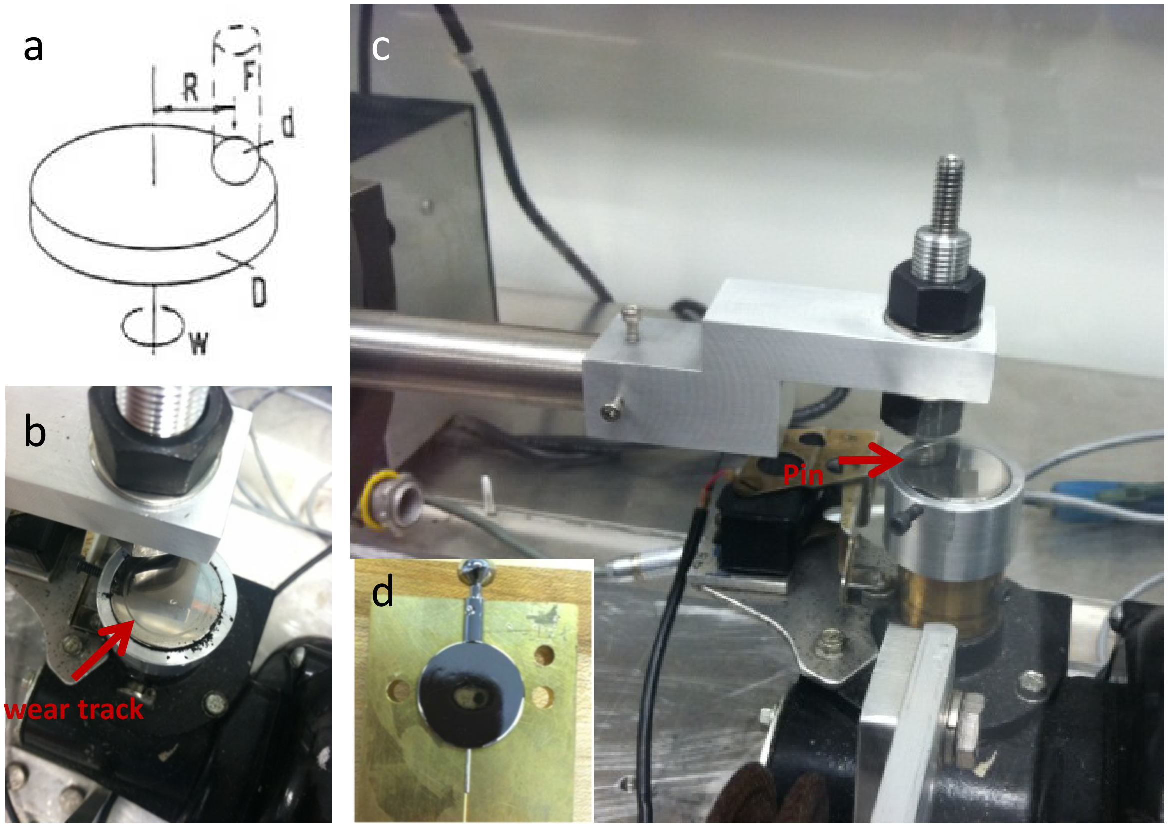

Figure 5-4: a) A schematic diagram of the ASTM standard pin-on-disk test. b) An overhead view of a POD test in progress. Wear debris can be seen on the edges of the sample holder. c) An overview of the POD tester. The pin is located at the end of a long arm to allow for precise application of a normal force. d) An as-cast sample prior to removal of gate material.

For each sample, a number of measurements were performed. The Vickers hardness was measured on a Leco LM247 hardness testing machine. A 2 kg weight was used with a dwell time of ten seconds. At least three hardness measurements were made around the sample to account for local variability. The density was determined via the Archimedes method. By measuring the speed of shear and longitudinal sound waves being propagated through the sample, all of the elastic moduli can be determined through the relations for isotropic materials:[32]

$$c_l = \sqrt{\frac{K + \frac{4}{3}G}{\rho}} \qquad c_s = \sqrt{\frac{G}{\rho}} \tag{1}$$

$$E = \frac{9KG}{3K + G} \tag{2}$$

$$\nu = \frac{1}{2} - \frac{E}{6K} \tag{3}$$

Where c_l and c_s are the longitudinal and shear wave speeds, respectively, ρ is the density, K is the bulk modulus, G is the shear modulus, E is the elastic modulus, and ν is Poisson's ratio. From the frictional force data, both a run-in time (the amount of time for a steady-state force to be reached) and an average frictional force were measured. In order to measure mass loss accurately, each sample was weighed on the same analytical balance with precision to 0.1 mg multiple times, both before and after the test was performed. Each alloy had at least two wear tests performed to try and detect anomalous results. A Mitutoyo Surftest SJ-210 surface roughness tester was used to measure the surface profile across the wear track.

The most important value measured in testing is the mass loss. One has to be careful when interpreting this value, though, since it can be heavily influenced by the density of the material being worn. Suppose identical gears were made out of tungsten (density of 19.3 g/cm^3) and beryllium (1.85 g/cm^3). During a wear test it could be possible that the beryllium gear loses half as much mass as the tungsten gear. One could be tempted to quickly assume the Be gear performed significantly better, since it lost hardly any weight. However, volume-wise it lost almost 21x more material. So, by converting to volume loss, the differences in density between varying alloy systems can be compensated for.

In addition to compensating for the variability in densities between materials, it is desirable to use a quantity which is as independent of testing conditions as possible. In following Greer's derivation,[33] we start with Archard's wear equation[34]

$$V_W = K\frac{SN}{H} \tag{4}$$

Where V_W is the total volume of material removed by wear, S is the sliding distance, N is the normal load, H is the hardness, and K is the dimensionless wear coefficient. In order to be able to compare across multiple experimental conditions (differing loads, wear distances, etc.) the dimensional wear coefficient, *k* is used instead.

$$k = \frac{K}{N} = \frac{V_W}{SN} \tag{5}$$

k has units of Pa^{-1}, but can also be defined as $mm^3/(N^{-}m)$. This then allows us to take a measured wear loss and convert it into a measurement of the volume of material lost per distance per normal load.

$$k = \frac{\Delta m}{SN\rho} \tag{6}$$

From this we now have a measurement which will allow not only comparing across different alloy systems, but across different experimental setups, and allow comparisons in the future for measuring the effect of distance and load on the rate of material removal.

Unfortunately, there has not been a comprehensive study of BMG alloys in wear resistance, and the studies which have been done have generally been done through very different experimental methodologies. For this reason, it was determined the first thing to be performed would be a survey of a number of different systems. Samples would need to be able to be suction cast from an arc melter into a copper mold and remain amorphous in a 25.4 mm diameter by 3 mm thick geometry. Unfortunately, these requirements take out a number of systems containing elements with high vapor pressures. During the arc melting process the constituent elements are heated up in excess of 1750 K, and elements with high vapor pressures can rapidly evolve into vapor, making it difficult to reliably create stoichiometrically accurate alloys. This eliminates, for the most part, all Ni and Fe based alloys. Appendix A gives all of the compositions fabricated, as well as the following quantities measured: state (amorphous, composite, or crystalline), density, Vickers hardness, elastic modulus, bulk modulus, shear modulus, Poisson's ratio, measured wear loss, volume of material lost, average wear track depth, average wear track width, and *k*, the dimensional wear coefficient. Compositions are grouped by alloy family (CuZr, Ni, Ti, and Zr/ZrTi).

One of the attributes typically given to BMGs is their "high wear resistance," but Figure 5-5's representative plots of a few alloys' wear tracks demonstrates how BMGs' performance can span the space of wear loss from being on par with state-of-the-art materials to well over an order of magnitude worse. Vascomax's wear track was barely measurable, as was crystalline $Ni_{56}Zr_{17}Ti_{13}Si_2Sn_3Be_9$. $Cu_{43}Al_{43}Al_7Be_7$ had marginally worse performance, though it was nowhere near as bad as the Zr-based GHDT, which had roughly an average wear track over thirty times deeper than that of crystalline $Ni_{56}Zr_{17}Ti_{13}Si_2Sn_3Be_9$. Unfortunately, even though the Ni based alloy had phenomenal wear performance, it was very brittle. This makes it somewhat limited in usefulness, it was unable to survive being machined in any form, which is a necessity to cut gear teeth or to machine mounting holes. Going back and inspecting Appendix A, it can be seen all of the Ni alloys are either fully crystalline or composites. All of the composites also appear to be the "accidental" type, which makes them fairly uncontrollable in an engineering sense and therefore not suitable to our purpose.

As there were two methods used to measure the amount of wear loss, it is worthwhile inspecting the differences between the two. The first was a direct method, done by measuring the mass of material lost from the wear testing. Each sample was weighed at least six times immediately prior to testing, tested, cleaned of any wear debris with ethanol after completion of the test, dried, and then reweighed at least another six times. This procedure generally left certainty in the measurement of mass at each point to approximately 0.1 mg. The mass lost was then converted to volume loss through the density formula,

$$\Delta V = \frac{\Delta m}{\rho} \tag{7}$$

This allows for direct calculation of volume loss. Another method is by using a profilometer to find the wear profile across the wear track in numerous places (examples are given in Figure 5-5). An average wear depth can then be measured for each profile, and an average overall depth can be found. This introduces some uncertainty due to the need for setting a baseline, variability in the wear track, and precision of the profilometer. However, at small mass losses it does seem to be fairly sensitive, and, as such, could be a useful tool in distinguishing between performance of low wear alloys. The volume of wear loss was determined by using the formula for an extruded annulus:

$$V = \pi R_m \left(r_o^2 - r_i^2\right) \tag{8}$$

Where R_m is the average wear depth, r_o is the outer wear radius, and r_i is the inner wear radius. We also know the following relations:

$$r_o = R + \frac{R_W}{2} \qquad r_i = R - \frac{R_W}{2} \tag{9}$$

Where R is the initial radius of wear and R_W is the total width of the worn track. By substituting in we get:

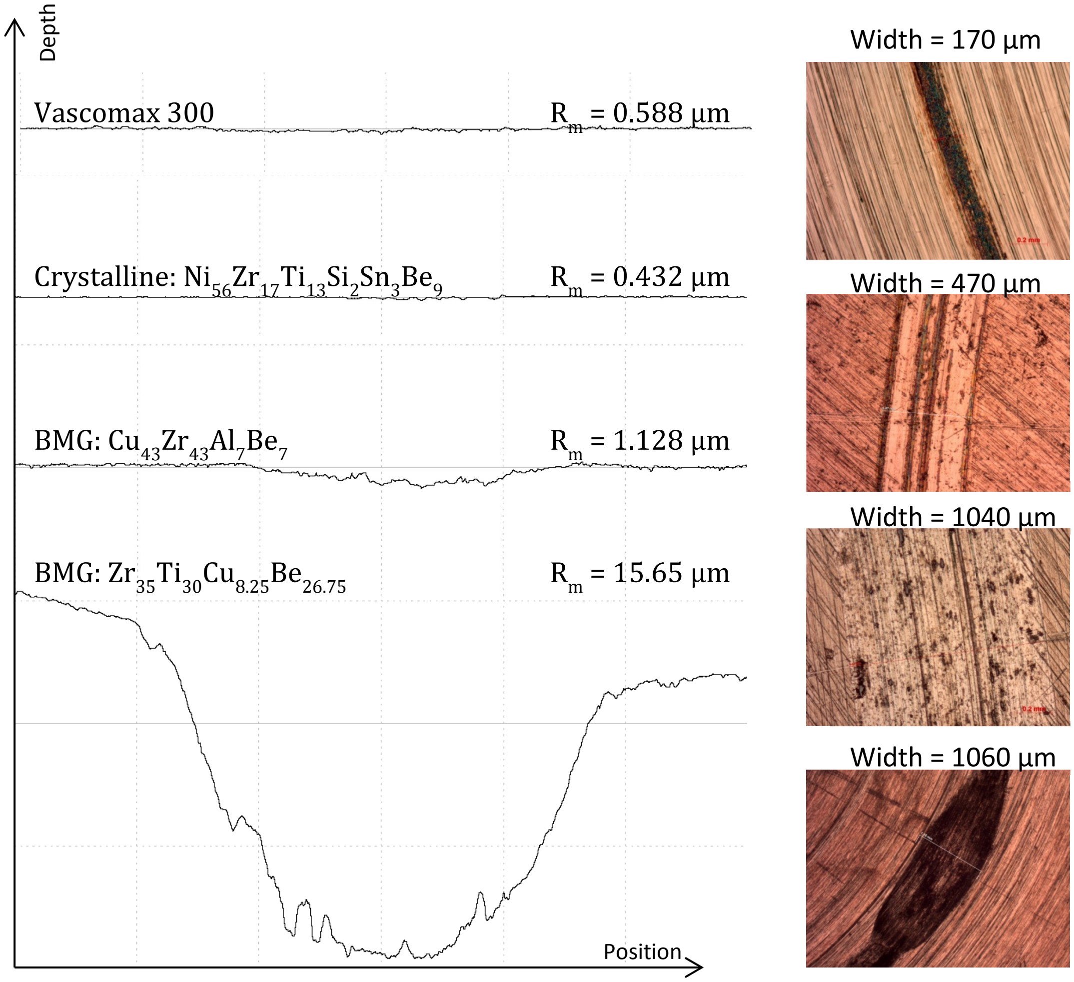

Figure 5-5: A comparison of line profiles between different alloys after a pin-on-disk test. A large difference can be seen between the current gear material, Vascomax, and one of the worst performing BMG alloys tested.

$$V = \pi R_m \left[\left(R + \frac{R_W}{2} \right)^2 - \left(R - \frac{R_W}{2} \right)^2 \right] \tag{10}$$

$$V = \pi R R_W R_m$$

So, by simply measuring an average wear depth, an average width, and knowing our initial wear radius, the volume of material lost can be calculated. Figure 5-6 is a comparison of the two methods for finding volume loss for all alloys tested. Points which fall above the solid line have a higher volume loss calculated through mass loss. While many alloys wind up with similar values for both methods, determining volume loss through profilometry consistently finds lower magnitudes of mass loss. None of the alloy systems in general seem to particularly be well described by both methods at the same time, either. ZrTi has the most spread, Ti is consistently underestimated by profilometry, while it seems to be more precise at the lower amounts of wear loss. As the method of measuring the mass is a more direct method, it will be later be the method used to determine k, the dimensional wear coefficient.

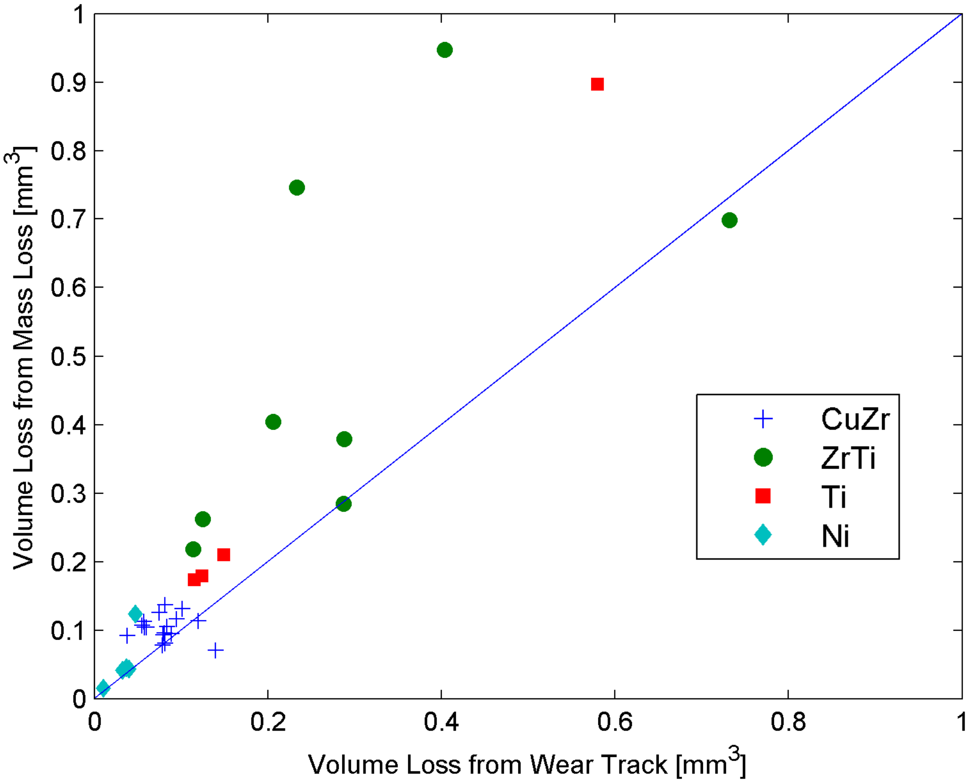

Figure 5-6: Measuring volume loss by profilometry seems to consistently underestimate the amount of wear loss compared to measuring mass changes. Alloys are both amorphous, composites, and crystalline.

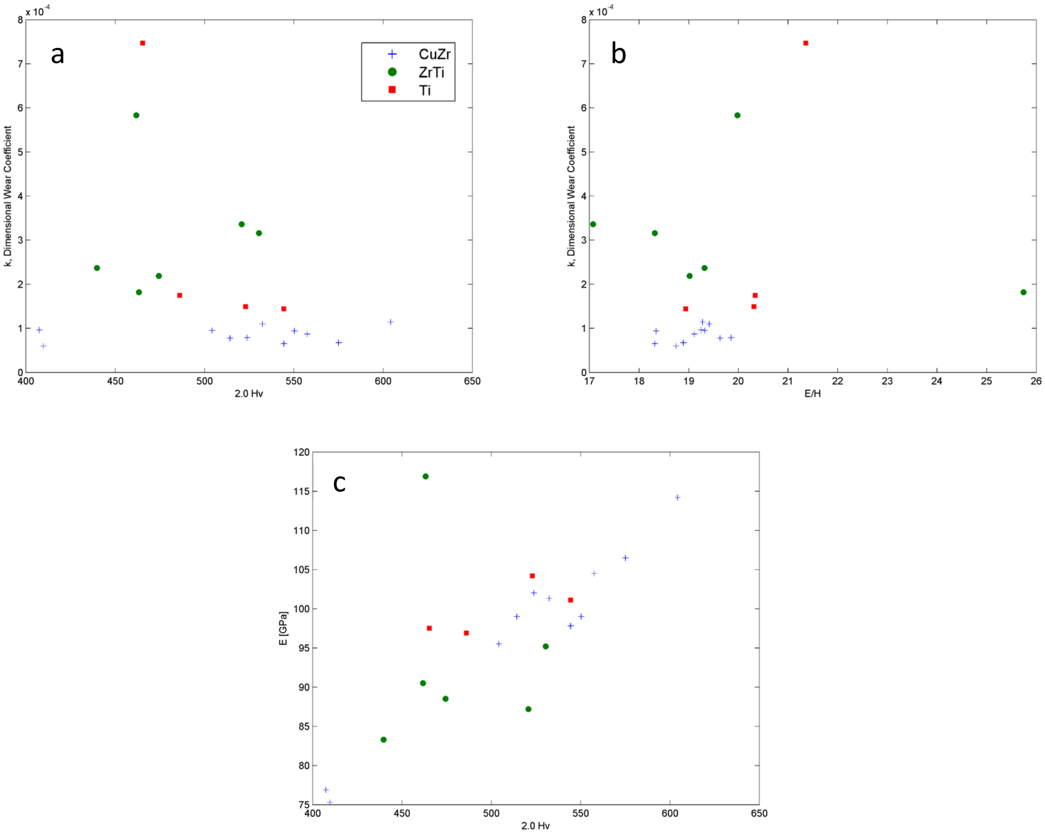

Figure 5-7: a) *k* versus hardness. These are typically considered directly proportional, however for our alloys there seems to be no trend. b) k versus E/H. The quotient of elastic modulus to hardness can be seen as a ratio of elasticity versus resistance to plastic deformation. c) As expected, E is fairly proportional to H_V. All alloys are amorphous.

The most commonly cited criteria for predicting wear resistance is its hardness, due to its presence in the Archard wear equation (4). Figure 5-7a contains plots comparing the Vickers hardness to wear resistance. A couple of trends emerge. First, there seems to be little correspondence between hardness and wear resistance. The softest CuZr alloys wear less than the hardest, and the compositions with moderate hardness have similar wear performance. The Ti-based system has moderate wear performance, although one composition has the worst of any amorphous alloy tested. In general, ZrTi is poor in wear, and has the opposite performance of what is expected: as hardness increases, wear resistance decreases. Figure 5-7b compares *k* to the ratio of the elastic modulus, E, versus hardness. This quantity (E/H) is a ratio of elasticity in a material to resistance to plastic deformation. If one thinks of wear, it can be seen as a series of asperities on each surface impinging on the others. The elasticity measures how much energy it takes to elastically deform them, and the hardness gives an estimate of how much energy it takes to then permanently deform the asperity to a different shape. For this reason, it wouldn’t be surprising if the two are related to wear behavior. Again, though, we see most of the clustering occurring due to alloy system, with no apparent global or systemic relationships.

Figure 5-7c directly compares E to hardness, and there does at least appear to be a relationship between these two. As hardness increases so does the elastic modulus. This does make a bit of intuitive sense, especially in metallic glasses. Elasticity is a macroscopic measure of the stiffness of bonds between neighboring atoms. As these become stiffer, it becomes more difficult to separate them enough to initiate a shear band, the method by which metallic glasses plastically deform. This is why an increased E should lead to an increased hardness.

Another set of properties suspected to have a relationship to wear performance is the elastic constants. Figure 5-8 contains plots of the elastic modulus (E), shear modulus (G), bulk modulus (K), and Poisson’s ratio versus *k*. For E, G, and Poisson’s ratio there is no obvious correlation. Groupings again only appear by alloy system, without any particular trends within systems apparent either. There does appear to be a trend between the K and *k*. As the bulk modulus increases, the wear resistance increases. This is surprising, as in the wear process asperities would be more likely to undergo a shear stress, and thereby be influenced strongly by G instead of K.

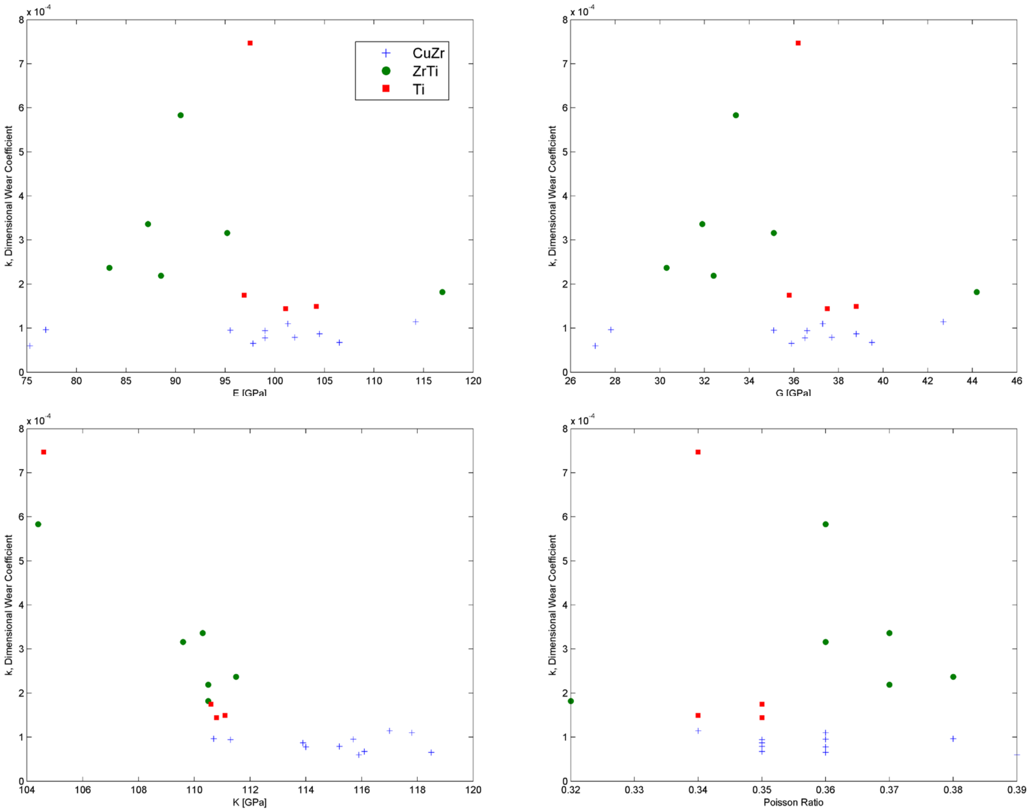

Figure 5-8: *k*, the dimensional wear coefficient versus each of the elastic constants. *k* is in units $mm^3/(N\text{-}m)$.

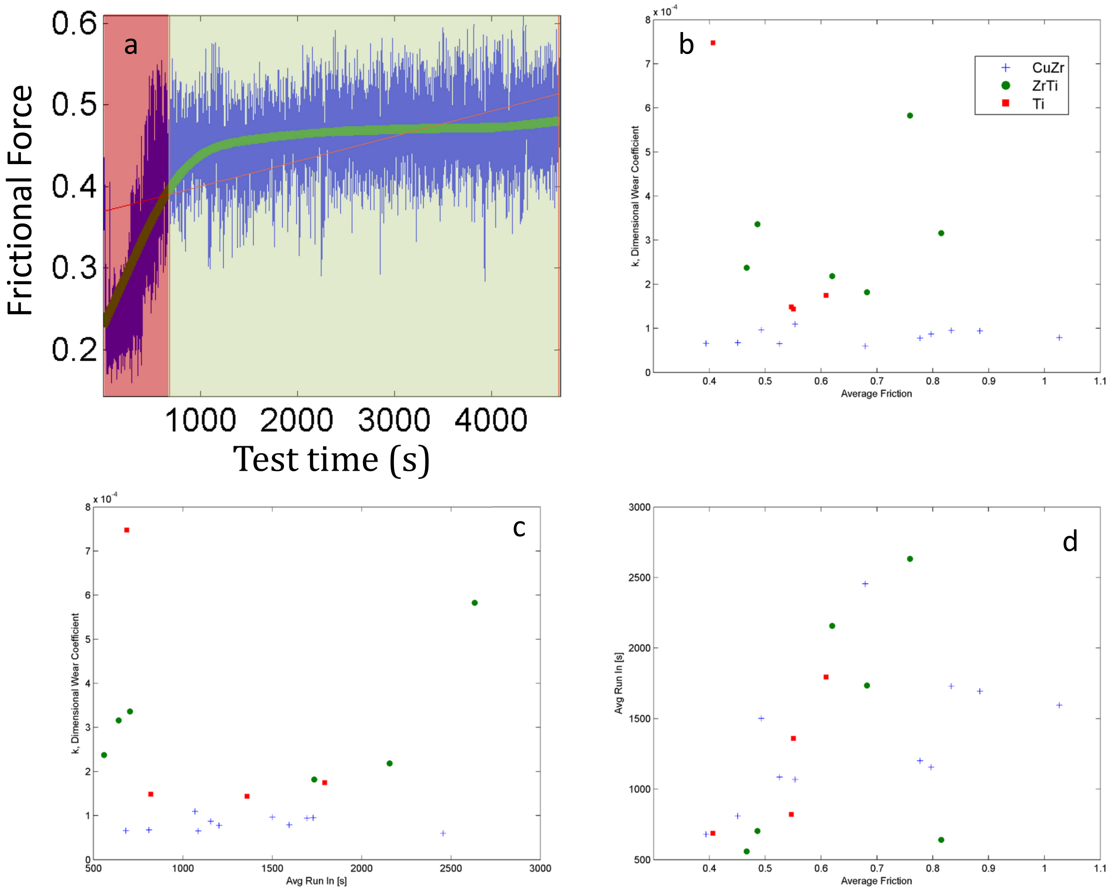

Figure 5-9: a) A typical friction vs time plot from the alloy $Cu_{43}Zr_{43}Al_7Ag_7$. The red section is the run-in period, at which there is little friction due to a lack of wear debris along the track. The green region is the steady state region, and where the average friction force was measured. b) *k* versus average friction. c) *k* vs run in time. d) Run in time versus average friction. Only amorphous alloys are shown.

The final bulk property thought to possibly be related to the wear resistance was the average frictional force experienced by the pin. Higher frictional forces generally mean greater asperity contact, which should offer more opportunities for their removal, and, thereby, decreased wear performance. Figure 5-9a is a typical frictional force vs elapsed time plot generated during a test. The red shaded area is commonly known as the “run-in” period, during which the friction is low, as is wear loss (red area). At this point there is minimal wear debris along the track and little wear occurs. Once the material has worn a bit, friction rapidly increases and typically reaches a roughly equilibrium value (green area). This is the number used for the "average frictional force." Figure 5-9b shows wear resistance does not correlate with the amount of friction between the wearing surfaces. Interestingly, each alloy system also has a spread of coefficients of friction. Run-in times varied considerably from sample to sample, and they did not correlate with wear resistance (Figure 5-9c). This signifies the test went sufficiently long after run-in finished such that the majority of the testing time was done under abrasive wear conditions. Figure 5-9d demonstrates the lack of relationship even between the frictional force and run-in time. Unlike most other properties measured, this did not even appear to depend upon the alloy system. To reiterate, all samples were prepared with the same initial surface finish, each with a new pin, and all had the same force applied at the same radius.

Wear Under Differing Conditions

In order to help determine the extent to which the wear characteristics are a function of the state of the quenched liquid, two annealing studies were performed. The first was on $Zr_{35}Ti_{30}Be_{27.5}Cu_{7.5}$. This alloy was chosen both since it has previously had studies on the change in its mechanical properties after annealing[35] and because it was poor in wear. An alloy which readily wears will give a much larger result for a smaller percentage change in properties. To minimize the effects of oxidation during annealing, all samples were annealed under vacuum and surrounded with titanium turnings to serve as getters for oxygen leaking into the system. Samples were repolished after being annealed to remove any surface oxides. The annealing temperature of 553 K (~25 K below T_g) was chosen by analysis of the work done by Garret, et. al. Two samples were annealed, one for 120 minutes and the other for 240 minutes. A third sample was fully crystallized by annealing at 773 K for two hours (T_x is ~738 K). The two amorphous samples remained fully amorphous upon XRD and the crystallized sample did not have a visible amorphous hump.

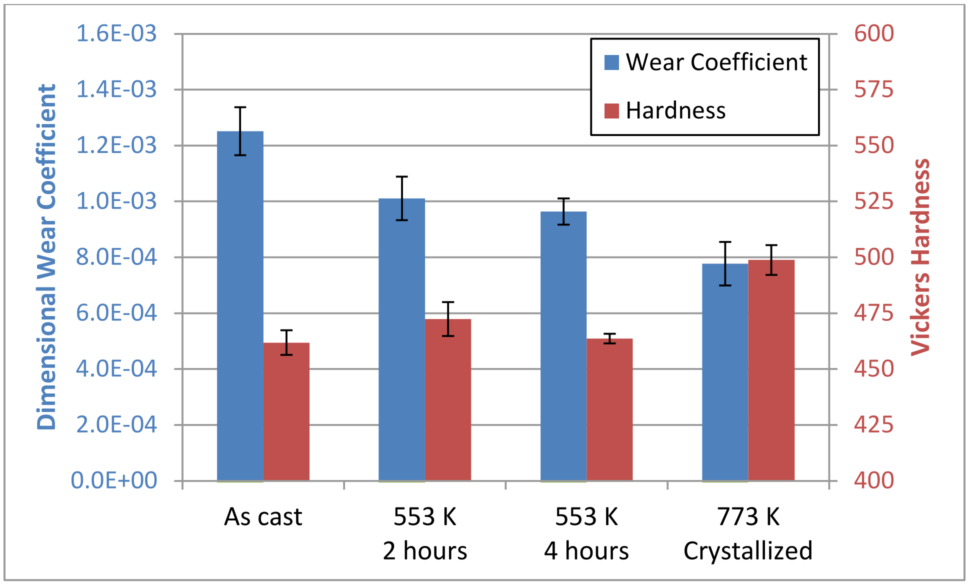

Figure 5-10: Wear loss and hardness data after annealing of $Zr_{35}Ti_{30}Be_{27.5}Cu_{7.5}$

While the dimensional wear coefficient compensates for the normal force applied and the distance worn, it does not account for the velocity of the pin relative to the sample. At this point in our experiments, a new apparatus had been constructed to replace the first, and it ran at a different speed than the first. As such, *k* values did not precisely match those of the alloy survey above. In order to compare between the differing setups, each alloy to be tested under specialized conditions was rerun. Figure 5-10 gives the results from both annealing and crystallizing $Zr_{35}Ti_{30}Be_{27.5}Cu_{7.5}$. Wear loss performance improves by 20% upon the initial two hours of annealing. Changing the annealing time to four hours affects the alloy minimally, with both the wear resistance and hardness staying roughly constant. After crystallization, however, wear performance is increased another 20%, while hardness changes from approximately 460 H_V to 500 H_V (an 8% change). The total difference in *k* is 1.25e-3 $mm^3/(N\text{-}m)$ for the as-cast sample to 7.78e-3 $mm^3/(N\text{-}m)$ after crystallization.

As can be seen in Appendix A, $Cu_{43}Zr_{43}Al_7Be_7$ was one of the highest performing fully amorphous alloys. In order to try and maximize its wear resistance, it was also given two annealing treatments as well as crystallized. The glass transition of the alloy was measured to be 718 K, with a crystallization temperature of 798 K. The first heat treatment was set at 693 K, about 45 K below T_g, for 5 hours. The second treatment was at 713 K for 0.5 hours. The final sample was crystallized at 863 K for 0.5 hours. XRD was performed on each sample to verify its state. The first stayed fully amorphous, the second displayed a very small amount of crystallization, and the third was fully crystalline.

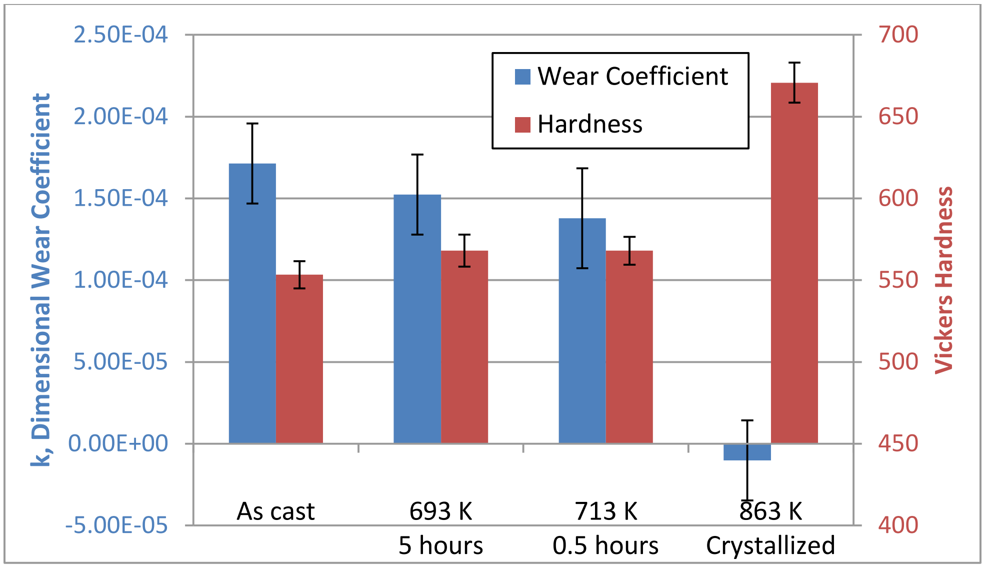

Figure 5-11: Wear loss and hardness data after annealing of $Cu_{43}Zr_{43}Al_7Be_7$

Like $Zr_{35}Ti_{30}Be_{27.5}Cu_{7.5}$,, the $Cu_{43}Zr_{43}Al_7Be_7$ alloy experienced significant changes upon annealing. Figure 5-11 shows *k* was initially 1.7e-4 mm³/(N-m). After annealing at 593 K for 5 hours, *k* decreased to 1.5e-4 mm³/(N-m). By heat treating 20 K hotter for half an hour, *k* was reduced yet again to 1.4e-4 mm³/(N-m). Compared to the as-cast state, this is an approximate 20% decrease in wear. Meanwhile, hardness increases marginally from 553 H_V to 568 H_V for both of the annealed samples. The crystallized sample greatly increased its hardness, up to 670 H_V, but actually experienced a net increase in mass.

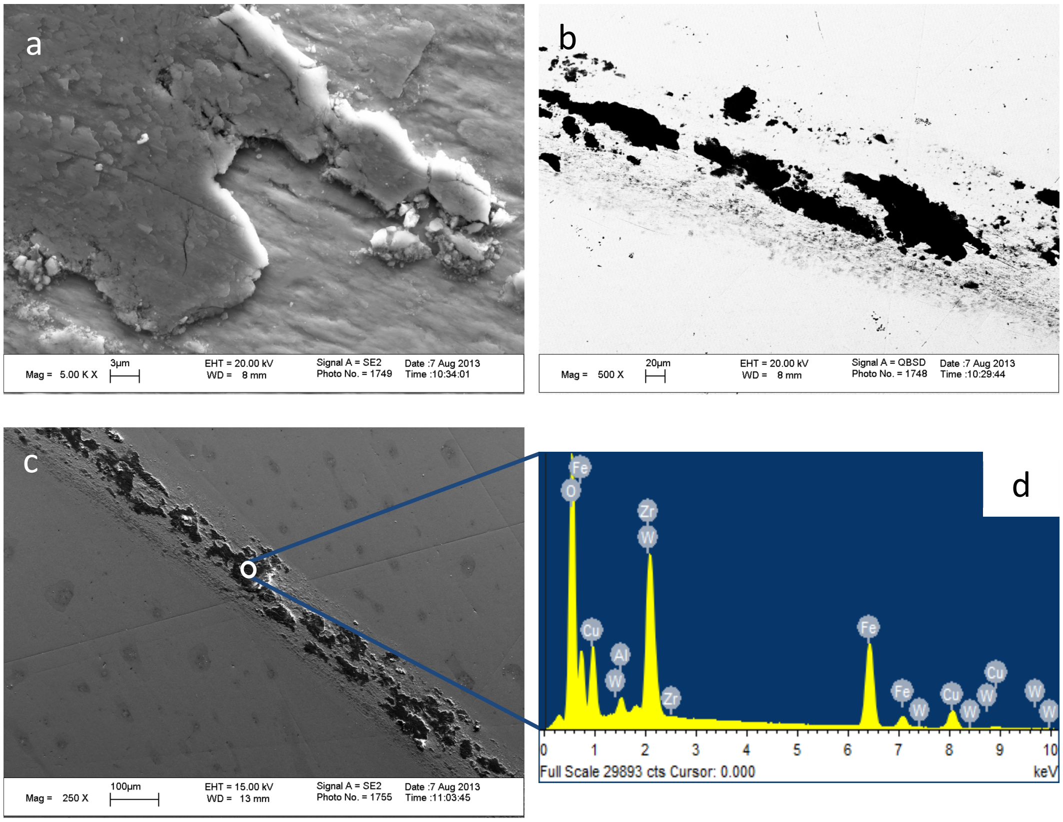

Figure 5-12: a) A micrograph of debris along the wear track of crystallized $Cu_{43}Zr_{43}Al_7Be_7$. b) A QBSD micrograph of the wear track. Brighter spots indicate higher Z elements. c) Location selected for EDS of wear debris. d) Lots of iron was found in the wear track, while none was found in bulk areas of the sample (not shown).

An increase in mass was an unexpected result, as one would expect that in an abrasive wear situation material would wind up being worn off of the surface, not added to it. Upon initial inspection under an optical microscope, it appeared material had worn off, and the anomalous results were due to measurement error. A second ingot was cast and crystallized, with similar results on wear tests on each side. Inspection of the wear surface was then performed via SEM. Figure 5-12a is a micrograph of the wear surface showing material deposited on the surface. Figure 5-12b, a quasi-backscattered electron diffraction micrograph, shows the wear track to be darker than the surrounding alloy. As QBSD images get their contrast from Z-scattering, darker areas are typically those with a lighter atomic number. The bulk of the alloy is comprised of Zr and Cu (Z of 40 and 29, respectively). The pin used in testing is a stainless steel variant, so the dominant elements should be Fe, Ni, and Cr (Z of 26, 28, and 24, respectively). As such, we should expect the brightness of any material originating from the pin to be much lighter than the alloy. Finally, EDS was performed along the wear track (Figure 5-12d) and off the track (not shown). Along the wear track Fe, Zr, Cu, and Al are all detected. Off of the wear track only Zr, Cu, and Al are detected (Be content cannot be detected due to the x-ray window being made out of Be). For this reason, it can be determined that the sample was minimally worn, but had a significant amount of material transferred to it from the pin.

The problem of material transfer from the pin is one which had been discussed early during testing, but it was decided to adhere to the ASTM standard. Great accuracy of measurements could have been achieved by more careful considerations of testing requirements. One solution would be to replace the relatively soft stainless steel ball bearings with a harder material, such as tungsten carbide. This exact change has been enacted by ASTM for the indenter used in Rockwell B hardness tests due to issues with the ball bearing indenter deforming after repeated loading.[36] A harder pin may also ensure a more consistent normal force applied to the sample during testing. As the pin gets worn down, the surface area in contact with the same increases, thereby decreasing the actual contact stress. If the pin wears at different rates against different materials, then each material will have differing contact stresses as the test evolves.

While many of the crystalline samples were exemplary and outperformed most of the amorphous alloys, they remained extremely brittle. In being so brittle, they would be able to be machined into gears without fracturing. However, it could be possible to take advantage of the high wear resistance of the crystalline phase by first machining out a gear, and then performing a heat treatment to either relax the glass or crystallize it. There is still the possibility of the toughness of individual gear teeth being too low to function, though. In this case, it may be possible to do a surface treatment along the lines of induction hardening, carburization, or nitriding, which are done to traditional gear materials. In the case of BMGs a technique along the lines of induction hardening of the gear teeth, or perhaps a pulsed laser technique to induce rapid heating only at the surface would be appropriate. As most wear tracks are only a few microns deep, only a thin surface layer would be needed to crystallize, while the rest could retain the tougher amorphous structure. It could be difficult, though, since crystallization is an exothermic process and the initial crystallization of a surface layer may initiate crystallization further into the bulk. In this idea for surface treatments, though, BMGs could be seen as a route to access the beneficial mechanical properties of brittle intermetallics while retaining the processing and toughness benefits of metallic glasses.

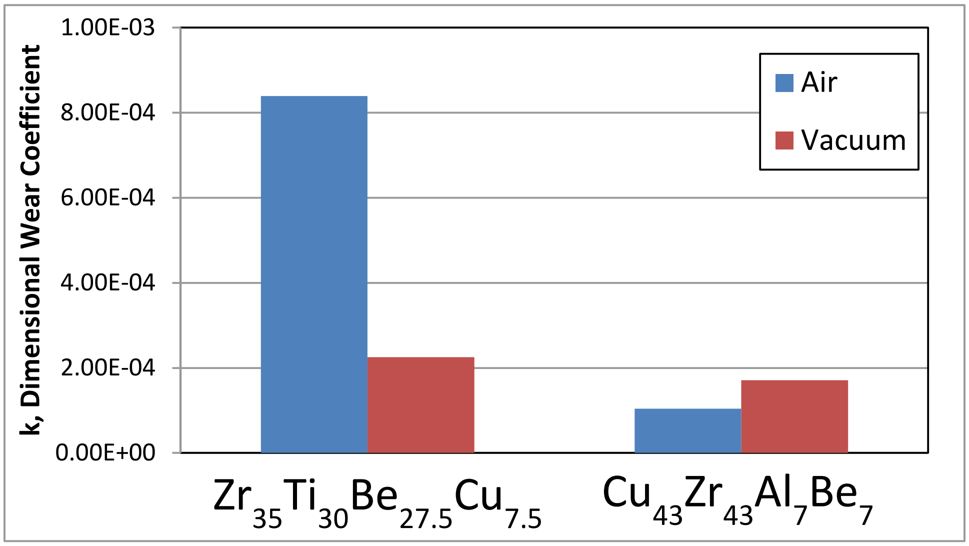

Figure 5-13: A comparison of wear coefficients for two alloys under air and vacuum. The ZrTi alloy sees notable improvements, while the CuZr alloy has decrease performance.

Finally, as suggested in the papers by Wu et al.[23,24] and Fu et al.[37], testing was performed under vacuum conditions for both of the alloys studied above. The same testing apparatus used in the annealing study was used here. The chamber was evacuated to $2x10^{-2}$ Pa, backfilled with argon, and then evacuated again to attempt to remove as much oxygen from the chamber as possible. Throughout the test the chamber continued to be pumped on in case of any slow vacuum leaks. Figure 5-13 demonstrates the effects of removing air from the testing chamber. $Zr_{35}Ti_{30}Be_{27.5}Cu_{7.5}$ experienced a 75% decrease in wear under vacuum, from *k* of 8.4e-4 $mm^3/(N\text{-}m)$ to 2.25e-4 $mm^3/(N\text{-}m)$. In $Cu_{43}Zr_{43}Al_7Be_7$, however, *k* actually increases 70%, from 1.0e-4 $mm^3/(N\text{-}m)$ to 1.7e-4 $mm^3/(N\text{-}m)$. Under vacuum both alloys wind up with similar performance.

From this data, is becomes apparent it is likely the surface oxide has a strong role to play in wear behavior. In the case of ZrTi-based alloys, which tended to have poorer wear behavior, the oxide could be brittle and both readily fracture off or regrow rapidly. Zr and Ti are both known to bond readily with oxygen (which is why they are often used in oxygen gettering systems). Meanwhile, the CuZr system may have a mechanically desirable oxide layer, as it provided superior wear protection in the presence of oxygen. Cross-sectional TEM performed by Wu et al. found multiple oxides present near the wear surface on samples tested in air and oxygen environments, and only one oxide phase with testing performed in argon.[23]

Concurrent to screening alloys, development was also being done on how to fabricate gears out of both metallic glasses and metallic glass matrix composites. The first technique attempted was semi-solid forging of BMGMC gears. This technique was chosen as BMGMCs were known to have high hardness and high toughness, both of which were thought to be desired for successful gears. The same semi-solid forging technique was used to fabricate these gears as the egg boxes from previous chapters. In this case, however, the mold was modified slightly. Two flat water cooled copper face plates were used for the faces, and the gear mold was just an internal gear purchased from a hobby shop. Ingots of DH1 ($Zr_{36.6}Ti_{31.4}Nb_7Cu_{5.9}Be_{19.1}$) were heated up to the semi-solid regime and then forged by pneumatic. The gear can then be removed from the mold with a press. Finally, a hole can be drilled into the center for an axel to pass through. Parts of the procedure and the finished gear are shown in Figure 5-14. SEM micrographs of the gear teeth are also shown. Fairly good replication of the tooth surface is achieved; however, it is far from perfect. There are pores present on the teeth, likely from air trapped by the molten front flowing into the mold. Two gears were also able to rotate smoothly when placed against each other.

The second technique used to fabricate gears was to take the coupons created for pin-on-disk testing. Due to the high hardness of metallic glasses, it would be exceedingly difficult to

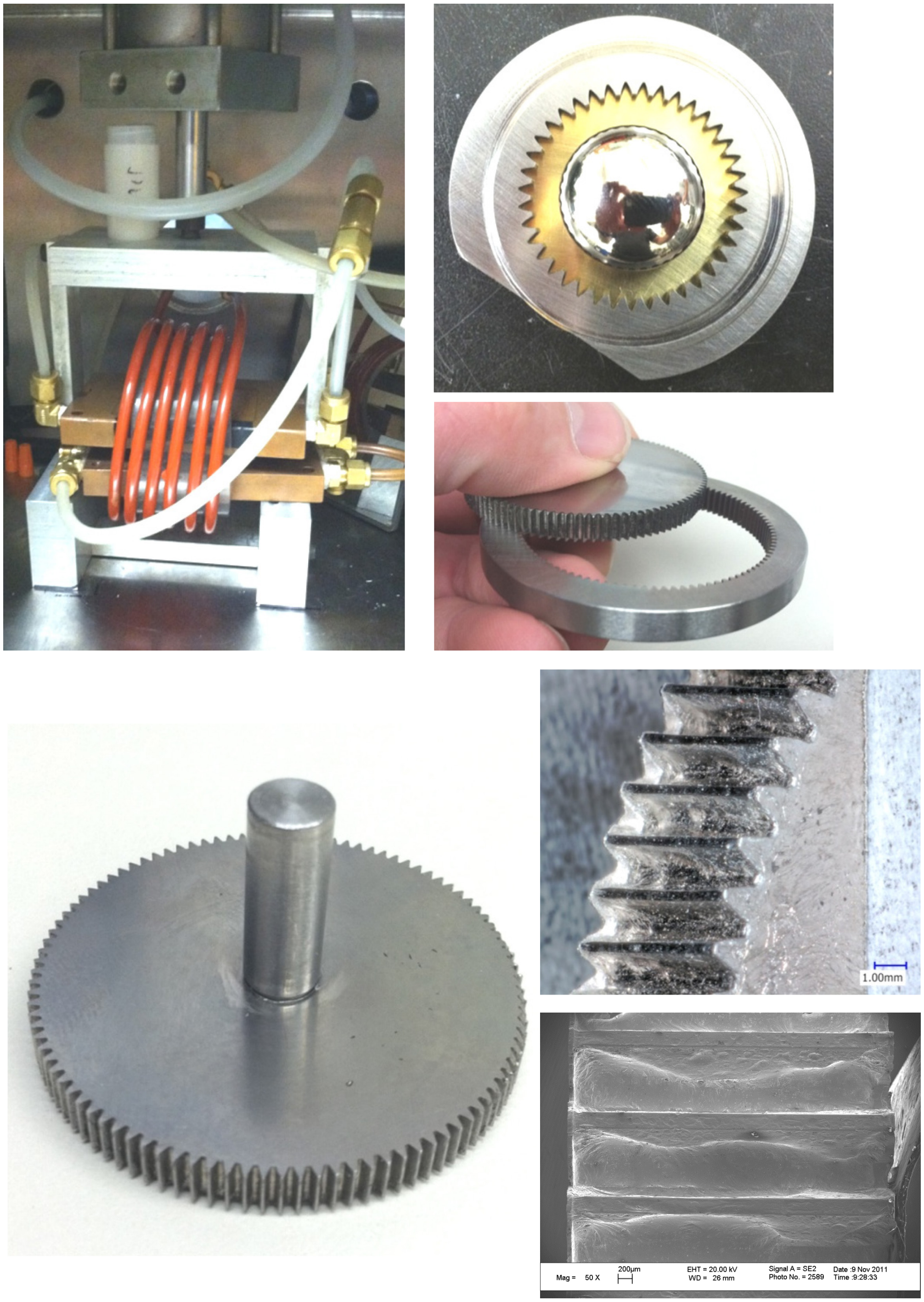

Figure 5-14: a) The semisolid forging setup. b) A prealloyed BMGMC ingot set up to be forged. c) A finished composite gear once it has been removed from the mold. d) The completed gear once it has had a hole drilled and axle inserted. e) A perspective image showing the finish on the gear teeth. f) A SEM micrograph where some of the casting defects are visible.

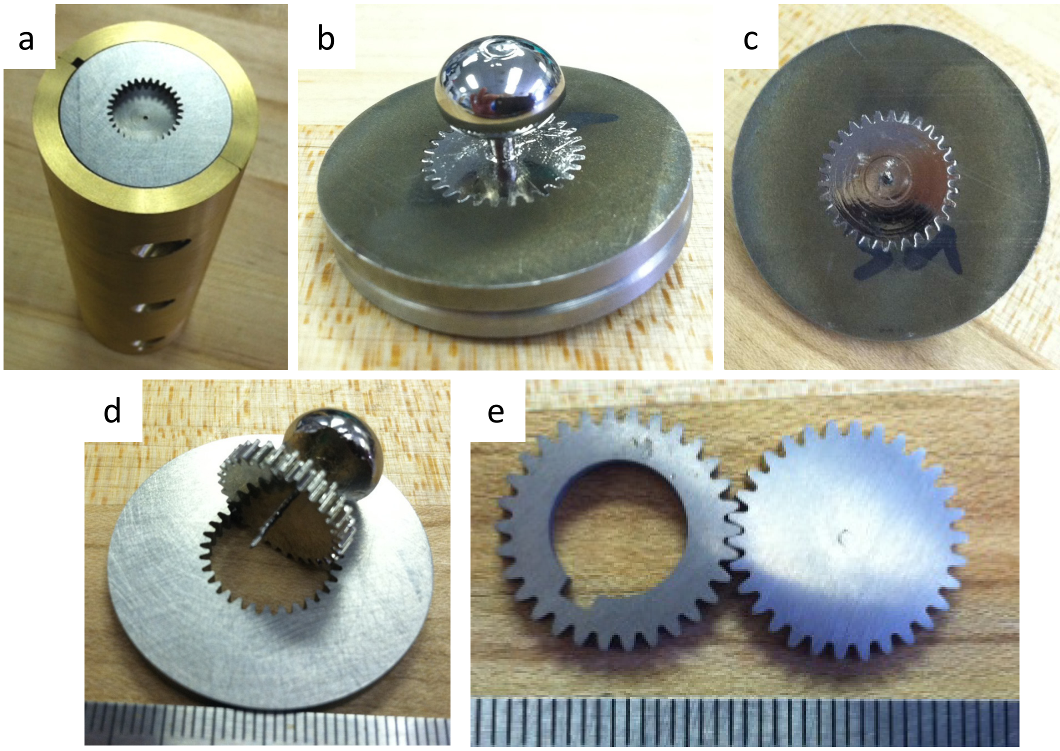

Figure 5-15: a) The gear mold fully assembled without the cap on top. b) An image a cast gear still in the mold. Upper gate material still connects to the pool it was cast from. c) The bottom of the mold. d) Gear once it has been removed from the mold. e) Left, gear with a keyway machined out. Right, a gear with flashing removed and faces ground to a 16 μm finish.

have them traditionally machined into the desired shape. Instead, they were wire EDMed. This worked well for tougher alloys (such as ZrTi and CuZr based systems), but all of the Ni composites fractured during the machining process, as expected, so they were unable to be made into gears.

The third method used to fabricate gears was suction casting. Figure 5-15a shows three of the four pieces used in the mold. The two brass sides separate, and there is a steel disk with a gear shape which has been wire EDMed into it. Finally, a copper cap with a gate goes on top where the ingot is melted. This design allows for casting a concentric shape (as opposed to if the gear was oriented vertically, in which case it would fill from the bottom teeth to the top) with no mold parting lines along the gear teeth. The rest of the figure shows the steps of removing the

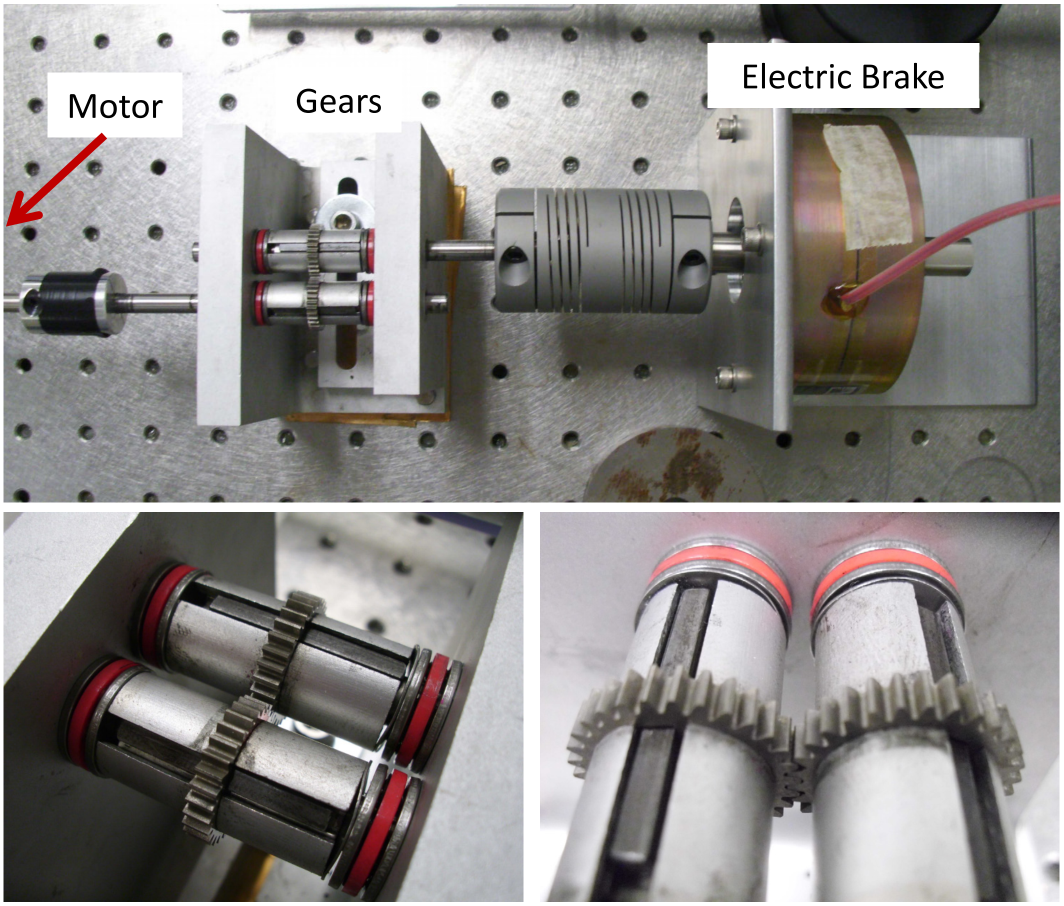

Figure 5-16: The gear testing machine. Key components are labeled.

gear, and then a gear which has had a keyway cut into it next to one without. The surface has been ground to a 16 μm finish on a polishing wheel. This method had not been perfected until the completion of initial testing, though, and will be used moving forward.

To perform wear testing on fabricated gears, yet another apparatus had to be used. It is shown in Figure 5-16. In this system, a speed controlled motor is connected to one side through a torque sensor. Meanwhile, the other side is connected to an electrically controlled brake, which enables constant loading on the gears. To emulate the conditions experienced by actual gearboxes in spacecraft, the electric brake was set to 10 lbs-in and the rotational speed to

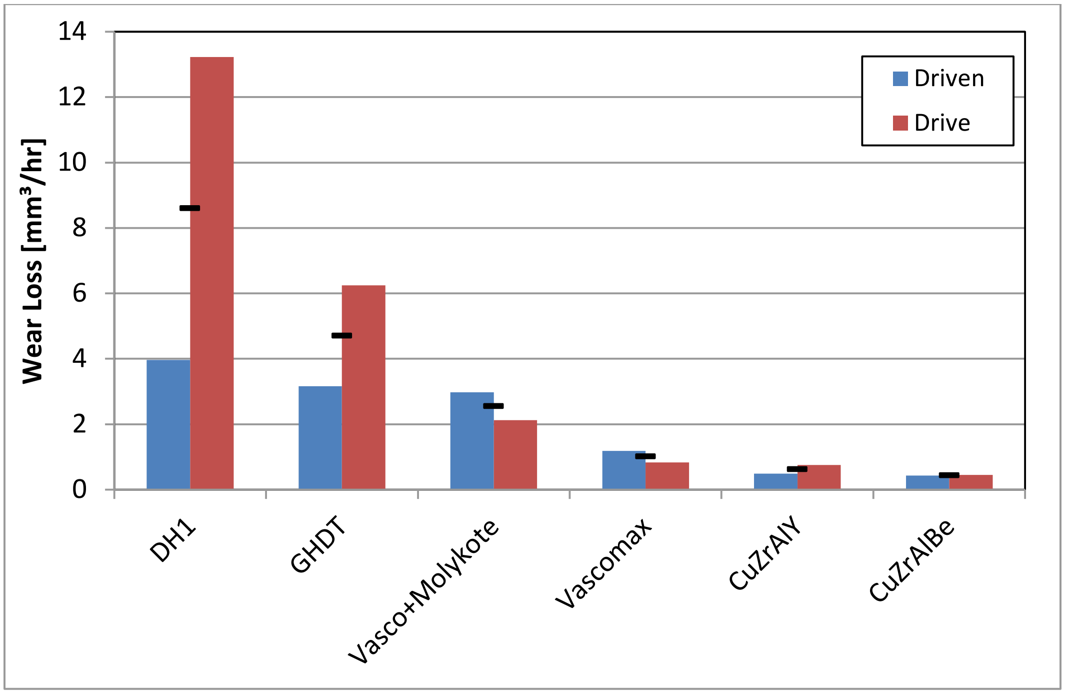

Figure 5-17: Wear loss per hour for each of the gear pairs tested.

4100 rpm. Each test began with a brief run-in period to remove any debris from the surface, and then the gears were run continuously for 3 hours.

Initially, five alloys were machined into gears for testing. The first, Vascomax C300, is the standard crystalline material currently used. The goal was to improve on its actual wear behavior. A variant with a Mo-Sr surface coating was also tested. The second, $Zr_{35}Ti_{30}Cu_{8.25}Be_{26.75}$ (GHDT), is a widely studied glass known for its superior fracture toughness and wide supercooled liquid region.[38] The third, $Zr_{55.3}Ti_{24.9}Nb_{10.8}Cu_{6.2}Be_{2.8}$ (DH1), is a BMGMC, and was intended to see how much using a high toughness material would impact the performance of a gear. $Cu_{47}Zr_{46}Al_5Y_2$ was the first of two CuZr alloys tested. It had the least mass loss of any fully amorphous material during POD testing. Finally, $Cu_{43}Zr_{43}Al_7Be_7$ was run, since it had become the benchmark CuZr alloy.

In a method similar to the pin-on-disk tests above, each gear was weighed multiple times both before and after testing. Each gear was tracked separately to see if any trends were present on wear behavior between the gear attached to the motor (drive) versus the one attached to the brake (driven). The mass loss was then divided by each alloy’s density to determine total volume lost. To compensate for the DH1 test having to be stopped only halfway through due to excessive wear, data is given in wear loss per hour. Figure 5-17 shows the final results of testing. Wear loss per hour is given for the driven gear in blue (on the left) while the drive gear is in red (on the right). Average wear loss between the two gears is shown as a solid black **-**.

DH1, the BMGMC and toughest glassy alloy tested, performed very poorly. It lost, on average, 8.6 mm^3/hr. It is quite possible this poor performance is due to the dual microstructure of the composite. It contains a soft, crystalline bcc dendrite which may be preferentially worn. This hypothesis was unable to be confirmed via SEM due to the smearing of material along the wear track. GHDT was the next poorest performer, losing 4.7 mm^3/hr. GHDT actually has a very similar composition to DH1’s matrix, so it is not too surprising its performance is similar. The main difference is that GHDT has a higher hardness at the expense of a lower toughness, and it instead retains an entirely amorphous microstructure. The two Vascomax alloys both performed well, but surprisingly the one with a coating had higher wear loss than the one without. The sample coated with MoSr lost 2.6 mm^3/hr versus 1.0 mm^3/hr for the uncoated. The coating seems to have quickly worn off, and then served as abrasive particles to increased abrasive wear on the gears. For this reason, care needs to be taken to any surface treatment given to a gear. If the treatment winds up being detrimental to the wear performance, it can greatly accelerate wear rates even after that layer has been removed. Both of the CuZr alloys performed the best.

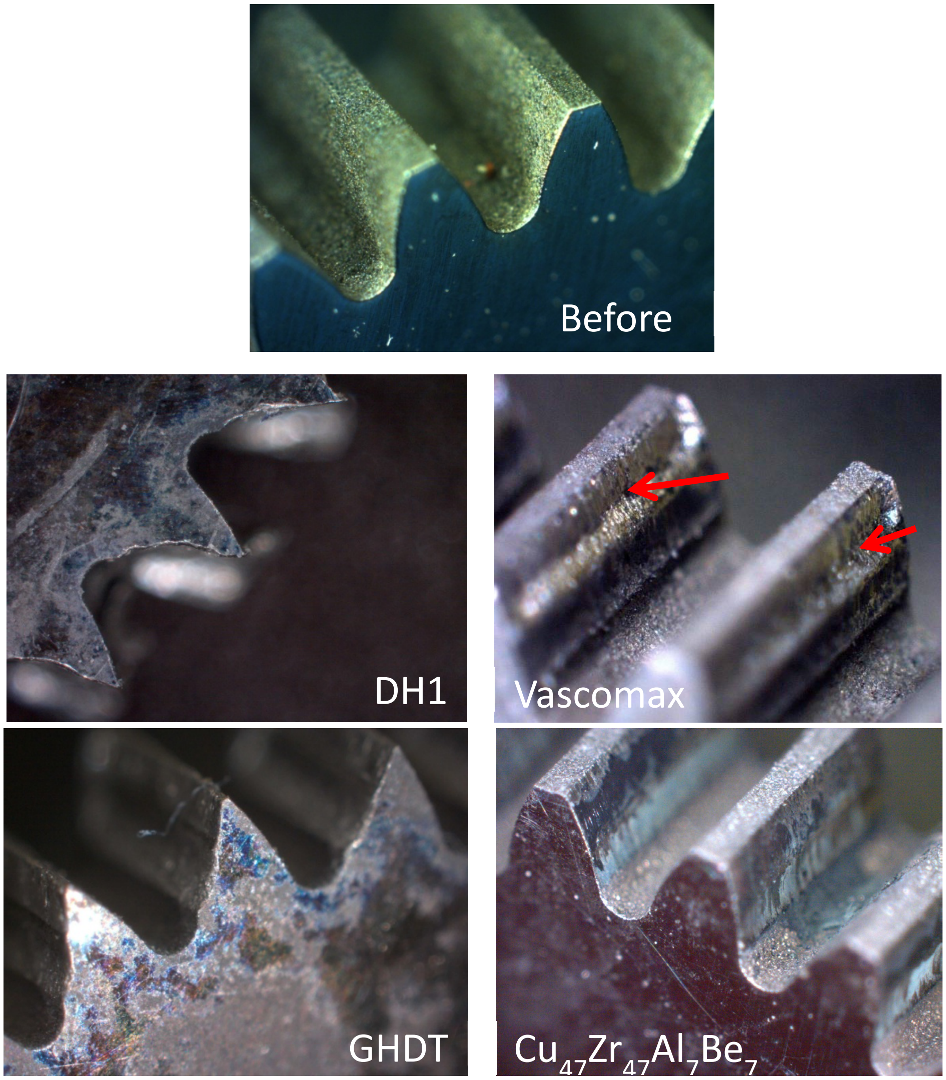

Figure 5-18: Top, appearance of gears prior to testing. Bottom, effects of wearing on each of the alloys. The arrows on the Vascomax image highlight their wear.

$Cu_{47}Zr_{46}Al_5Y_2$ lost 0.63 mm^3/hr and $Cu_{43}Zr_{43}Al_7Be_7$ lost only 0.44 mm^3/hr. This is less than half of the wear loss of the uncoated Vascomax gears. There does not seem to be a trend between whether the driven or driving gear wears more extensively.

The difference in wear between alloys is quite drastic when viewed directly. Figure 5-18 shows the difference between a new gear and ones which have undergone a complete wear test. The unworn gear is Vascomax 300, but all gears had a similar look (as they had all been

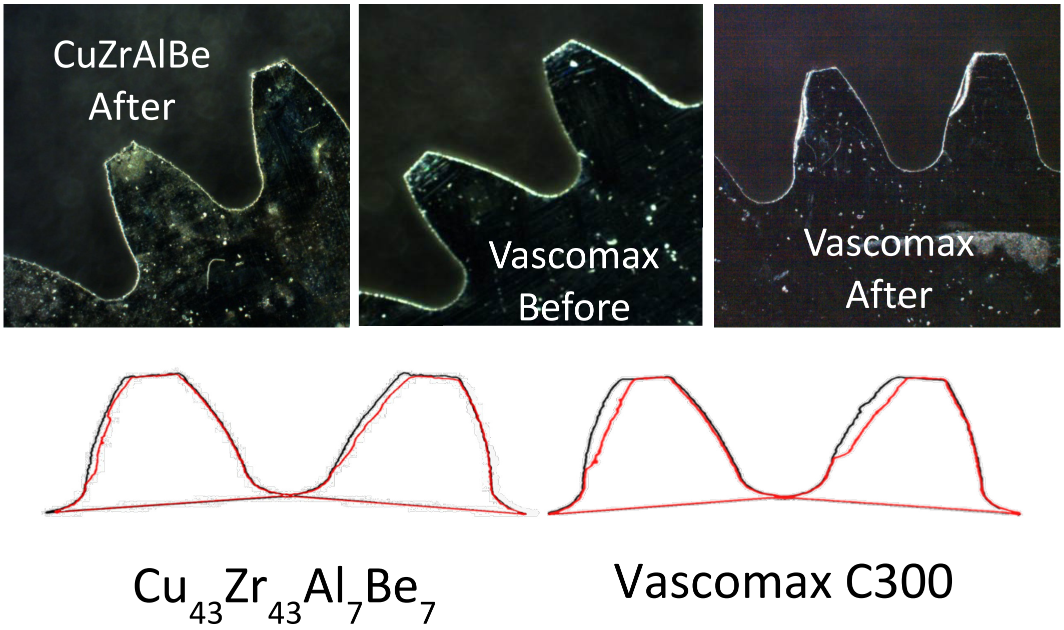

Figure 5-19: Above: Darkfield images of CuZrAlBe and uncoated Vascomax gears. Small amounts of wear can be seen on the left side of the teeth for both gears. Below: The difference in edge profiles between unworn (black) and worn (red) gears.

EDMed out of a plate). Both the DH1 and GHDT gears have had their teeth worn to sharp points. Again, the DH1 gear has actually been worn half as long as all the other gears to highlight how poorly it performed. The Vascomax gear has worn a little where the driving gear pushes against the one pictured (highlighted by arrows). The $Cu_{43}Zr_{43}Al_7Be_7$ gear also shows hardly any wear.

In order to highlight the difference in wear behavior, and possibly find a better way to inspect for wear on high performance gears, dark field micrographs were taken of both the Vascomax and $Cu_{43}Zr_{43}Al_7Be_7$ gears. Another set of micrographs were then taken post-test. By using dark field imaging, the edges of the gears became highlighted. By overlaying one image on the other, a difference in the profile of the gear teeth could easily be seen. Figure 5-19 contains a sample before image (Vascomax 300) as well as an after for both Vascomax and $Cu_{43}Zr_{43}Al_7Be_7$. The CuZr gear can be seen to experience a small change in profile after three hours of testing, while the Vascomax gear has lost a significant amount on one side of each tooth. By comparison both GHDT and DH1 experienced wear loss on both sides of every tooth, practically sharpening them to a point.

This study has encompassed a large variety of tasks. It began with initially attempting to screen out specific alloy systems which could be cast into fully amorphous 25.4 cm wide by 3 mm tall cylinders via arc melting. After many systems were attempted, success was found in the CuZr, Ni, and ZrTi systems. A variety of alloys within these systems were then cast and prepared for pin-on-disk testing. Even though metallic glasses are widely attributed with the property of “good in wear resistance,” it was found many are anything but. Wear tests created from commercially available, low quality, material in particular had lower than expected performance. However, many alloys were able to outperform the current state of the art in unlubricated, low load, sliding, abrasive wear test.

Little correlation was seen between any single sets of measured physical properties and wear resistance. Hardness, elastic modulus, bulk modulus, shear modulus, Poisson’s ratio, and toughness all seemed to be fairly independent of wear behavior. It was possible to modify wear performance in two alloy systems (CuZr and ZrTi) by both annealing and crystallization. Allowing the supercooled liquid to relax at different temperatures led to higher amounts of wear resistance without simultaneously introducing significant hardness changes. Crystallization dramatically increased the wear resistance of the ZrTi alloy. In the case of the CuZr alloy, it actually leads to adhesive wear, where material was only removed from the pin and the sample was left mostly unscathed. Pin-on-disk testing was also performed under vacuum to try and determine the effect of oxygen on wear behavior. The ZrTi alloy saw a 75% improvement in wear resistance, while the CuZr alloy performed about 75% worse. In terms of absolutes, though, the CuZr alloy was still superior.

To continue development, gears were fabricated by multiple methods. First, composite gears were semisolidly forged. Then, gears were EDMed out of suction cast plates. Finally, gears were able to be directly suction cast with only the wire EDM required for cutting the internal hole. Pairs of gears were then able to be run against each other for multiple hours, and measurements were made of total wear loss on gears. $Cu_{43}Zr_{43}Al_7Be_7$ had the best performance, having less than half the volume of material lost compared to Vascomax 300, the current material used.

The performance increases obtained by BMGs are expected to increase once tests are performed at cryogenic temperatures. Vascomax is known to become brittle and exhibits large amounts of wear, but as shown in previous chapters, fully amorphous glasses can retain much of their room temperature toughness. Other future work can include new processing techniques, such as linear injection casting, to reduce porosity and flow lines upon casting compared to suction casting. It would also be advantageous to be able to directly cast gears with keyways in them, eliminating the requirement to EDM them out, as that may open up the possibility of using glasses with lower toughness.

The author would like to thank Laura Andersen and Niccolo Valigi for their invaluable contributions in performing measurements during their internships at the Jet Propulsion Laboratory.

Conclusions

While many publications in the literature have claimed numerous relationships between the wear resistance of metallic glasses and their mechanical properties, it is only through a thorough study of many alloys under the same testing conditions a claim such as this can be made. Unfortunately, there is not a universal property which makes metallic glasses perform better in wear. The only consistently measured value is CuZr's ability to resist wear across all sets of mechanical properties. CuZr has shown to exhibit a different oxide structure on the surface, as samples left out in air for several months begin to tarnish, while no other Zr, ZrTi, Ni, or Fe-based glasses do. Future studies should focus on identifying what is present on this surface. Possible methods for doing this are cross-sectional SEM, cross-sectional TEM, XPS identification of the elemental composition as a function of depth from the surface, XRD analysis of the wear debris under atmosphere, vacuum, and an oxygen-rich environment. Further studies must also be performed on the effects of lubrication, as well as cryogenic temperatures. One substantial mechanical property, to this point, has also been mostly ignored. Fracture toughness has also been cited as a measure of wear behavior. All of the above factors will need to be taken into account, as any compounds present on the surface of a wearing gear will also have their own unique set of mechanical properties.

References

(1) Hofmann, D. C.; Suh, J.-Y.; Wiest, A.; Lind, M.-L.; Demetriou, M. D.; Johnson, W. L. Development of tough, low-density titanium-based bulk metallic glass matrix composites with tensile ductility. *Proc. Natl. Acad. Sci. U. S. A.* **2008**, *105*, 20136–40.

(2) Demetriou, M. D.; Launey, M. E.; Garrett, G.; Schramm, J. P.; Hofmann, D. C.; Johnson, W. L.; Ritchie, R. O. A damage-tolerant glass. *Nat. Mater.* **2011**, *10*, 123–8.

(3) Naka, M.; Hashimoto, K.; Masumoto, T. High Corrosion-Resistance of Chromium-Bearing Amorphous Iron-Alloys in Neutral and Acidic Solutions Containing Chloride. *Corrosion* **1976**, *32*, 146–152.

(4) Naka, M.; Hashimoto, K.; Inoue, A.; Masumoto, T. Corrosion-Resistant Amorphous Fe-C Alloys Containing Chromium and/or Molybdenum. *J. Non. Cryst. Solids* **1979**, *31*, 347–354.

(5) Schroers, J. Processing of bulk metallic glass. *Adv. Mater.* **2010**, *22*, 1566–97.

(6) Boswell, P. Wear-Resistance of a Liquid Quenched Metallic Glass. *J. Mater. Sci.* **1979**, *14*, 1505–1507.

(7) Standard Test Method for Wear Testing with a Pin-on-Disk Apparatus **2010**.

(8) Galloway, J.; Bhatt; S Evaluating polymer wear and particulation for semiconductors and data storage http://www.gslb.cleanrooms.com/index/display/article-display/0723054128/articles/solid-state-technology/semiconductors/subsystems/2010/11/evaluating-polymer-wear-and-particulation-for-semiconductors-and.html (accessed Nov 10, 2013).

(9) Prakash, B.; Hiratsuka, K. Sliding wear behavior of some Fe-, Co-, and Ni-based metallic glasses during rubbing against bearing steel. *Tribol. Lett.* **2000**, *8*, 153–160.

(10) Li, G.; Wang, Y. Q.; Wang, L. M.; Gao, Y. P.; Zhang, R. J.; Zhan, Z. J.; Sun, L. L.; Zhang, J.; Wang, W. K. Wear behavior of bulk Zr 41 Ti 14 Cu 12.5 Ni 10 Be 22.5 metallic glasses. *J. Mater. Res.* **2002**, *17*, 1877–1880.

(11) Tam, R. C. Y.; Shek, C. H. Abrasion resistance of Cu based bulk metallic glasses. *J. Non. Cryst. Solids* **2004**, *347*, 268–272.

(12) Parlar, Z.; Bakkal, M.; Shih, A. J. Sliding tribological characteristics of Zr-based bulk metallic glass. *Intermetallics* **2008**, *16*, 34–41.

(13) Tao, P. J.; Yang, Y. Z.; Ru, Q. Effect of rotational sliding velocity on surface friction and wear behavior in Zr-based bulk metallic glass. *J. Alloys Compd.* **2010**, *492*, L36–L39.

(14) Huang, D.; Li, R.; Huang, L.; Ji, V.; Zhang, T. Fretting wear behavior of bulk amorphous steel. *Intermetallics* **2011**, *19*, 1385–1389.

(15) Segu, D. Z.; Choi, J. H.; Yi, S.; Kim, S. S. Dry Sliding Tribological Properties of Fe-Based Bulk Metallic Glass. *Tribol. Lett.* **2012**, *47*, 131–138.

(16) Tam, C. Y.; Shek, C. H. Abrasive wear of Cu60Zr30Ti10 bulk metallic glass. *Mater. Sci. Eng. A* **2004**, *384*, 138–142.

(17) Maddala, D.; Hebert, R. J. Effect of notch toughness and hardness on sliding wear of Cu50Hf41.5Al8.5 bulk metallic glass. *Scr. Mater.* **2011**, *65*, 630–633.

(18) Liu, Y.; Yitian, Z.; Xuekun, L.; Liu, Z. Wear behavior of a Zr-based bulk metallic glass and its composites. *J. Alloys Compd.* **2010**, *503*, 138–144.

(19) Chen, B.; Li, Y.; Li, R.; Pang, S.; Cai, Y.; Wang, H.; Zhang, T. Influence of laser surface melting on glass formation and tribological behaviors of Zr55Al10Ni5Cu30 alloy. *J. Mater. Res.* **2011**, *26*, 2642–2652.

(20) Liu, G.; An, Y.; Chen, J.; Hou, G.; Chen, J. Influence of Heat Treatment on Microstructure and Sliding Wear of Thermally Sprayed Fe-Based Metallic Glass Coatings. *Tribol. Lett.* **2012**, *46*, 131–138.

(21) Choi, H.; Jo, H.; An, K.; Yoon, S.; Lee, C. Tribological behavior of the kinetic sprayed Ni59Ti16Zr20Si2Sn3 bulk metallic glass. *J. Alloys Compd.* **2007**, *434-435*, 64–67.

(22) Duan, H.; Wu, Y.; Meng, H.; Wang, J.; Tu, J.; Kou, H.; Li, Y.; Zhang, T.; Li, J. Tribological properties of Zr41.25Ti13.75Ni10Cu12.5Be22.5 bulk metallic glasses under different conditions. *J. Alloys Compd.* **2012**, *528*, 74–78.

(23) Wu, H.; Baker, I.; Liu, Y.; Wu, X.; Munroe, P. R. Effects of environment on the sliding tribological behaviors of Zr-based bulk metallic glass. *Intermetallics* **2012**, *25*, 115–125.

(24) Wu, H.; Baker, I.; Liu, Y.; Wu, X. Dry sliding tribological behavior of Zr-based bulk metallic glass. *Trans. Nonferrous Met. Soc. China* **2012**, *22*, 585–589.

(25) Ishida, M.; Takeda, H.; Nishiyama, N.; Kita, K.; Shimizu, Y.; Saotome, Y.; Inoue, A. Wear resistivity of super-precision microgear made of Ni-based metallic glass. *Mater. Sci. Eng. A* **2007**, *449-451*, 149–154.

(26) Kwon, D. H.; Park, E. S.; Huh, M. Y.; Kim, H. J.; Bae, J. C. Wear behavior of Fe-based bulk metallic glass composites. *J. Alloys Compd.* **2011**, *509*, S105–S108.

(27) *CRC Handbook of Lubrication and Technology, Volume III: Monitoring, Materials, Synthetic Lubricants, and Applications*; Booser, E. R., Ed.; 3rd ed.; Taylor & Francis, 1993.

(28) Bhushan, B. *Introduction to Tribology*; 1st ed.; Wiley, 2002.

(29) Zhang, G. Q.; Li, X. J.; Shao, M.; Wang, L. N.; Yang, J. L.; Gao, L. P.; Chen, L. Y.; Liu, C. X. Wear behavior of a series of Zr-based bulk metallic glasses. *Mater. Sci. Eng. A* **2008**, *475*, 124–127.

(30) Oberle, T. L. Properties Influencing Wear of Metals. *J. Met.* **1951**, *3*, 438–446.

(31) Leyland, A.; Matthews, A. On the significance of the H/E ratio in wear control: a nanocomposite coating approach to optimised tribological behaviour. *Wear* **2000**, *246*, 1–11.

(32) Lind, M.; Duan, G.; Johnson, W. Isoconfigurational Elastic Constants and Liquid Fragility of a Bulk Metallic Glass Forming Alloy. *Phys. Rev. Lett.* **2006**, *97*, 015501.

(33) Greer, a. L.; Rutherford, K. L.; Hutchings, I. M. Wear resistance of amorphous alloys and related materials. *Int. Mater. Rev.* **2002**, *47*, 87–112.

(34) Archard, J. F.; Hirst, W. The Wear of Metals under Unlubricated Conditions. *Proc. R. Soc. A Math. Phys. Eng. Sci.* **1956**, *236*, 397–410.

(35) Garrett, G. Study of the origins of toughness in amorphous metals, California Institute of Technology, 2013, pp. 35–57.

(36) ASTM Standard E18 - 2012, “Standard Test Methods for Rockwell Hardness of Metallic Materials” **2012**.

(37) Fu, X.; Kasai, T.; Falk, M. L.; Rigney, D. A. Sliding behavior of metallic glass Part I . Experimental investigations. *Wear* **2001**, *250*, 409–419.

(38) Duan, G.; Wiest, A.; Lind, M. L.; Li, J.; Rhim, W.-K.; Johnson, W. L. Bulk Metallic Glass with Benchmark Thermoplastic Processability. *Adv. Mater.* **2007**, *19*, 4272–4275.

Chapter 6 – Characterization of Two Gradient Alloys Fabricated by Laser Engineered Net Shaping

Additive manufacturing is a relatively new field based around the idea of depositing one layer of a material at a time in order to build a three dimensional structure. It is also commonly known as rapid prototyping or 3D printing. Typical additive manufacturing processes begin with a computer-designed part. A layering path is then generated by software, and is input into the machine to build the part. Traditional machining processes require removal of material in order to create a final shape. Additive manufacturing works in the reverse, only depositing material required for the finished product. It also provides extra flexibility, allowing for hollow, low density, or blind structures to be manufactured, features that are difficult or impossible to obtain with traditional machining.

A variety of additive manufacturing processes have been developed recently. The most common technique is known as fused deposition modeling (FDM). A thin filament is pushed through a heated nozzle which can be positioned in an x-y plane. Either the nozzle or build surface is then moved after each layer. The filament is most commonly made out of a polymer, although variants which use metal feedstock are also under development. Surface finishes range from very rough to smooth, and are often directly related to the price of the printing machine and the total size of the smallest feature. Resolution can also be sacrificed to increase printing speed by increasing layer thickness.

Another common technique is photopolymerization. In this case, a tank with a build platform near the surface is filled with a photosensitive polymer solution. A laser is then used to activate desired sections and instigate polymerization. The build table is then lowered, and the next layer is polymerized. This technique can offer high quality surface finishes, but tends to be slow and can only be used with polymers.

A third technique involves using powders as feedstock material, and there are three variants; in one version a powder is mixed with a binder and printed similar to FDM above. After printing, the final product can be sintered or thermoset. This results in a good quality surface, but it is not fully dense or necessarily mechanically robust. A second version, called direct metal laser sintering, is similar to photopolymerization, except instead of using a pool of liquid it employs a base layer of metallic powder.[1] A powerful laser is then used to melt the desired areas, a new layer of powder is added, and the process is repeated.

The technique used in this study, laser engineered net shaping (LENS), uses a nozzle to inject metallic powder into the laser. This removes the need for a bed of metallic powder, so only the powder to be melted is needed. Another benefit of LENS is the production of fully dense parts. This is because it melts powder instead of using sintering for consolidation. Figure 6-1 contains a schematic of the LENS machine used in this study, which has been outfitted with four nozzles, each capable of feeding from a different hopper (as shown in Figure 6-1a). This technique has been used in the literature to fabricate samples transitioning from one alloy to another; however, previous research largely focused on studying hardness and dislocations, not the formation of the gradient..[2–4]

In this study, pillars were made which transition from Ti-6Al-4V to pure vanadium. They were printed on a Ti-6Al-4V plate, with the Ti-6Al-4V deposited first, and transitioning to V on top. Figure 6-1b shows a pillar during the build process. Figure 6-1c and 6-1d show the completed structures. Table 6-1 outlines the parameters for building the pillar. Each layer was 0.38 mm thick; steps were done in 3% volume increments. Each composition was five layers thick, and a total of 195 individual layers were deposited over 585 minutes. The laser's power was held at a constant 600 W, with 4.4 LPM of argon gas flowing. The build process was done in a series of small, linear steps to minimize microstructural differences from one layer to another.

This proved to be a successful technique, as compared to other pillar composition gradients, which suffered failures in transition regimes that had larger changes in composition (as much as 25% different) from one layer to the next.

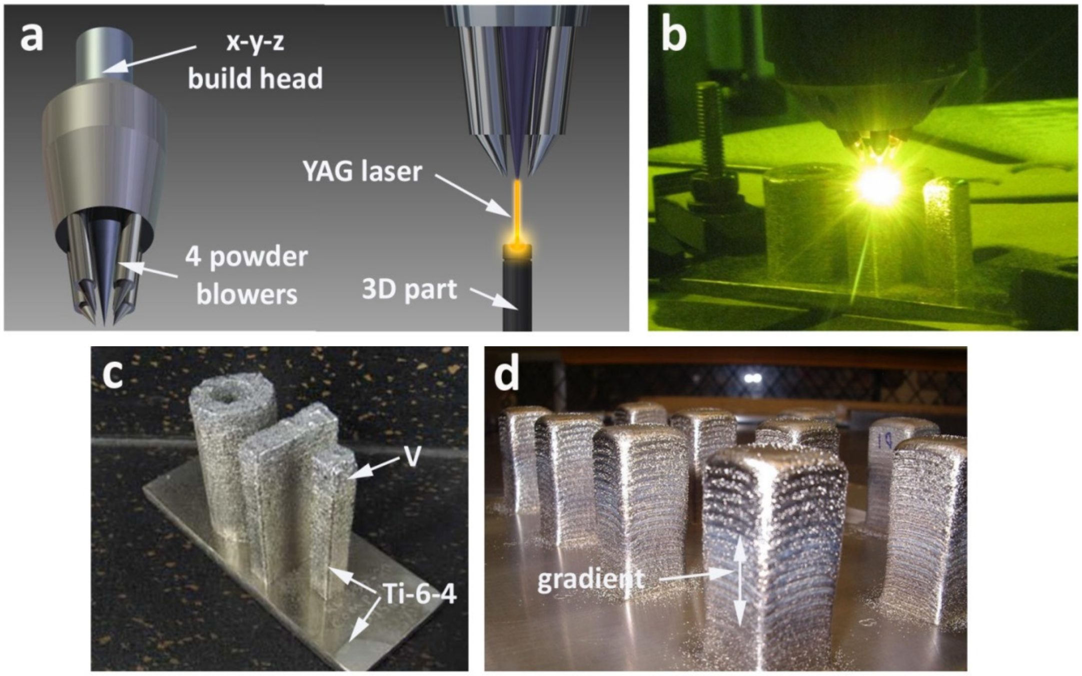

Figure 6-1: Schematic of the laser deposition (LD) building heads used to fabricate gradient alloys. **(b)** Image of the LD process fabricating several test specimens of the Ti-V gradients. **(c)** Three gradient alloy specimens; a hollow cylinder, a plate and a beam. **(d)** Example of a “forest” of gradient alloy posts used to vary gradient compositions.

Table 6-1: Build conditions for the Ti-6Al-4V gradient alloy.

Layers	% vol Ti-6-4	% vol V	g/min Ti-6-4	g/min V
0-28	100%	0%	2.1	0
29-33	97%	3%	2.04	0.08
34-38	94%	6%	1.97	0.16
39-43	91%	9%	1.91	0.24
44-48	88%	12%	1.85	0.31
49-53	85%	15%	1.79	0.39
54-58	82%	18%	1.72	0.47
59-63	79%	21%	1.66	0.55
64-68	76%	24%	1.59	0.63
69-73	73%	27%	1.53	0.71
74-78	70%	30%	1.47	0.78
79-83	67%	33%	1.41	0.86
84-88	64%	36%	1.34	0.91
89-93	61%	39%	1.28	1.02
94-98	58%	42%	1.22	1.1
99-103	55%	45%	1.16	1.18
104-108	52%	48%	1.09	1.26
109-113	49%	51%	1.57	2.03
114-118	46%	54%	1.52	2.15
119-123	43%	57%	1.42	2.27
124-128	40%	60%	1.32	2.39
129-133	37%	63%	1.22	2.51
134-138	34%	66%	1.12	2.63
139-143	31%	69%	1.02	2.75
144-148	28%	72%	0.92	2.87
149-153	25%	75%	0.83	2.99
154-158	22%	78%	0.73	3.11
159-162	19%	81%	0.62	3.23
163-166	16%	84%	0.53	3.35
167-170	13%	87%	0.43	3.47
171-174	10%	90%	0.3	3.58
175-178	7%	93%	0.23	3.71
179-182	4%	96%	0.13	3.83
183-186	1%	99%	0.03	3.94
187-195	0%	100%	0	3.98

The gradient alloy used in this study was chosen to provide a structure which would be high-strength and low-density at one end and have a high melting point at the other. An example of where such a design would be ideal is a rocket nozzle transitioning directly into the body, eliminating the need for a joining process between the two.

X-ray diffraction (XRD) was performed to verify successful fabrication, and to determine which phases were produced. The pillars were serial sectioned on an Allied Techcut 5 laboratory saw. The face of each sample was inspected via XRD to determine the phases present in its microstructure.

Standard Ti-6Al-4V is a mixture of both α (hcp) and β (bcc) crystal structures, while elemental vanadium is purely bcc. Figure 6-2a is a binary phase diagram of titanium and vanadium. A large, single phase bcc region is seen at elevated temperatures, with only minimal solubility of vanadium into the hcp phase. In equilibrium at temperatures below 873 K, a two phase mixture is expected for compositions ranging from roughly 5% to 90% vanadium. This is supported by the ternary phase diagrams of Ti-Al-V given at 600 K, 900 K, and 1200 K (Figure 6-2b-d, respectively). A representation of the path taken through the alloy is drawn on the ternary phase diagrams. The transition of Ti-6Al-4V to vanadium was chosen since it thermodynamically avoids any intermetallic phases. Another low density, high strength alloy is Al-2024. However, the transition from a predominantly aluminum alloy to vanadium would cross through a number of intermetallic phases. For aluminum to vanadium, the alloy would start as fcc, then change to a stoichiometric fcc, tetragonal, monoclinic, hexagonal, and body centered cubic phases, followed by bcc vanadium.[5] All of these different crystal structures create all sorts of different interfaces and wildly different mechanical properties within the material. By choosing to transition from predominantly titanium to vanadium, much of this issue is avoided.

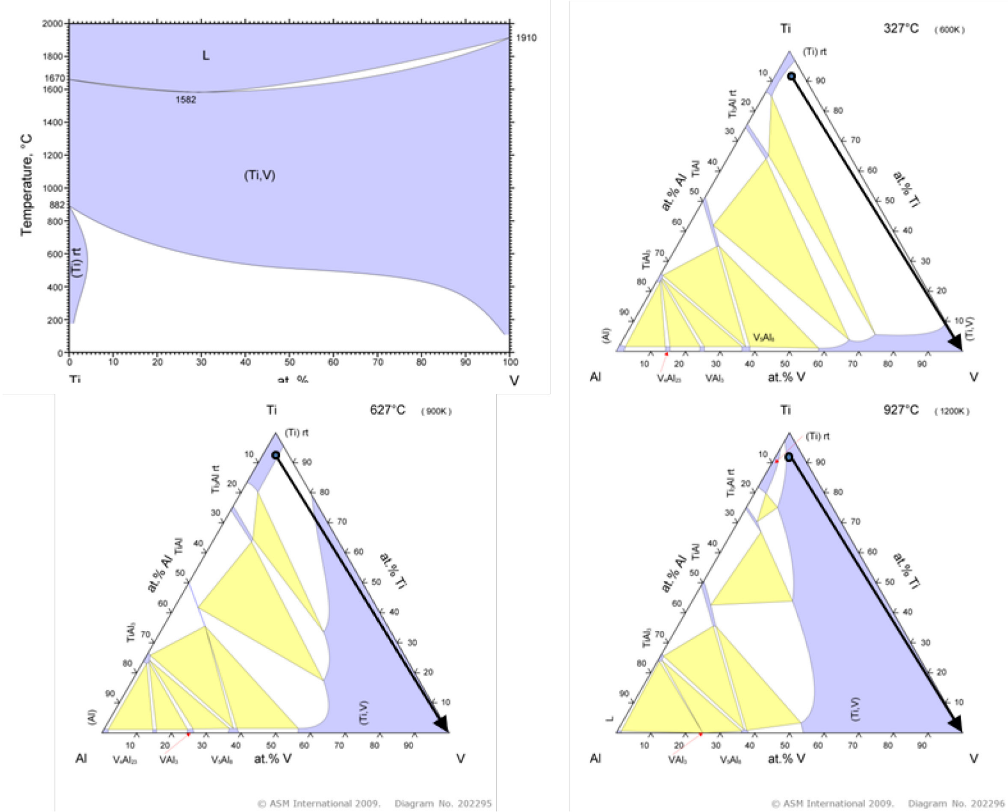

Figure 6-2: (a) A binary Ti-V phase diagram. α is hcp and β is bcc. (b) Ternary Ti-Al-V phase diagram. The addition of aluminum to the system appears to broaden the two phase region slightly. The outlined path demonstrates the compositions contained in the tested pillar.[6,7]

Of course, real manufacturing processes do not always wind up with what is expected from thermodynamic equilibrium. Figure 6-3b was constructed by serial-sectioning a pillar and performing XRD on each surface. At the pure Ti-6Al-4V side, only the hcp α is visible. After only a few layers, bcc peaks also begin to appear and coexist with the hcp phase. By only ~15% of the way to pure vanadium, all hcp peaks have disappeared and only bcc remain. This does not match up with the results predicted from the phase diagrams in Figure 6-2. It is actually closer in line to the equilibrium phase compositions seen at 900 K in the Ti-Al-V ternary phase diagram. However, since these materials are deposited layer by layer, it is likely they experience a fairly rapid quench rate. Therefore, they won't have time to reach an equilibrium state. Individual XRD patterns are shown in Figure 6-3c(i-v). (i) is pure Ti-6Al-4V, but only contains bcc. (ii) has the

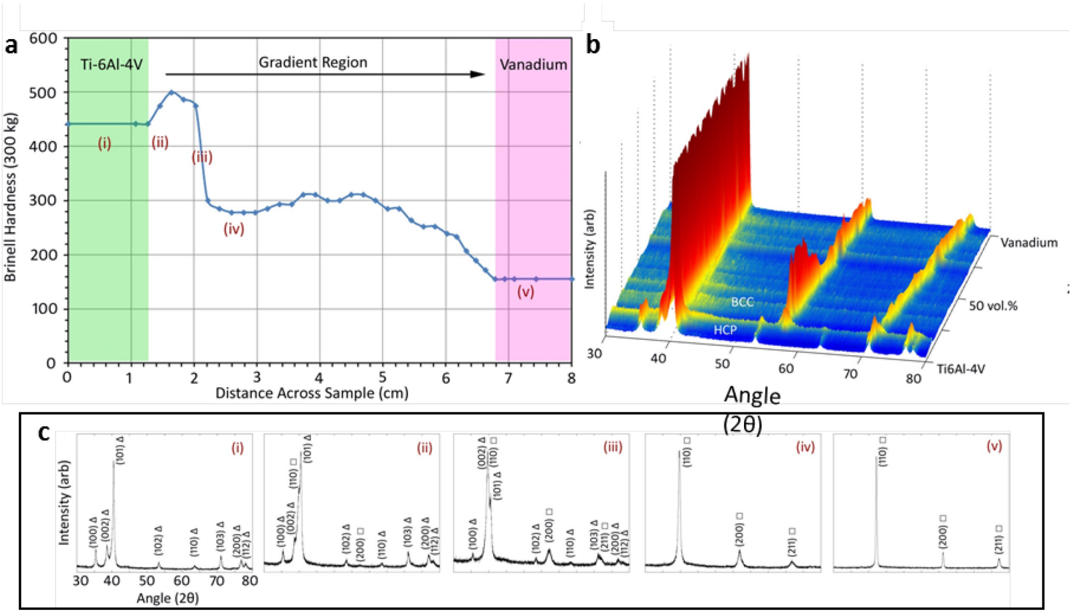

Figure 6-3: (a) A hardness vs position plot for the Ti-6-4 to V sample. (b) 3d mapping of XRD intensities across the sample. A slow change in diffraction angles is apparent in the BCC phase. (c) Indexed diffraction patterns identified to in (a). The coexistance of both HCP and BCC phases is demonstrated.

beginning of bcc presence, and (iii) has diminishing levels of hcp. By (iv) only the bcc phase exists, and that continues all the way through (v).

Figure 6-3a shows more evidence for the gradual changes of phase. Initially, in the Ti-6Al-4V region (i), the hardness is roughly 440 Brinell. In the two phase region (ii and iii) the hardness is increased to a maximum of 500 Brinell. By (iv), when only bcc is present, the hardness fluctuates around 300 Brinell. It then trails off to vanadium's normal value of 160 Brinell.

As mentioned above, having minimal crystal structure changes is desirable in a gradient alloy. Likewise, having a small, gradual, change in lattice parameter would likely mean fewer weak interfaces between layers. It is subtle, but in Figure 6-3, a shift in the position of the diffracted peaks is demonstrable. It is most visible in the (211) bcc reflection in Figure 6-3b. By indexing each peak, and using Bragg's law, it can be shown that,

$$2d_{hkl}\sin(\theta) = n\lambda \tag*{1)}$$

$$d_{hkl} = \frac{n\lambda}{2\sin(\theta)} \tag*{2)}$$

where *n* is the number of wavelengths, λ is the wavelength of the incident x-rays, θ is the angle of the source to the surface of the sample, and d_{hkl} is the interplanar spacing for planes with indices *h*, *k*, and *l*. In bcc metals, the first set of Bragg reflections expected are (110), (200), and (211). The relationship between a measured d_{hkl} and a_o for a bcc material is

$$\frac{1}{d_{hkl}^2} = \left[h^2 + k^2 + l^2\right]\frac{1}{a^2} \tag*{3)}$$

$$a_0 = d_{hkl}\sqrt{h^2 + k^2 + l^2}$$

$$a_0 = \frac{n\lambda}{2\sin(\theta_{hkl})}\sqrt{h^2 + k^2 + l^2} \tag*{(4)}$$

For hcp the measured reflections are (100), (101), (102), (110), (103), (200), and (112).

$$\frac{1}{d_{hkl}^2} = \left[\frac{4}{3}\left(h^2 + k^2 + hk\right) + l^2\left(\frac{a}{c}\right)^2\right]\frac{1}{a^2} \tag*{(5)}$$

For planes (*hk0*) and (*00l*).

$$a_0 = 2d_{hk0}\sqrt{\frac{h^2 + k^2 + hk}{3}}$$

$$a_0 = \frac{n\lambda}{\sin(\theta_{hk0})}\sqrt{\frac{h^2 + k^2 + hk}{3}} \tag*{(6)}$$

$$c_0 = l \cdot d_{00l}$$

$$c_0 = l\frac{n\lambda}{2\sin(\theta_{00l})} \tag*{(7)}$$

By collecting all of this, and finding the volume for each unit cell (a_0^3 for bcc and $a_0^2 b_0$ for hcp), Figure 6-4 was generated. A steady change in lattice parameter can be seen as V is added to Ti-6Al-4V. The unit cell's volume increases at a rate of 6.3e-2 Å^3/(vol %); a_0 increases at a rate of 2.3e-3 Å/(vol %) for the bcc crystals. Once the dual phase region is entered, the bcc lattice shrinks slightly while the hcp unit cell is larger. The shrinkage is due to the decreased amount of titanium dissolved in the vanadium bcc crystals. These results are promising, as there is a slow, gradual change in lattice parameter even when there is a transition involving two phases present at the same time.

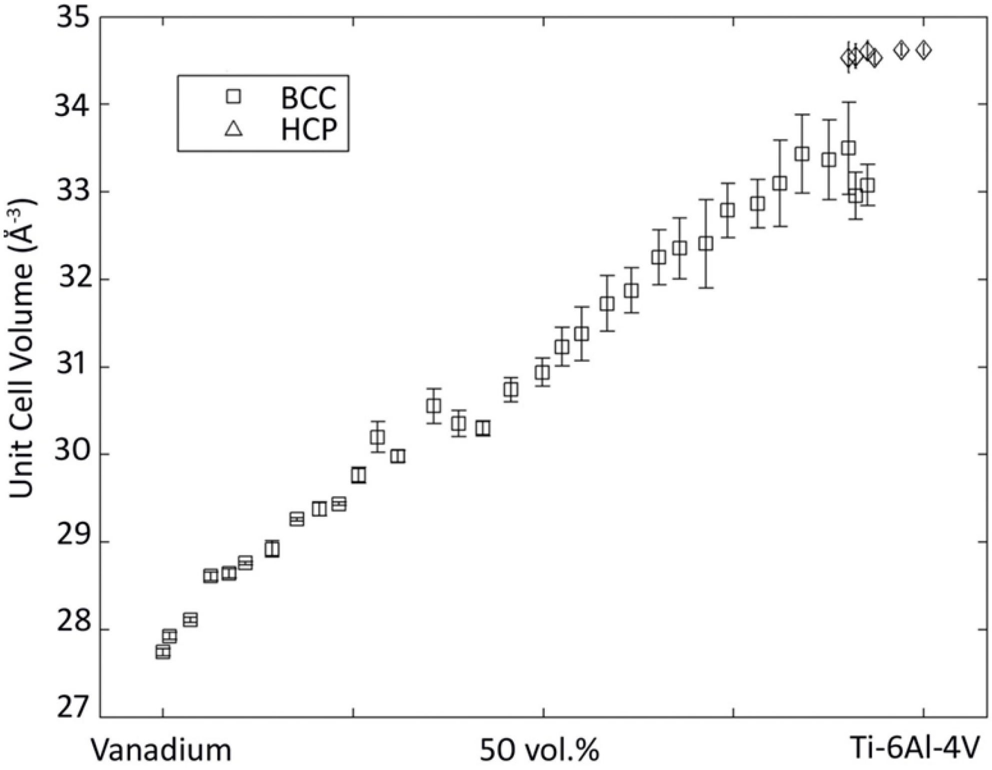

Figure 6-4: Volume of a unit cell versus composition. As more titanium is added, an increase in cell volume can be seen. Beta-titanium has a larger lattice constant than vanadium (3.282 Å for Ti versus 3.020 Å for V), so this expansion is reasonable.

The next alloy synthesized was fabricated in two geometries. The first was a radial gradient deposited on a central A286 stainless steel rod. It transitions from 304L stainless steel at the core to Invar 36 at the perimeter, as seen in Figure 6-5. The alloy was fabricated by rotating the central A286 cylinder along one axis while the build head slowly moved along the axis perpendicular to the plane of rotation. The second geometry grown was square pillars, the same as the Ti-6Al-4V to vanadium. In this case, the 304L steel was deposited onto 304L stainless steel plate with Invar 36 at the free end. This gradient alloy was chosen, as it offers a very common and versatile material (304L) which is high in strength, and can be welded and readily machined. Invar provides a surface layer with little to no thermal expansion.

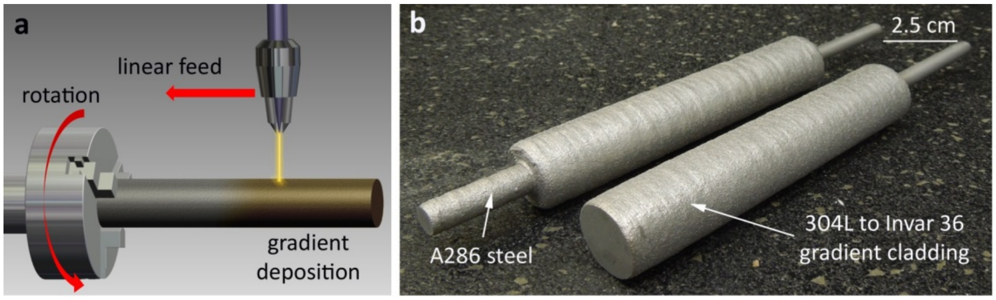

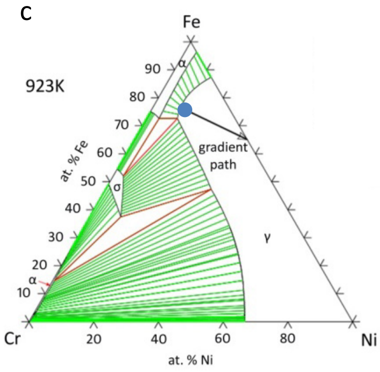

Figure 6-5: **(a)** Schematic of the rotational deposition process used to develop alloys with gradient compositions in a radial direction. **(b)** Image of two radially grown alloys where a 304L to Invar 36 gradient was applied to a rotating A286 stainless steel rod. **(c)** A calculated phase diagram at 923 K showing the gradient path from 304L to Invar 36. Phase diagram calculated by our collaborator, Richard Otis from Penn State.

A situation where this combination of properties is useful is mirror mounts used on satellites in space. Mirrors used in space applications frequently consist of a quartz substrate that has been silvered on one side. The quartz has a negligible coefficient of thermal expansion (CTE). If the mount holding the mirror's CTE does not match the mirror substrate's CTE, then the mirror will experience a torque and deform. In high performance systems, this slight deflection can significantly degrade the optic system. An obvious solution would be to make the entire mount of Invar. Then the problem of connecting the mount to the main structure arises. If the mount is entirely made of Invar, it cannot be welded. Therefore, bolts would have to be used, but there is then a CTE mismatch between the mount and bolt used to attach it. By transitioning within the mount itself from Invar at the mirror end to stainless steel at the other, it can both act as an effective holder with zero CTE as well remain weldable to a steel support structure.

The radial gradient was designed with the intent to replace the current inserts for carbon fiber paneling. Panels are currently manufactured using a cladding of carbon fiber around aluminum honeycomb panels (Figure 6-6). These are used for their high stiffness and low density. However, in order to attach the panels together, or to other structures, threaded metal inserts are epoxied into the panels. These panels are often subjected to extreme temperatures with large fluctuations, and undergo significant thermal cycling. The carbon fiber face sheets have a near-zero CTE, while the steel inserts have a high CTE. The radial gradient was designed such that the threading would be the same material as that used for the bolts which would attach to it. There is then a rapid transition to Invar to minimize the expansion of the insert as a whole to protect the carbon fiber from expansion. Figure 10a is a collection of fully finished inserts. Figure 6-6c is before and after a pullout test. Rupturing of the carbon fiber face sheet is visible.

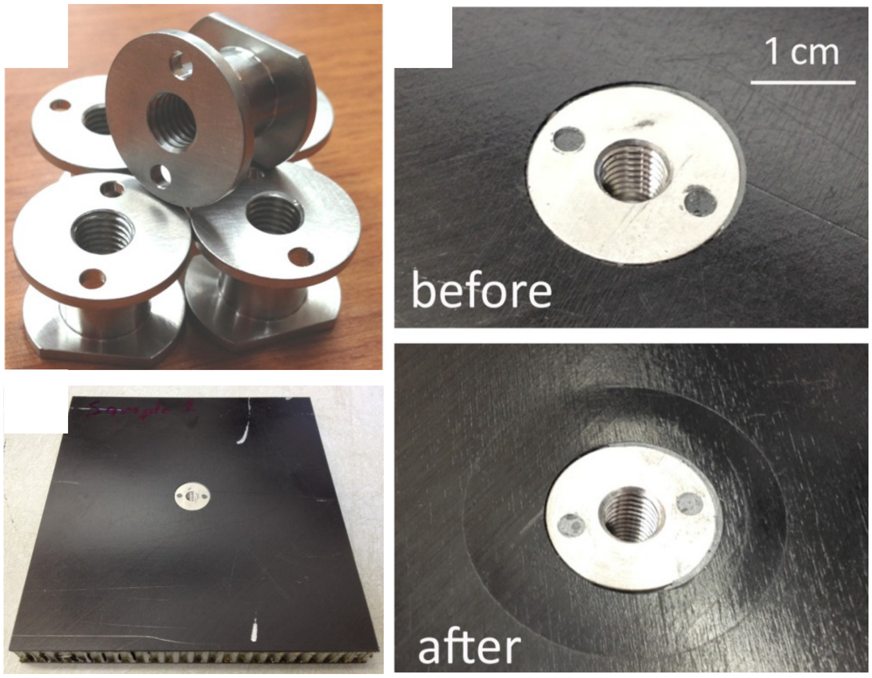

Figure 6-6: (a) Printed and machined inserts for carbon fiber and aluminum honeycomb sheets. (b) An insert installed into a panel. (c) Before and after a pull-out test.

Thermodynamically, this is also an ideal system to attempt, as both alloys are primarily iron with significant amounts of nickel. 304L contains approximately 20% chromium, 10% nickel, and 70% iron.[8] It is an austenitic grade of stainless steel. Similarly, Invar 36 is fcc iron, which is the austenite phase. As seen in Figure 6-5c, it contains 64% iron and 36% nickel. The gradient path is highlighted on the ternary phase diagram. The only phase which should be produced through the entire sample is austenitic fcc.

Determination of phases present was done via XRD in a manner similar to the Ti-6Al-4V to vanadium pillar above. It was sectioned in the manner shown in Figure 6-7. Each of the six XRD scans are also shown in the figure. Only fcc peaks are seen, and there is no apparent shift of peak positions. This is a great result, as it means the lattice has changed minimally, and the amount of strain and deformation experienced by the lattice should be minimized.

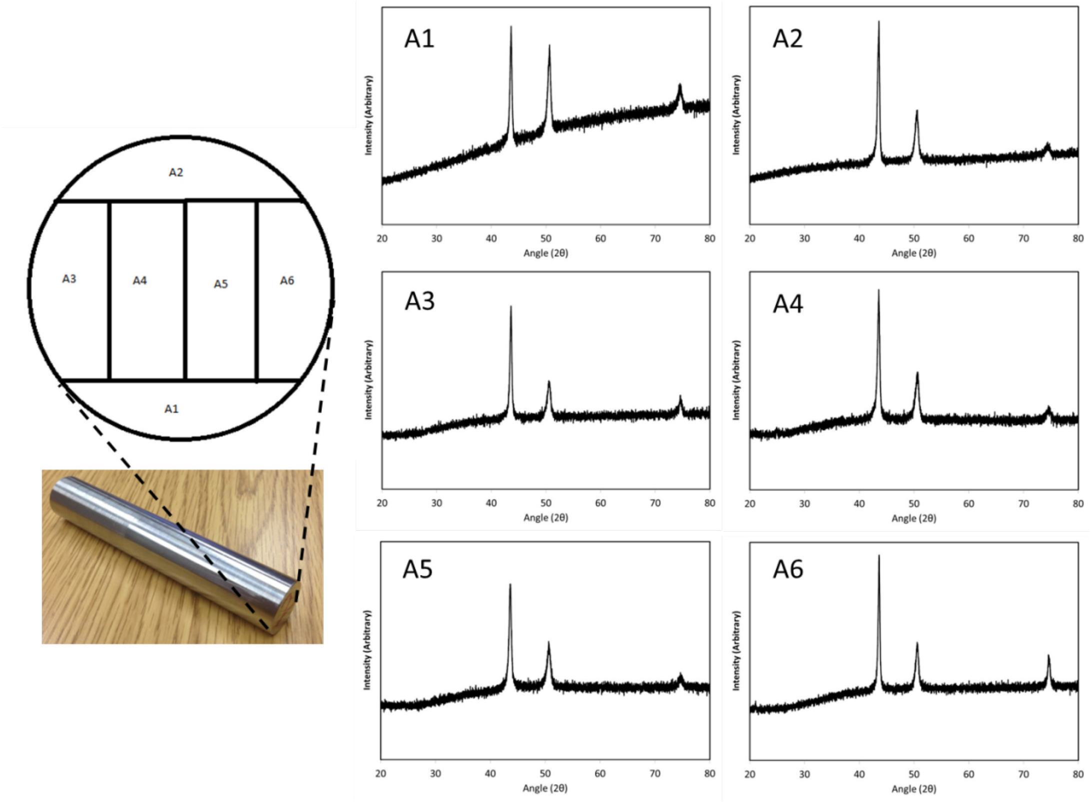

Figure 6-7: X-ray scans were obtained for the radial sample as well as for the linear sample of 304L to Invar 36. The radial alloy was sectioned according to the map above and x-ray scans were performed on each section, shown at right. Only the austenite phase was detected.

In order to estimate the CTE throughout the gradient, two mixed-composition pillars were fabricated. They were then machined into 2-3 mm tall cylinders with an aspect ratio of, at most, 2:1. The faces were polished to be plane parallel. The samples were tested in a Perkin-Elmer Diamond TMA with a static applied force of 100 mN. They were then repeatedly cycled from room temperature to 773 K. A representative thermal cycling measurement is shown in Figure 6-8a. Multiple cycles were used, since typically the first heating cycle is needed to ensure the sample is properly seated in the testing apparatus. The following heating and cooling cycles all overlay consistently. In order to find the CTE from a position versus temperature plot the instantaneous slope is determined for each point and then plotted versus temperature.

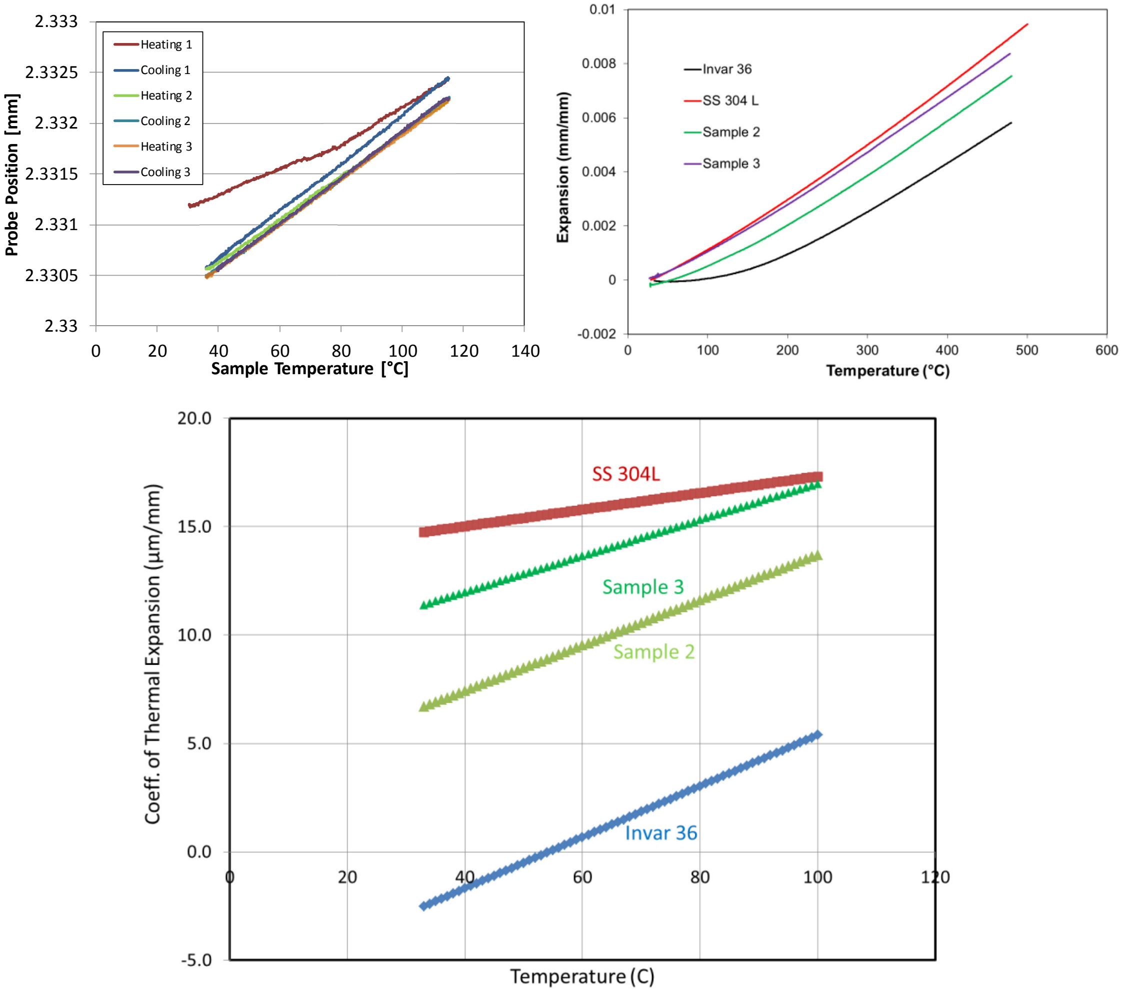

Figure 6-8: (a) A representative thermal expansion measurement plotting probe position vs. temperature. The first cycle was always discarded since it was used to "seat" the sample properly under the load. (b) Expansion of the cylinder versus temperature. Four of those measurements are shown, one from the Invar side of the gradient, one from the steel side, and two samples near the Invar side of the gradient. Sample 2 represents the sample most near the pure Invar, and Sample 3 is the next sample beyond that. (c) The CTE was obtained by differentiating the curves from (b).

A strong correlation between composition and CTE was measured. Figure 6-8b is a plot of probe position versus temperature across a very large temperature range. Invar 36 and SS 304L are the “pure” alloys, while Sample 2 is 90% Invar 36 and Sample 3 75% Invar. Near room temperature very different expansion behaviors are seen. Invar 36 initially shrinks, stays constant for a small range, and then begins expanding. On the other hand, the other three samples all monotonically expand. Figure 6-8c is the result of taking derivatives of the above curves. Invar 36 is again seen to initially have a slightly negative CTE, having its actual CTE of zero around 52° C, and continuing to a CTE of 5 ppm. Sample 2 begins with a moderate CTE of 6.5 ppm and grows to 13.5 ppm by 100° C. Sample 3 starts at 11.3 ppm and increases to 17 ppm. 304L is 14.5 ppm initially, and, like Sample 3, has a final CTE of approximately 17 ppm. Figure 9c gives the total change in CTE as well as the change in CTE per degree Celsius. Invar 36 has the largest change, at 7.84 ppm/K, and 304L has the least at 2.12 ppm/K. Both of the intermediate alloys have a smaller change in CTE than Invar. The alloy having greater Invar composition having the greater sensitivity to temperature. The CTE properties measured for all compositions of the gradient alloy demonstrate that it is possible to tailor the CTE of an alloy by mixing known materials. It is likely with sufficiently small steps, a completely tailored CTE could be achieved.

Table 6-2: Linearized CTEs and change in CTE from ambient temperatures to 373 K

Composition	ΔCOE	$\frac{\mathrm{d}\mathbf{COE}}{\mathrm{d}\mathbf{T}}$
	(ppm/K)	(ppm/K^2)
Invar 36	7.84	0.12
Sample 2	6.94	0.10
Sample 3	5.47	0.081
SS 304L	2.12	0.032

In this chapter, the feasibility of fabricating two different gradient alloys was demonstrated. By careful selection of the alloys to be deposited, unwanted phases were able to be avoided. Confirmation of the correct phases being present was demonstrated via XRD. The tunability of the coefficient of thermal expansion of the 304L – Invar system was also demonstrated.

Collaborators on this project include Joanna Kolodziejska from Caltech/JPL for the illustrations in Figure 6-1 and Figure 6-5, Richard Otis from Penn State for the phase diagram in Figure 6-5, and John Paul Borgonia from JPL for being the driving force behind this project, fabricating all of the structures used in this study.

References

(1) Santos, E. C.; Shiomi, M.; Osakada, K.; Laoui, T. Rapid manufacturing of metal components by laser forming. *Int. J. Mach. Tools Manuf.* **2006**, *46*, 1459–1468.

(2) Griffith, M. L.; Ensz, M. T.; Puskar, J. D.; Robino, C. V.; Brooks, J. A.; Philliber, J. A.; Smugeresky, J. E.; Hofmeister, W. H. Understanding the Microstructure and Properties of Components Fabricated by Laser Engineered Net Shaping (LENS). *MRS Proc.* **2011**, *625*, 9.

(3) Collins, P. C.; Banerjee, R.; Banerjee, S.; Fraser, H. L. Laser deposition of compositionally graded titanium–vanadium and titanium–molybdenum alloys. *Mater. Sci. Eng. A* **2003**, *352*, 118–128.

(4) Banerjee, R.; Collins, P. .; Bhattacharyya, D.; Banerjee, S.; Fraser, H. . Microstructural evolution in laser deposited compositionally graded α/β titanium-vanadium alloys. *Acta Mater.* **2003**, *51*, 3277–3292.

(5) Gong, W. Al-V Phase Diagram **2004**.

(6) Kaufman, L. Ti-V Phase Diagram **1987**.

(7) Kaufman, L. Al-Ti-V Phase Diagram **1987**.

(8) *Metals Handbook*; 10th ed.; ASM International: Materials Park, OH, 1990.

APPENDIX A - COMPLETE TABLE OF MEASURED PROPERTIES FOR WEAR TESTING

	A/X/C	Density (g/cm^3)	2.0Hv	E (GPa)	K (GPa)	G (GPa)	k, Dim. Wear Coeff.
Cu38Zr42Al7Be10Nb3	A	6.948	626.5	108.5	119.5	40.2	6.60E-05
Cu44Zr46Al5Y2Nb3	A	6.925	407.4	76.9	110.7	27.8	9.63E-05
Cu42.5Zr42.5Al7Be5Nb3	A	7.020	544.4	97.8	118.5	35.9	6.53E-05
Cu41.5Zr41.5Al7Be7Nb3	A	6.867	523.9	102.0	115.2	37.7	7.89E-05
Cu40Zr40Al10Be10	A	6.582	604.3	114.2	117.0	42.7	1.14E-04
Cu42Zr41Al7Be7Co3	A	6.846	532.4	101.3	117.8	37.3	1.10E-04
Cu47Zr46Al5Y2 (POD)	A	7.003	409.8	75.3	115.9	27.1	5.95E-05
Cu42Zr41Al7Be7Cr3	A	6.813	575.1	106.5	116.1	39.5	6.73E-05
Cu44Zr44Al5Ni3Be4	A	7.014	504.3	95.5	115.7	35.1	9.51E-05
Cu41.5Zr41.5Al7Be10	A	6.722	557.6	104.5	113.9	38.8	8.68E-05
Cu44Zr44Al7Be5	A	6.978	514.3	99.0	114.0	36.5	7.76E-05
Cu43Zr43Al7Be7	A	6.811	550.3	99.0	111.3	36.6	9.38E-05
Cu41Zr40Al7Be7Co5	C	6.864	589.9	103.5	116.8	38.3	1.05E-04
Cu43Zr43Al7Ag7	C	7.224	496.1	90.6	117.6	33.0	8.65E-05
Cu47.5Zr48Al4Co0.5	X	7.138	381.9	79.6	116.3	28.7	8.76E-05
Cu50Zr50	X	7.313	325.9	81.3	116.8	29.4	7.98E-05
Cu46.5Zr46.5Al7	X	7.007	510.5	101.4	113.0	37.5	8.92E-05
Cu44Zr44Al7Ni5	X	7.052	570.0	99.2	114.8	36.6	7.68E-05

	A/X/C	Poisson Ratio	POD (mg)	Volume Loss (mm^3)	Rm (µm)	Track Width (mm)	k, Dim. Wear Coeff.
Cu38Zr42Al7Be10Nb3	A	0.35	0.6	0.079	1.930	0.65	6.60E-05
Cu44Zr46Al5Y2Nb3	A	0.38	0.8	0.116	2.237	0.71	9.63E-05
Cu42.5Zr42.5Al7Be5Nb3	A	0.36	0.6	0.078	1.800	0.73	6.53E-05
Cu41.5Zr41.5Al7Be7Nb3	A	0.35	0.7	0.095	1.757	0.85	7.89E-05
Cu40Zr40Al10Be10	A	0.34	0.9	0.137	2.138	0.64	1.14E-04
Cu42Zr41Al7Be7Co3	A	0.36	0.9	0.131	1.981	0.86	1.10E-04
Cu47Zr46Al5Y2 (POD)	A	0.39	0.5	0.071	3.389	0.69	5.95E-05
Cu42Zr41Al7Be7Cr3	A	0.35	0.6	0.081	1.924	0.71	6.73E-05
Cu44Zr44Al5Ni3Be4	A	0.36	0.8	0.114	2.368	0.85	9.51E-05
Cu41.5Zr41.5Al7Be10	A	0.35	0.7	0.104	1.554	0.65	8.68E-05
Cu44Zr44Al7Be5	A	0.36	0.7	0.093	1.741	0.76	7.76E-05
Cu43Zr43Al7Be7	A	0.35	0.8	0.113	1.290	0.74	9.38E-05
Cu41Zr40Al7Be7Co5	C	0.35	0.9	0.126	1.605	0.78	1.05E-04
Cu43Zr43Al7Ag7	C	0.37	0.8	0.104	1.292	0.75	8.65E-05
Cu47.5Zr48Al4Co0.5	X	0.39	0.8	0.105	1.797	0.78	8.76E-05
Cu50Zr50	X	0.38	0.7	0.096	1.693	0.80	7.98E-05
Cu46.5Zr46.5Al7	X	0.35	0.8	0.107	1.336	0.69	8.92E-05
Cu44Zr44Al7Ni5	X	0.36	0.7	0.092	1.042	0.61	7.68E-05

	A/X/C	Density (g/cm^3)	2.0Hv	E (GPa)	K (GPa)	G (GPa)	k, Dim. Wear Coeff.
Ni40Zr28.5Ti16.5Be15	C	6.432	715.2	128.4	131.7	48.0	1.04E-04
Ni40Zr28.5Ti16.5Cu5Be10	C	6.649	668.2	112.0	129.2	41.3	3.76E-05
Ni40Zr28.5Ti16.5Cu5Al10	X	6.485	627.2	99.3	128.7	36.2	3.53E-05
Ni56Zr17Ti13Si2Sn3Be9	X	6.895	562.5	141.1	144.7	52.7	1.21E-05
Ni57Zr18Ti14Si2Sn3Be6	X	6.958	637.3	139.4	145.4	52.0	3.59E-05
Ti33.18Zr30.51Ni5.33Be22.88Cu8.1	A	5.481	486.1	96.9	110.6	35.8	1.75E-04
Ti40Zr25Be30Cr5	A	4.850	465.4	97.5	104.6	36.2	7.47E-04
Ti40Zr25Ni8Cu9Be18	A	5.501	544.4	101.1	110.8	37.5	1.44E-04
Ti45Zr16Ni9Cu10Be20	A	5.322	523.1	104.2	111.1	38.8	1.49E-04
Zr41.2Ti13.8Cu12.5Ni10Be22.5	A	6.061	530.4	95.2	109.6	35.1	3.16E-04
Zr52.5Ti5Cu17.9Ni14.6Al10	A	6.670	474.4	88.5	110.5	32.4	2.19E-04
Zr57Nb5Al10Cu15.4Ni12.6	A	6.667	439.7	83.3	111.5	30.3	2.37E-04
Zr65Cu17.5Al7.5Ni10	A	6.643	463.3	116.9	110.5	44.2	1.82E-04
Zr55Cu30Al10Ni5	A	6.690	520.8	87.2	110.3	31.9	3.36E-04
Zr35Ti30Be27.5Cu7.5	A	5.361	461.8	90.5	104.4	33.4	5.83E-04
Zr36.6Ti31.4Nb7Cu5.9Be19.1	C	5.700	391.1	84.7	105.8	31.0	6.21E-04
Zr55Al20Co25	C	6.176	602.5	119.6	108.9	45.4	7.89E-04

	A/X/C	Poisson Ratio	POD (mg)	Volume Loss (mm^3)	Rm (µm)	Track Width (mm)	k, Dim. Wear Coeff.
Ni40Zr28.5Ti16.5Be15	C	0.34	0.8	0.124	1.698	0.47	1.04E-04
Ni40Zr28.5Ti16.5Cu5Be10	C	0.36	0.3	0.045	0.768	0.82	3.76E-05
Ni40Zr28.5Ti16.5Cu5Al10	X	0.37	0.3	0.042	0.836	0.66	3.53E-05
Ni56Zr17Ti13Si2Sn3Be9	X	0.34	0.1	0.015	0.487	0.38	1.21E-05
Ni57Zr18Ti14Si2Sn3Be6	X	0.34	0.3	0.043	1.578	0.43	3.59E-05
Ti33.18Zr30.51Ni5.33Be22.88Cu8.1	A	0.35	1.2	0.210	3.162	0.79	1.75E-04
Ti40Zr25Be30Cr5	A	0.34	4.4	0.897	12.150	0.80	7.47E-04
Ti40Zr25Ni8Cu9Be18	A	0.35	1.0	0.173	2.325	0.83	1.44E-04
Ti45Zr16Ni9Cu10Be20	A	0.34	1.0	0.179	2.309	0.90	1.49E-04
Zr41.2Ti13.8Cu12.5Ni10Be22.5	A	0.36	2.3	0.379	6.788	0.71	3.16E-04
Zr52.5Ti5Cu17.9Ni14.6Al10	A	0.37	1.8	0.262	3.607	0.58	2.19E-04
Zr57Nb5Al10Cu15.4Ni12.6	A	0.38	1.9	0.285	6.413	0.75	2.37E-04
Zr65Cu17.5Al7.5Ni10	A	0.32	1.5	0.218	3.082	0.62	1.82E-04
Zr55Cu30Al10Ni5	A	0.37	2.7	0.404	3.754	0.92	3.36E-04
Zr35Ti30Be27.5Cu7.5	A	0.36	3.8	0.699	11.796	1.04	5.83E-04
Zr36.6Ti31.4Nb7Cu5.9Be19.1	C	0.37	4.3	0.746	4.951	0.79	6.21E-04
Zr55Al20Co25	C	0.32	5.9	0.947	9.532	0.71	7.89E-04

Appendix B – A Series of Other Studies

Bridgman Solidification

Directional Solidification:
Heating a 2-phase alloy to its liquidus and then cooling slowly from one side to directionally solidify the second phase.

Microgravity is needed to avoid sedimentation of the dendrites during processing (different densities).

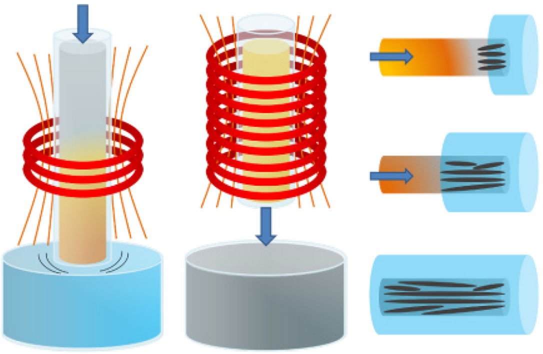

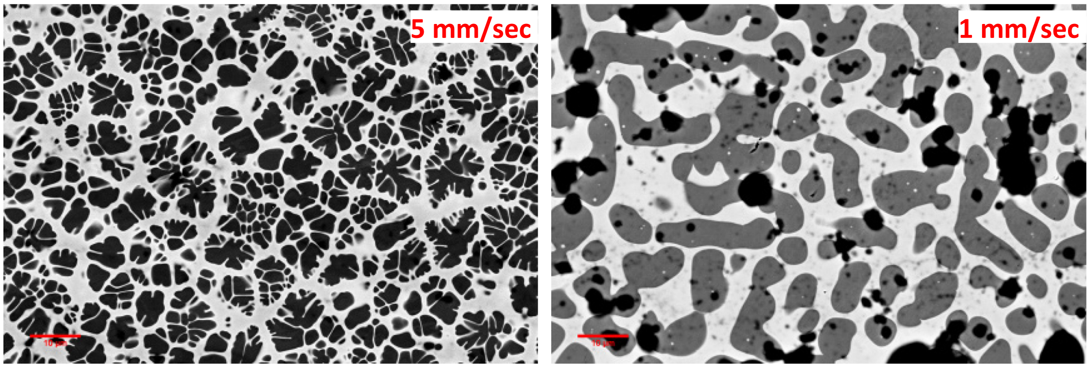

A 1.5 inch diameter graphite rod had a hole bored in the center. A quartz tube containing a thin DV1 rod was then inserted into the center, and the susceptor was heated via RF induction heating. The susceptor was used since the DV1 rods were too thin to couple efficiently with the low frequency of the power supply. A container of a molten fusible alloy was used as a quenching bath. The quartz tubes containing DV1 rods were lowered at differing rates (5 mm/sec and 1 mm/sec) into the metal bath. This was intended to initiate directional solidification, with the dendrites growing from the molten alloy bath towards the graphite susceptor. Unfortunately, no texturing was observed, although the alloy being annealing for longer did have substantial coarsening of the dendrites. It is likely the liquidus temperature was not reached to fully remelt the dendrites. Instead, the existing dendrites coarsened. Dark spots are due to polishing debris adhered onto the surface. Images were taken in QBSD mode at 2500x. Experiments were performed with Henry Kozachkov and Doug Hofmann.

Quasistatic Compression Testing of a Single Eggbox's Pyramid

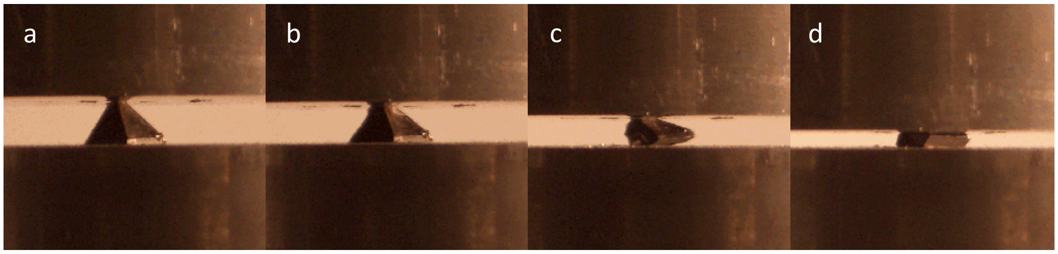

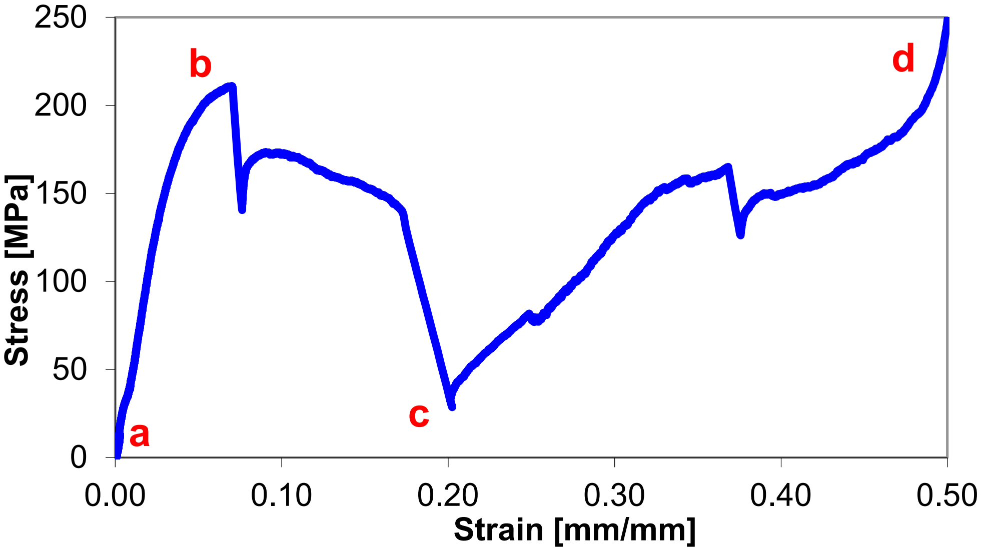

A single eggbox from structures used in Chapters 2-4. The stress supported by a single pyramid should be the maximum stress achievable by an eggbox structure. The difference between the stress supported by a sheet and a single eggbox indicates how much strength is lost due to geometry. It is known from previous chapters the 1 mm offset between pyramids allows for torqueing to occur which lowers the strength of welded structures. This was also seen in the images published in Joe Schramm's thesis.

The slight change in slope of the stress-strain curve is due to the pyramid's tip sinking into the hardened steel platens as the Instron was loaded. The pyramid is harder than the platens, so it is not surprising it is able to dent them significantly. As point (b) is approached the pyramid begins to yield and plastic deformation behavior is apparent. This signifies the spacing of dendrites in the composite pyramid is on the appropriate length scale to arrest shear band growth.

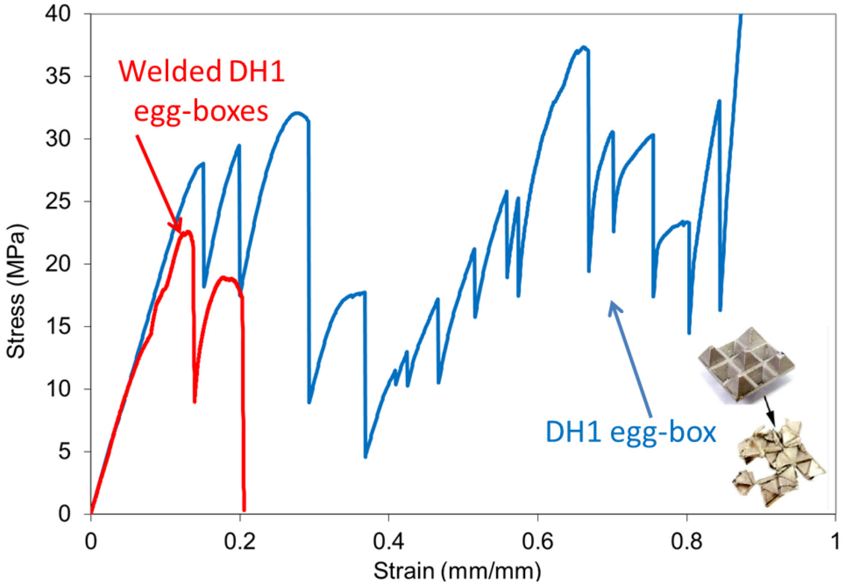

Above, Figure 3-3 is recreated to highlight the difference between performance in a single pyramid and a full eggbox structure. Each structure exhibits significant recovery after the first failure event. The single pyramid supports significantly more stress, although this is likely an effect of the eggbox geometry having both ‘up’ and ‘down’ pyramids. In a 3x3 eggbox, the entire load would be supported by 4 pyramids (in the inset figure, each would be facing down). For this reason, the measured stress is lower than that actually experienced by the actual 4 mm^2 of tip which is in contact with the platens. The pyramid was still, however, able to withstand more than seven times as much stress as a whole eggbox structure, a difference which is not made up for in geometry. For this reason, we can conclude the eggbox design used has further room for optimization.

Metallic Glass Wires

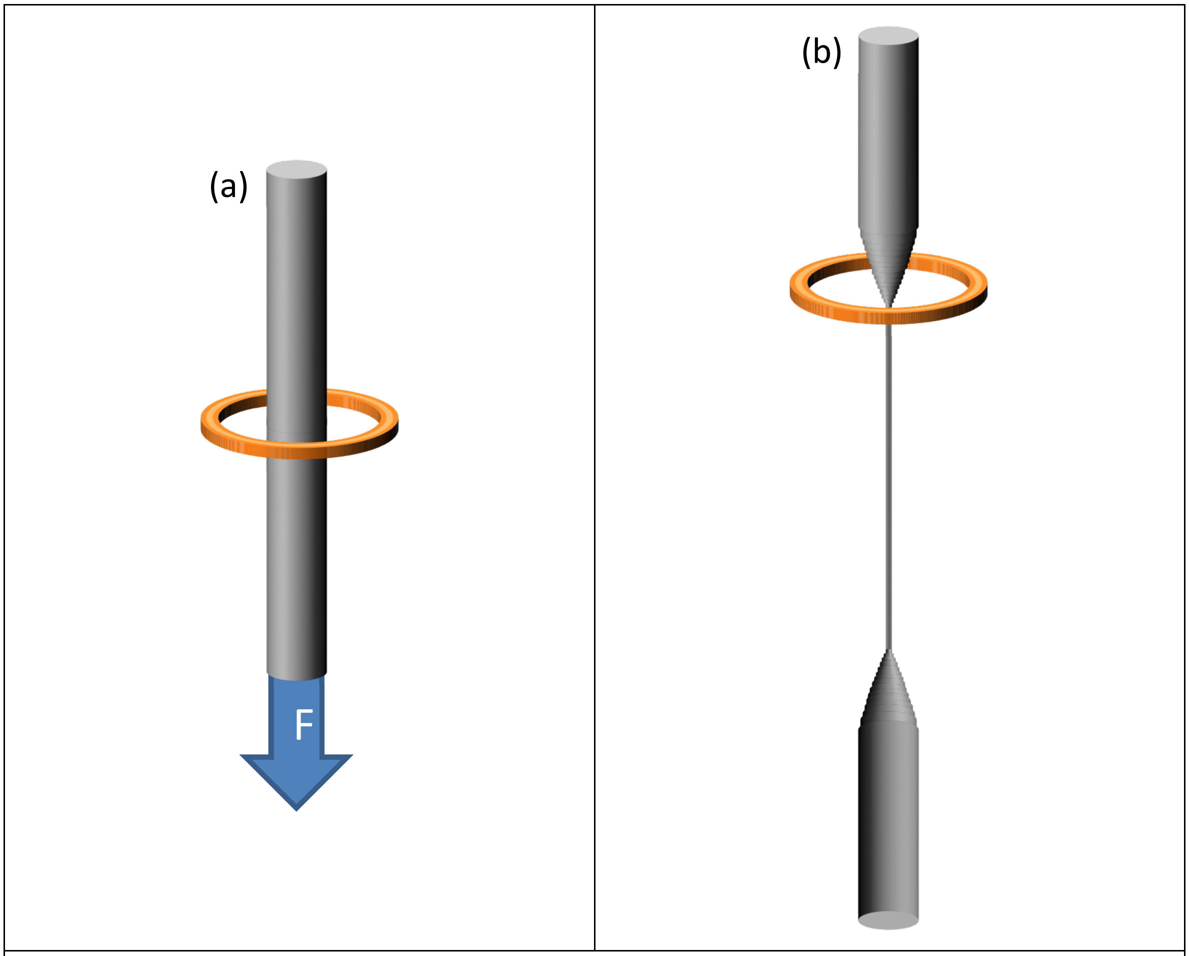

(a) Initially a metallic glass cylinder is preloaded with a force (e.g. a mass being pulled by gravity). A RF induction coil is placed around the cylinder.
(b) Localized heating by the RF coil causes the cylinder to heat above the glass transition temperature and, with sufficient force, flow occurs. As the coil thins it becomes more efficient at radiating heat since the surface area to volume ratio dramatically increases. Eventually the wire becomes thin enough the RF coil can no longer efficiently couple to the glass, and no more energy can be put into the system. At this point the wire stops drawing further.

The actual drop tower height was in excess of 18 inches.

A series of drop tower experiments. Wires were made with gauge sections of over 0.5 m. Different lengths and thicknesses were achieved by modifying the applied force and heating power.

This series of experiments were performed with Allison Kunz and Doug Hofmann.

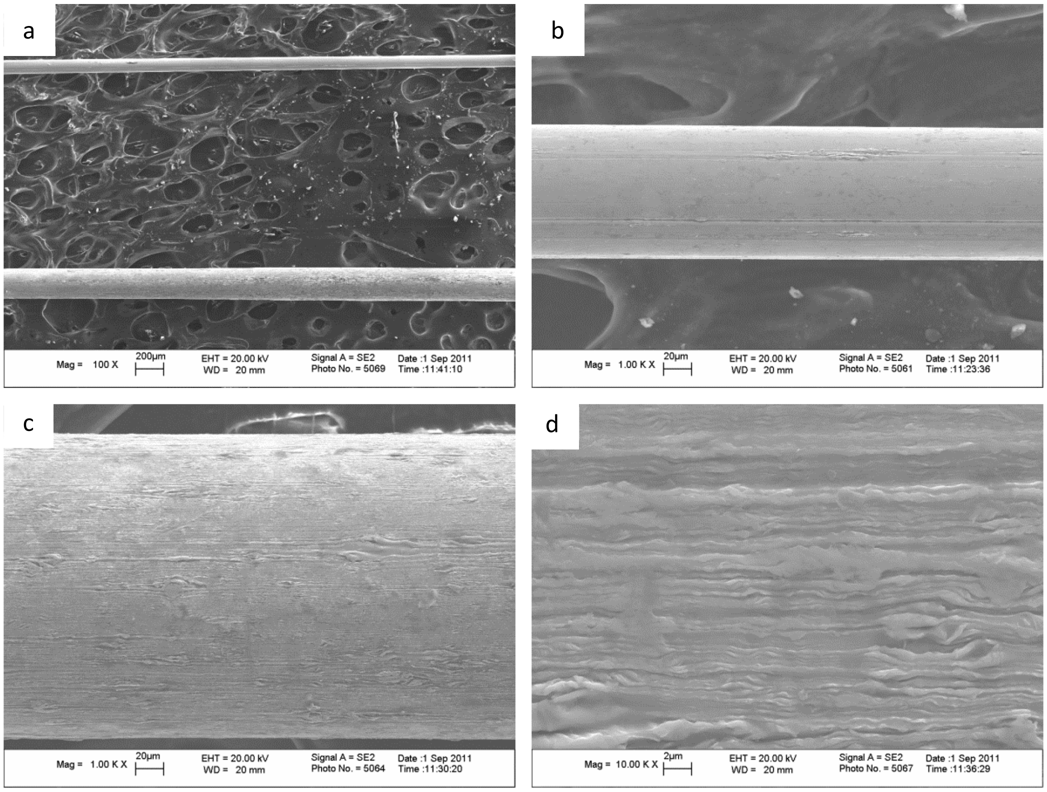

GHDT ($Zr_{35}Ti_{30}Be_{27.5}Cu_{7.5}$) wires.

(a) An overview of two wires. The top one is approximately 100 μm and the bottom is approximately 225 μm.

(b) 1000x of the top wire

(c) 1000x of the bottom wire

(d) 10000x of the bottom wire

Neither wire was brittle, which indicates they had likely fully vitrified. Thinner wires tended to have a much smoother surface. The thinner wire likely reached both a higher temperature and had its surface smoothed out due to imperfections smearing out over a longer length. Rods were initially fabricated via suction casting which leaves a moderately rough surface

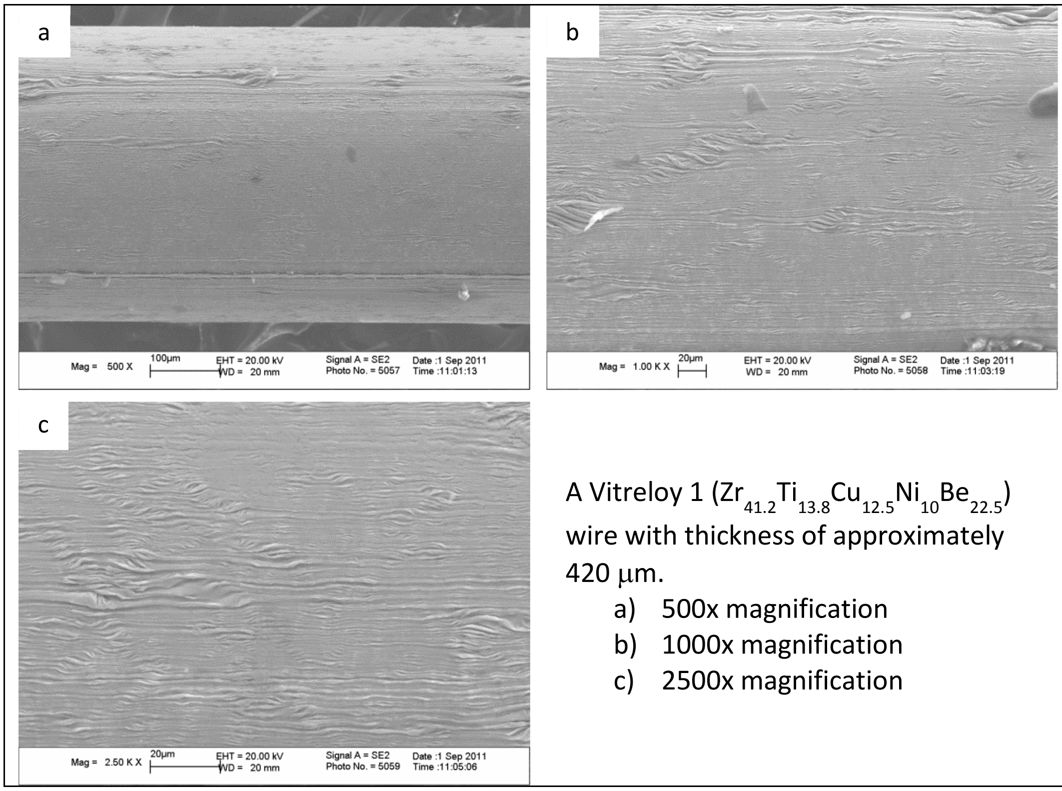

A Vitreloy 1 ($Zr_{41.2}Ti_{13.8}Cu_{12.5}Ni_{10}Be_{22.5}$) wire with thickness of approximately 420 µm.

a) 500x magnification
b) 1000x magnification
c) 2500x magnification

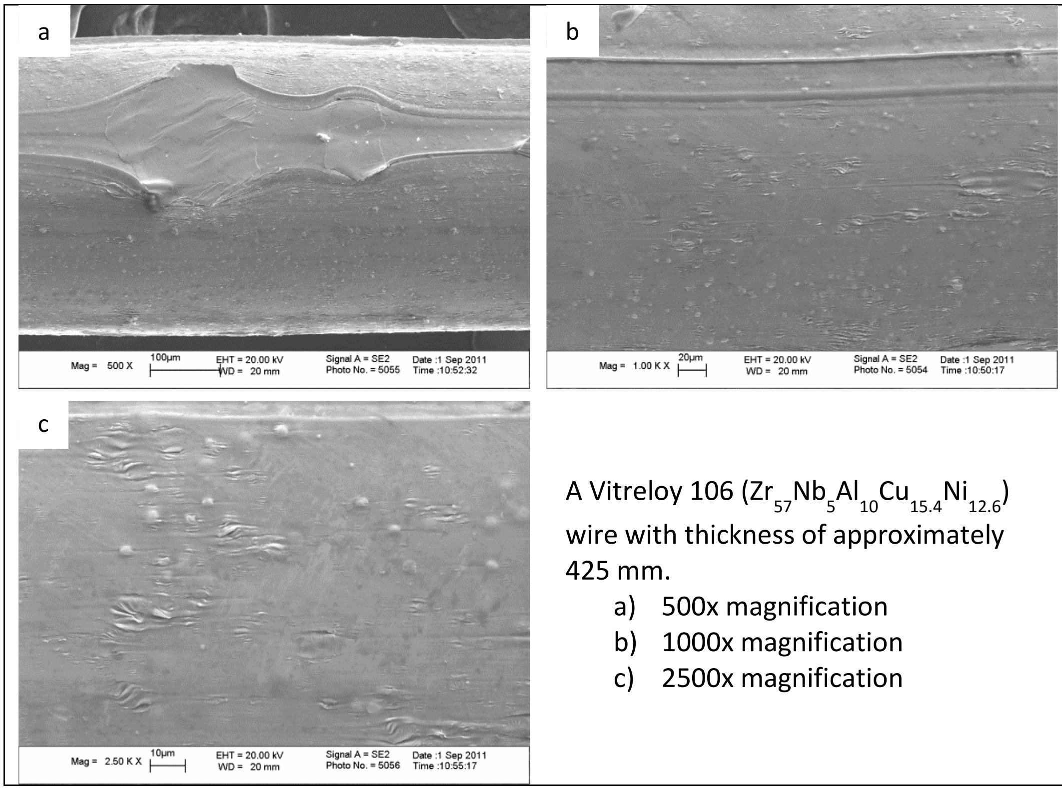

A Vitreloy 106 ($Zr_{57}Nb_5Al_{10}Cu_{15.4}Ni_{12.6}$) wire with thickness of approximately 425 mm.

a) 500x magnification
b) 1000x magnification
c) 2500x magnification

Coefficient of Thermal Expansion of BMGMC Composites

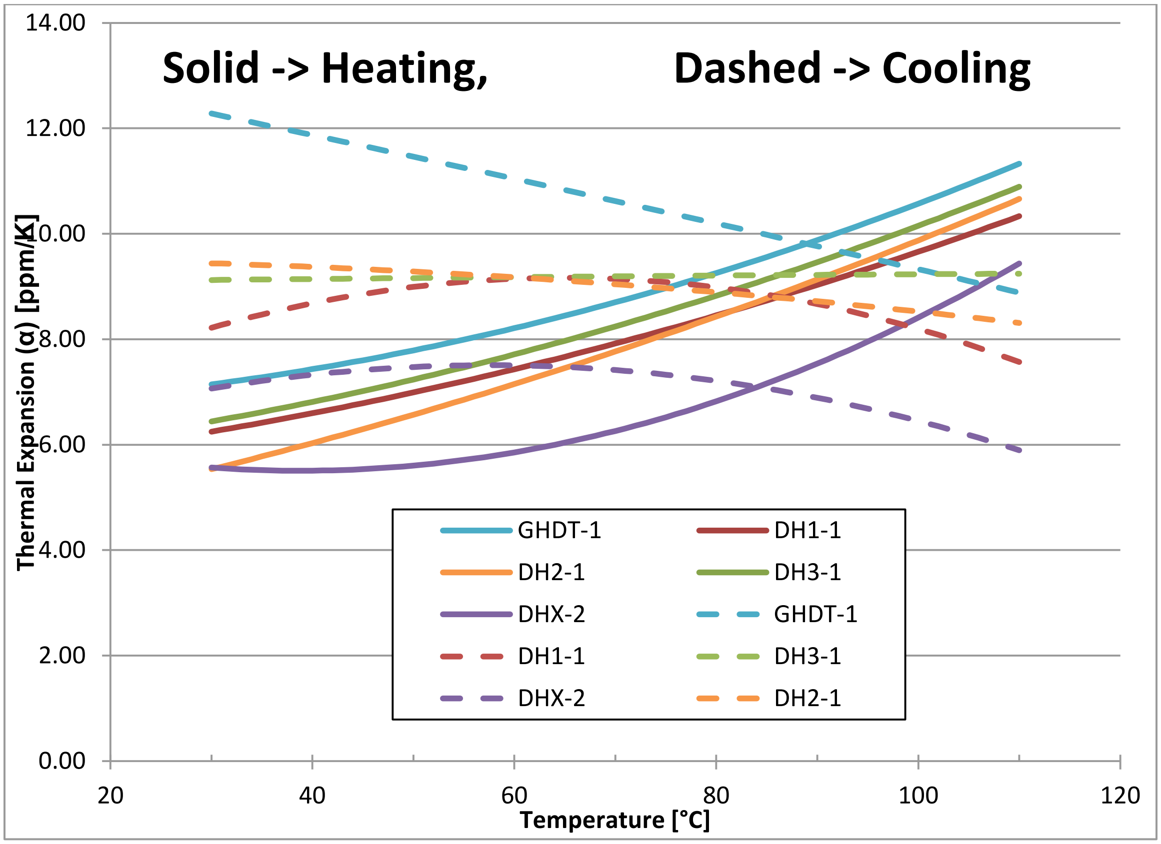

A series of BMGMC composites were alloyed, suction cast, sectioned, polished, and had their thermal expansion measured via TMA. Each alloy underwent a series of heating and cooling cycles. The average derivative of each alloy is shown above. Separate curves are given for heating and cooling.

Dendrite fractions should be as follows.

Alloy	Fraction Amorphous	Fraction Dendrite
GHDT	1	0
DH1	2/3	1/3
DH2	½	½
DH3	1/3	2/3
DHX	0	1

GHDT and DHX were taken as close approximations of the actual composition of the matrix and dendrites in the DH series of BMGMCs. At the time the precise composition could not be determined due to the beryllium content which could not be accurately measured.

Melt Spinner

In an attempt to further understand the corrosion properties of metallic glasses, a melt spinning apparatus was built to be able to vitrify a wide variety of MG systems. The idea behind a melt spinner is to eject a thin stream of molten alloy onto a rapidly spinning copper wheel. The wheel will rapidly quench the molten liquid at rates of up to 10^6 K/sec.

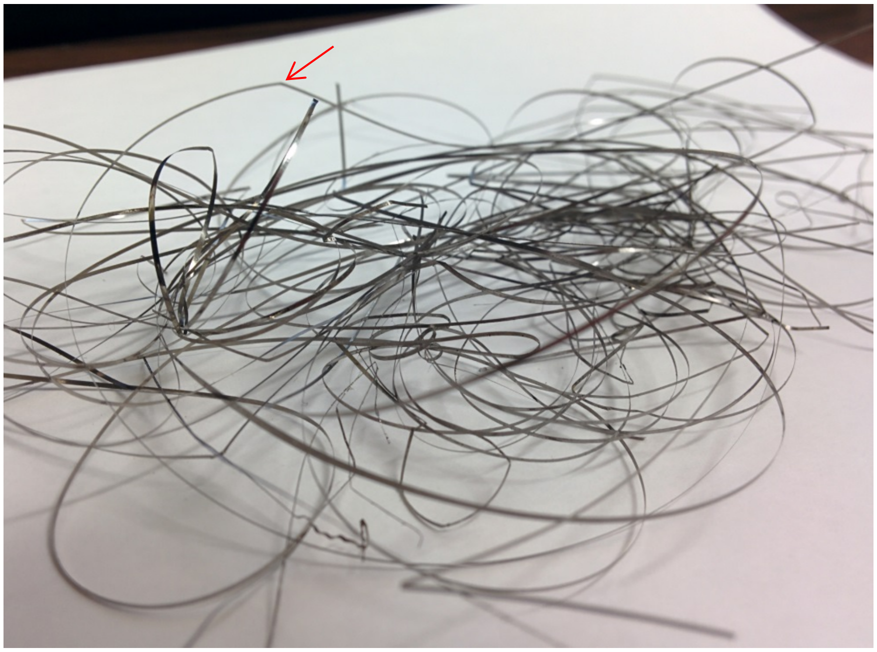

A successfully fabricated $Ni_{22}Zr_{78}$ wire. It is several meters long. The arrow points to a kink showing plasticity due to the wire's thickness being below twice the plastic zone size.

Unfortunately, the melt spinner met an untimely demise as the braising of the copper ring to the edge of the melt spinner failed in the middle of an experiment.

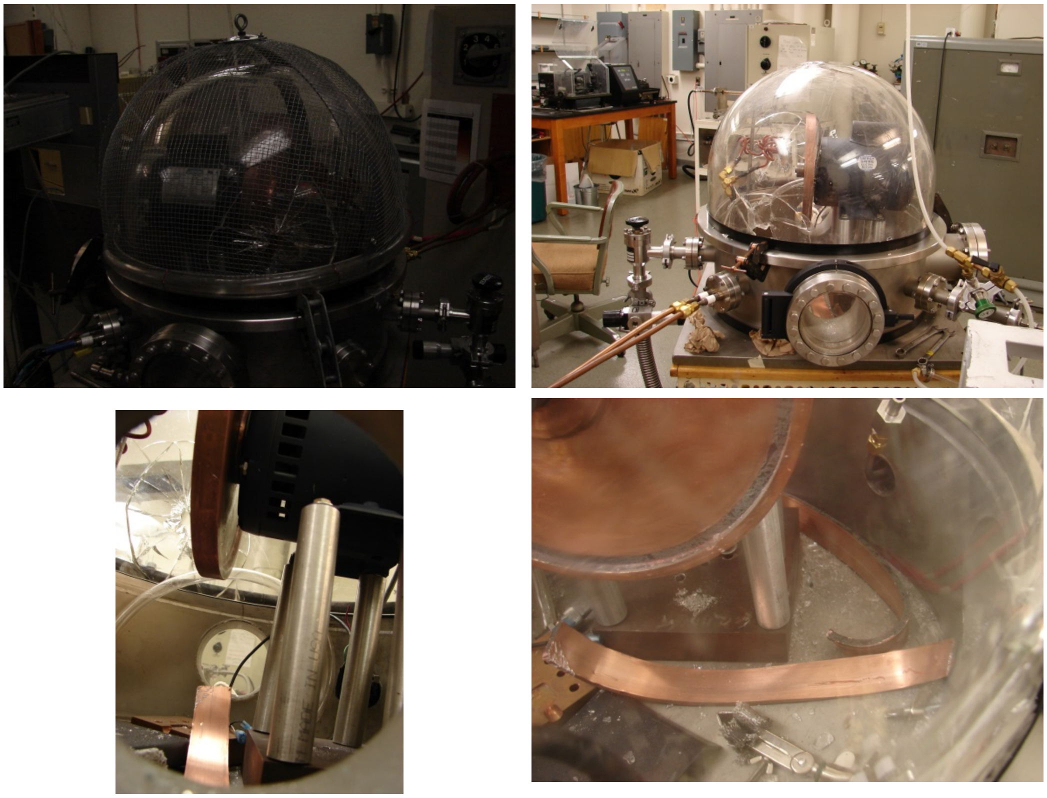

Unfortunately, the melt spinner met an untimely demise as the braising of the copper ring to the edge of the melt spinner failed in the middle of an experiment. In the end, the motor, bell jar, feedthroughs, ring stand, and clamp were all destroyed. The only surviving piece of the experiment was the feedstock ingot of metallic glass.